MAX PLANCK INSTITUTE
FOR SOLAR SYSTEM RESEARCH

Calibration Report of the RAPID Measurements in the Cluster Science Archive (CSA)

prepared by
Elena A. Kronberg, Patrick W. Daly, and Esa Vilenius

Version 10.0

Table of Contents

Reference Documents 4

List of Acronyms 5

1 Introduction 6

2 Instrument Description 6
2.1 The IIMS Instrument . . . 6
2.2 The IES Instrument . . . 8
2.3 Spin Sectorization . . . 8
2.4 Accumulation Time . . . 9

3 Measurement Calibration Procedures 9
3.1 Calibration Releases . . . 9
3.2 Calibration and Auxiliary Files . . . 10
3.3 The Calibration Procedure for IIMS . . . 10
3.4 The Calibration Procedure for IES . . . 11

4 Measurement Processing Procedures 13
4.1 Level 1: The Raw Data Set . . . 13
4.2 Level 2: Science Data Processing . . . 13

5 Results of Calibration Activities 13
5.1 IES . . . 13
5.1.1 Efficiency decay . . . 13
5.1.2 Spectral rebinning . . . 14
5.1.3 Pedestal noise correction on SC3 and SC4 . . . 14
5.1.4 Solar noise on SC3 and its correction . . . 19
5.1.5 Failure of IES on SC2 . . . 19
5.2 IIMS . . . 23
5.2.1 Loss of the central ion detectors . . . 23
5.2.2 1st He and CNO energy channels . . . 23
5.2.3 Time-of-Flight efficiency . . . 23
5.3 Features of IIMS Series 4 . . . 28

6 Results of Cross-Calibration Activities 34
6.1 RAPID/IIMS and CIS/CODIF Cross-Calibration . . . 34
6.2 1st CNO energy channel . . . 34
6.3 RAPID/IES and PEACE Comparison: Histogram Mode Analysis . . . 39
6.4 RAPID/IES and PEACE: Electron Spectra Comparison . . . 41
6.4.1 Input data . . . 41
6.4.2 Analysis . . . 41
6.4.3 Conclusions . . . 42

7 The IES Energy Defect 43
7.1 RAPID/IES Calibration: Statistical Study . . . 43
7.2 Corrections for the Energy Defect . . . 46
7.3 Latest Determination of the IES Energy Defect . . . 46

8 Automatic Spike Removal 51
8.1 The Despiking Procedure . . . 51
8.2 Heater Spikes (Hatchets) . . . 52

9 IES Detector Decay Corrections **55**
9.1 The Previous Version and Reasons for Update . . . 55
9.2 Orbital Averages for Long-Term Calibration . . . 55
9.3 Detector-to-Detector Corrections . . . 56
9.4 Donut Correction . . . 61
9.5 Validation and Caveats . . . 61
9.5.1 Caveats . . . 63
9.6 Mission Overview . . . 64
9.7 Environmental Effects . . . 64

10 Partial Failure of IES on SC2 **68**

11 Electron Background Counts **71**
11.1 The Background . . . 71
11.2 Background Product . . . 71
11.3 Poisson Testing . . . 72
11.4 Application and Validity . . . 74
11.5 Long-Term Analysis . . . 75
11.6 Non-Cosmic-Ray Background . . . 76

12 IES Contamination in the Radiation Belts **78**

13 Accessing Data for Heavier Ions **80**
13.1 Direct Events (DE) . . . 80
13.2 The MTRX and RMTRX Products . . . 82

14 Summary **85**

A Calculation of Fluxes from Count Rates **86**
A.1 Geometry Factor . . . 86
A.2 Detector Efficiency . . . 86
A.3 Conversion Factor for Particle Flux . . . 87
A.4 Conversion to Differential Flux . . . 87
A.5 Calculation of Omnidirectional Flux . . . 88

B Phase Space Density Conversion **88**
B.1 Calculation of the Effective Energy for the Energy Channels . . . 89
B.2 Conversion Factors for Mean Energies . . . 90
B.3 Effective Energy and Geometric Mean Energy . . . 91
B.4 Energy Density with Geometric Mean Energy . . . 91

C Standard Deviations of Processed Data **92**
C.1 Poisson Standard Deviations . . . 92
C.2 Data Compression Errors . . . 93
C.3 Combining Standard Deviations . . . 93
C.4 Determining the Actual Standard Deviation . . . 94
C.5 The Meaning of Standard Deviation . . . 94
C.6 Error in the Calibration Factors . . . 94

D Times of ENA Mode **95**

Reference Documents

Braginsky, S. [1997]. *Characterization of the Imaging Electron Spectrometer*. Master's thesis, Boston University, College of Engineering, Boston. http://caa.esac.esa.int/documents/teams/RAPID/Braginsky_MS_Thesis_annotated.pdf.

Daly, P. W. and Kronberg, E. A. [2010]. RAPID Products at the Cluster Active Archive. In *The Cluster Active Archive, Studying the Earth's Space Plasma Environment*, edited by H. Laakso, M. G. T. T. Taylor, and C. P. Escoubet, Astrophysics and Space Science Proceedings, pp. 145–158. Springer, Berlin. DOI: 10.1007/978-90-481-3499-1_9.

RAP-UG: Daly, P. W. and Kronberg, E. A. [2024]. User Guide to the RAPID Measurements in the Cluster Science Archive (CSA). *RAPID Report CAA–EST–UG–RAP, Issue 6.2*, Max-Planck-Institut für Sonnensystemforschung, Göttingen, Germany. http://caa.esac.esa.int/documents/UG/CAA_EST_UG_RAP_v62.pdf.

RAP-ICD: Daly, P. W., Mühlbachler, S., and Kronberg, E. A. [2024]. Cluster Science Archive: Interface Control Document for RAPID. *Report CAA–RAP–ICD–0001, Issue 9.0*, Max-Planck-Institut für Sonnensystemforschung, Göttingen, Germany. http://caa.esac.esa.int/documents/ICD/CAA_EST_ICD_RAP_v9.0.pdf.

Escoubet, C. P., Russell, C. T., and Schmidt, R. [1997]. The Cluster and Phoenix Missions. *Space Science Reviews*, **79**. DOI:10.1023/A:1004923124586.

Haaland, S., Daly, P. W., and Vilenius, E. [2021]. Heavy Metal and Rock in Space: Cluster RAPID Observations of Fe and Si. *J. Geophys. Res.*, **126**, e2020JA028852. DOI:10.1029/2020JA028852.

Haaland, S., Daly, P. W., Vilenius, E., Krcelic, P., and Dandouras, I. [2020]. Suprathermal Fe in the Earth's plasma environment: Cluster RAPID observations. *J. Geophys. Res.*, **125**, e2019JA027596. DOI:10.1029/2019JA027596.

Heynderickx, D., Quaghebeur, B., and Evans, H. D. R. [2002]. The ESA Space Environment Information System (SPENVIS). In *IAF abstracts, 34th COSPAR Scientific Assembly*. http://adsabs.harvard.edu/abs/2002iaf..confE.475H.

Kronberg, E. A., Rashev, M. V., Daly, P. W., Shprits, Y. Y., Turner, D. L., Drozdov, A., Dobynde, M., Kellerman, A. C., Fritz, T. A., Pierrard, V., Borremans, K., Klecker, B., and Friedel, R. [2016]. Contamination in electron observations of the silicon detector on board Cluster/RAPID/IES instrument in Earth's radiation belts and ring current. *Space Weather*, **14**, 449–462. DOI:10.1002/2016SW001369.

Kruglanski, M., de Donder, E., Messios, N., Hetey, L., Calders, S., Evans, H., and Daly, E. [2010]. Space Environment Information System (SPENVIS). In *38th COSPAR Scientific Assembly*, volume 38 of *COSPAR Meeting*, p. 8. http://adsabs.harvard.edu/abs/2010cosp...38.4176K.

Kruglanski, M., Messios, N., de Donder, E., Gamby, E., Calders, S., Hetey, L., and Evans, H. [2009]. Space Environment Information System (SPENVIS). In *EGU General Assembly Conference Abstracts*, edited by D. N. Arabelos and C. C. Tscherning, volume 11 of *EGU General Assembly Conference Abstracts*, p. 7457. http://adsabs.harvard.edu/abs/2009EGUGA..11.7457K.

RAP-FOM: [2000]. RAPID Flight Operation User Manual. *Version 3.0*, Max-Planck-Institut für Aeronomie, Katlenburg-Lindau, Germany. http://caa.esac.esa.int/documents/teams/RAPID/CL_CP_RAP_FOP_Manual__20000617_V30.pdf.

Roussos, E., Krupp, N., Paranicas, C. P., Kollmann, P., Mitchell, D. G., Krimigis, S. M., Armstrong, T. P., Went, D. R., Dougherty, M. K., and Jones, G. H. [2011]. Long- and short-term variability of Saturn's ionic radiation belts. *J. Geophys. Res.*, **116**, A02217. DOI:10.1029/2010JA015954.

Wilken, B. et al. [1997]. RAPID: The Imaging Energetic Particle Spectrometer on Cluster. In *Escoubet et al.* [1997], pp. 399–473. DOI:10.1023/A:1004994202296.

Ziegler, J. F., Biersack, J. P., and Ziegler, M. D. [2015]. *SRIM—The Stopping and Range of Ions in Matter*. James Ziegler, Chester, Maryland. ISBN 978-0-9654207-1-6.

List of Acronyms

BM	Burst Mode, Cluster high telemetry rate
CDF	Common Data Format (NASA format)
CEF	Cluster Exchange Format (CSA format)
CF	Conversion Factor
CIS	Cluster Ion Spectrometry (Cluster Experiment)
CME	Coronal Mass Ejection
CODIF	Composition Distribution Function Analyser (part of CIS)
CSA	Cluster Science Archive
ENA	Energetic Neutral Atoms
ENY	Energy Signal Rate (RAPID/IIMS)
GF	Geometry Factor
HEEA	High-Energy Electron Analyser (part of PEACE)
IES	Imaging Electron Spectrometer (part of RAPID)
IIMS	Imaging Ion Mass Spectrometer (part of RAPID)
LEEA	Low-Energy Electron Analyser (part of PEACE)
MCP	Multichannel Plate
MSF	Merged Science File (RAPID raw data)
NM	Nominal Mode, Cluster low telemetry rate
PEACE	Plasma Electron and Current Experiment (Cluster Experiment)
RAPID	Research with Adaptive Particle Imaging Detectors (Cluster Experiment)
SAA	Solar Aspect Angle
SCENIC	Spectroscopic Camera for Electrons, Neutral, and Ion Composition (part of RAPID)
SCI	SCIence file, RAPID-specific format for processed data
TCR	Triple Coincidence Rate (RAPID/IIMS)
TOF	Time-Of-Flight

1 Introduction

The CSA has the objective of archiving all the relevant scientific data, metadata, documentation, support files, etc., from the Cluster Mission (launched July-August 2000, see *Escoubet et al.* [1997] for payload description) while the Mission is still operating and the experiment teams still active.

As one of the Cluster experiments, RAPID, an imaging spectrometer for ions and electrons of energies over ~30 keV, is contributing to this effort.

One of the important activities of the RAPID team is the calibration of data. Since the start of the operations phase of Cluster in early 2001, a number of problems involving RAPID have been recognized, problems which were given only provisional solutions at the time. These problems have now been analyzed to the extent that solutions are now possible.

The purpose of this document is to outline those problems, their causes, and to show how they are to be solved. It is intended as an explanation for the CSA users on how the calibrations were done and which problems one can encounter.

A detailed description of the RAPID products at CSA is given in the RAPID Interface Control Document [RAP-ICD]; a more general overview of the products can be found in *Daly and Kronberg* [2010], and a description of how to use them in the RAPID CSA Users Guide [RAP-UG].

2 Instrument Description

The RAPID experiment is described by *Wilken et al.* [1997], and also in the Flight Operation Manual [RAP-FOM]. The RAPID instrument uses two different and independent detector systems for the detection of nuclei and electrons: The **I**maging **I**on **M**ass **S**pectrometer (IIMS) and the **I**maging **E**lectron **S**pectrometer (IES).

2.1 The IIMS Instrument

The IIMS sensor measures ions with energies from ~ 28 keV to ~ 4 MeV. The centerpiece of the IIMS sensor system is the so-called SCENIC (Spectroscopic Camera for Electrons, Neutral, and Ion Composition) detector head, shown at the right in Figure 1. In essence, this is a miniature telescope composed of a time-of-flight and an energy detection system. The particle identifying function of the SCENIC spectrometer is obtained from a two-parameter measurement: the particle's velocity V and its energy E are measured as independent quantities; the particle's mass A is then uniquely determined either by computation ($A \sim E/2$) or by statistical analysis in two-dimensional (V, E) space with the mass A as the sorting parameter. Actually the velocity detector measures the flight time T taken by the particle to travel a known distance in the detector geometry.

Each SCENIC head has a field-of-view that is 6° wide (in the direction of the spacecraft spin) and 60° in the other direction (in the plane containing the spin axis). By means of the imaging features of this instrument, the particle's incident direction is assigned to one of 4 subdivisions of this field-of-view, each of 15° height. With three detector heads in all, the full range of 0–180° is covered by 12 polar angular segments (left side of Figure 2).

There is a special mode for **energetic neutral atoms** (ENA), in which a cross voltage of up to 10 kV is applied just behind the entrance aperture, to sweep out ions of up to ~ 150 keV. In this mode, only neutral atoms are detected and processed. This mode has only been used on SC4 in the solar wind during the first two years of operation, as listed in Appendix D.

A major problem with the IIMS instrument is that the middle detector heads rapidly lost all efficiency, so that the full 3-D distributions are incomplete, and exhibit a hole in the middle, the so-called "donut" effect (Section 5.2.1).

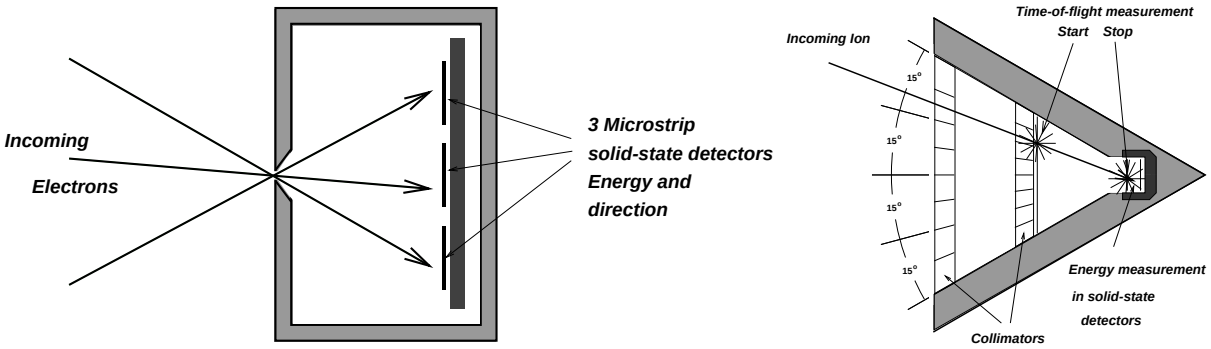

Figure 1: Left: One of the three IES heads, containing three solid state detectors to determine the direction of the incoming detected electron to within 20°. Right: One of the three SCENIC heads making up the IIMS part of RAPID. Shown is an incoming ion that triggers a start signal at a foil, which also serves to determine the fine direction, and a stop signal when it enters the solid state detector, where its energy is measured.

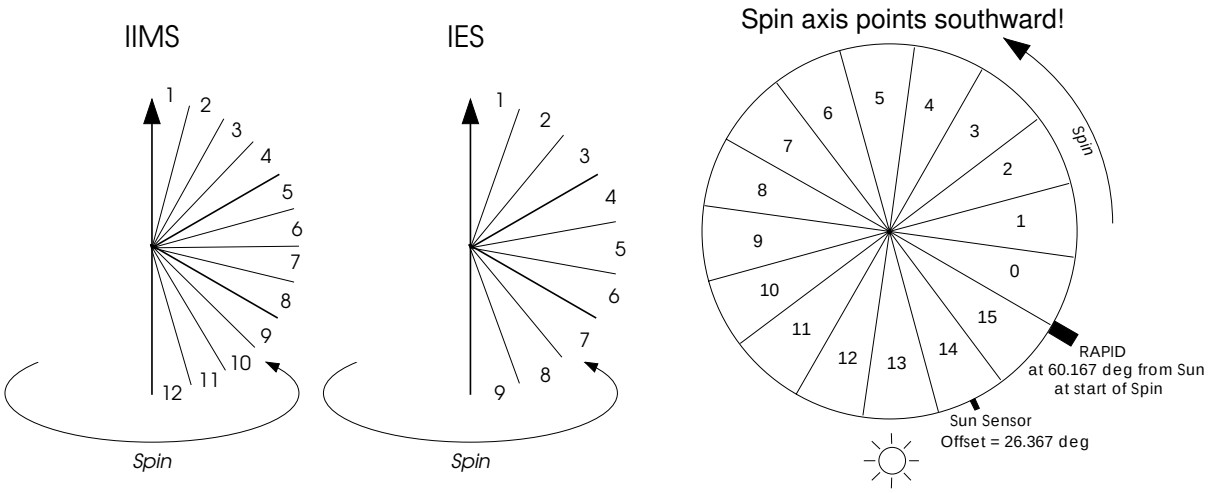

Figure 2: The IIMS and IES polar segments relative to the spin axis (left and center) and the RAPID sectorization relative to the sun (right). *Note that the spin axis actually points towards the $-Z$ GSE axis (southward).*

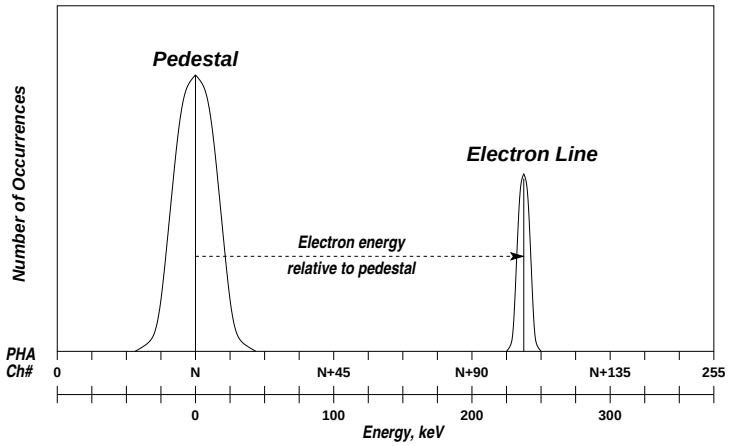

Figure 3: An idealized histogram plot for IES data. The number of measurements per second is constant, depending on integration time. The majority of measurements are empty, contain just a background charge but no electrons, and they form the *pedestal* (large peak at left). True electrons deposit an additional charge, so that a monoenergetic beam could create the peak at the right. The center of the pedestal thus corresponds to the zero of energy.

2.2 The IES Instrument

Electrons with energies from $\sim$ 30 keV to $\sim$ 400 keV are measured with the IES (Imaging Electron Spectrometer). Advanced microstrip solid state detectors having a 0.5 cm $\times$ 1.5 cm planar format with three individual elements form the image plane for three acceptance "pin-hole" systems. Each system divides a 60° segment into 3 angular intervals (Figure 1, left). Three such detector heads provide electron measurements over a 180° fan (middle of Figure 2).

Ions up to 350 keV are eliminated by an absorbing foil in front of the detectors.

The 3rd dimension, energy, is determined by the charge deposited in the detector by the absorbed electron, which is proportional to that energy (minus a constant). IES employs an integration method for this: that is, it accummulates all charges deposited during a selected integration time; the total charge (corresponding to the total energy) is then swept out and measured during a fixed read-out time, which constitutes a dead-time. Thus the total number of counts per second is constant for a given integration time. The analog signal is digitized to a bin number between 0 and 255, at 2.2 keV per bin. The number of counts in each bin can be plotted as a histogram as in Figure 3. The majority of these counts contain no real particles, but contribute to the *pedestal*, the location of zero energy. The pedestal arises because the detectors are slowly charged during the integration time by background currents. The actual 6–8 science energy channels are defined on-board in terms of the 256 bin numbers, relative to the expected location of the pedestal.

A description of the IES instrument and many of its calibration issues can be found in the thesis by *Braginsky* [1997].

2.3 Spin Sectorization

For both IIMS and IES, the azimuthal distribution of particle fluxes is obtained by sorting the counts into 16 sectors during one rotation of the spacecraft (right side of Figure 2).

The spin phase relationship between the sun sensor pulse and the start of sector 0 (the start of a new spin) is fixed so that the RAPID detectors are looking into the direction of the sun at sector 13.326, or about one third into sector 13. (This relationship has been set in agreement with the other experiments so that all start a new spin simultaneously.)

Note: For the IES heads 1 and 3, there are really only 8 sectors in the raw data. In order to simplify the dataset for the users, the processed data are put into regular rectangular matrices of 9×16. This is done by splitting each of the 8 sectors into two and by placing half the counts into each sector half. Thus for the polar directions 1–3 and 7–9, although 16 sectors exist mathematically, the fluxes in each pair (0,1), (2,3) . . . (14,15) are identical.

2.4 Accumulation Time

The RAPID detectors do not accumulate counts all the time; there is a *dead time* that leads to a *duty cycle* of less than 100%.

IIMS: in the usual *serial* mode, each ion head accumulates for a fixed 60 ms within each sector, one after the other. This means the duty cycle depends on spin rate. For a nominal 4 s spin, one sector requires 250 ms, so each head accumulates for only 24% of the time. During the remaining dead time, the counts from the previous sector are processed and other housekeeping tasks are performed.

There is also a *parallel* mode that was used early in the Mission; in this mode, all three heads accumulate simultaneously for 180 ms per sector.

In the first few months of the Mission, before the main patch was uploaded, the accumulation times were 65 and 195 ms, respectively.

IES: the total energy deposited by electrons during one *integration interval* is accumulated and then read out over the next 48 μs. The integration interval is one of 2, 5, 15, and 50 μs, depending on count rate. It is vital that at most one electron per interval is detected, otherwise it is the summed energy of multiple electrons that is registered. Thus the integration time should be as short as possible. On the other hand, it is desirable to have a long integration time to improve the duty cycle. The maximum duty cycle of $\sim$50% is achieved with an integration time of 50 μs. This is the usual case except during times of high count rates.

An autoswitching mechanism is in operation to automatically switch the integration time according to count rates.

3 Measurement Calibration Procedures

3.1 Calibration Releases

There have been four major releases of calibration data for the RAPID experiment since the launch of Cluster. These can be summarized as:

Commissioning: preliminary values prepared before the launch, suitable for the commissioning phase.

Initial Release: following commissioning, revised values and subsequent updates were applied for the initial operation phase; however it soon became apparent that the provided parameters were not capable of accommodating the observed evolution of the instrument performance.

These are the calibration parameters used for the first release of the RAPID data to CSA, and which are now considered obsolete, hence they will not be further described here.

Subsequent Releases: work on improved and more flexible calibration parameters began with systematic analysis of the instrument behaviour in flight, and an initial report on why changes were needed.

A new method of handling and maintaining calibration parameters was introduced. Whereas previously the choice and number of parameters were rigidly fixed, the new method allows additions and modifications without having to redefine and reprocess the entire set.

However, it was not until mid-2007 that reliable values for the new parameters could be safely implemented. Since then regular updates are carried out to extend the validity of the parameters up to the near present.

The *second release* of the RAPID CSA data have been produced with these calibrations, which bear the calibration version number 2. (This is the most significant digit in the dataset version number, described in Section 5.4 of RAP-UG.)

Beginning in September 2015, a complete redelivery of all datasets was started, the *third release*, bearing the calibration version number 3. This was not so much the result of a recalibration, but rather a set of systematic fixes for several issues (including bugs) that had arisen over the years. Important additions were the automatic removal of spikes (Section 8) and the correction of the decay of the IES electron detectors (Section 9) and the partial failure of IES on SC2 (Section 10).

In June 2018, after almost a year of reanalysing the IIMS ion calibrations, a new set of calibration files was ready, as the basis of the *fourth release*. At the same time, the IES electron calibrations were also upgraded for this release to include revised decay correction factors and the removal of an error in the recovery on SC2. For both ions and electrons, the calibration version number is now 4.

3.2 Calibration and Auxiliary Files

To get some impression of how calibration files are working one has to be familiar with a couple of definitions described in the following.

Calibration set: is a set of parameters needed for calculating flux from counts, valid for one spacecraft and for a given period of time.

Calibration file: is the file that the processing software reads, containing a collection of calibration sets.

The software reads this file until it finds the set that is valid for the time being processed, noting the end time as well. When the current process time exceeds this end time, the calibration file is read once more, to find the next valid set. Thus the current calibration set can change at any time, not just at day boundaries.

Calibration file series and version number: as the calibration parameters alter with time, new (time-limited) sets are added to the calibration files, which are then given a new number to distinguish them. This sequence of 3-digit numbers forms a series, all beginning with the same digit.

When a major change to the calibrations takes place, a reevaluation of all parameters from the beginning, then a new series is initiated, with a new first digit. Currently the calibration files are numbered 4*xx* (series 4), replacing the existing series 3 ones at CSA.

The series number is equivalent to the *calibration version number* that is the first digit of the dataset version (Section 5.4 in RAP-UG, and also in RAP-ICD).

This complicated arrangement has the advantage that per spacecraft and IIMS/IES, there is only one calibration file containing all the time-dependent changes in any of the parameters. This avoids having several files valid for only certain times. The RAPID calibration files as a whole are valid for all times up to a certain expiry date, although the individual sets within them may have limited validity.

For Cluster/RAPID science data users, it is also important to understand the relationship between count rates and fluxes. A description of the procedures to convert raw counts into differential fluxes using geometry factors and detector efficiency, as well as the calculation of omnidirectional flux, can be found in Appendix A.

3.3 The Calibration Procedure for IIMS

The IIMS calibration files are produced in three steps:

1. A *basic* set of calibration files is made containing all the fixed or well-determined parameters. This includes the pure geometrical factor, the ideal TOF efficiencies, the accumulation times, and the MCP voltages. With this, the 3-D count rates, the direct events, and the diagnostic “singles” are generated.
2. The next step is to produce the *preliminary* calibration files.

- From the direct events, we find the fraction of counts (per species and energy channel) in each of the 12 directions, to give the *directional distribution*, or DD parameters. This indicates how well the different heads and sub-directions are working, relative to one another.
- From the singles, we get the TOF efficiency as described in Section 5.2.3, the TE factors, one value per spacecraft and day, but only for sufficiently high correlations.

A linear fit with time is carried out for each of these factors. Suitable break-points for the fitting intervals are set when the MCP voltage changes, or when a visual inspection indicates that the linear change with time is no longer reasonable.

The resulting sets of fit parameters then go into the next calibration files. These are used to produce *preliminary* 3-D fluxes.

3. The *final* calibration files are now generated to include cross-spacecraft parameters XS. The orbit-averaged fluxes on all the functioning heads are normalized to their mean value and the normalization factors are subjected to a linear fit over time. These fit parameters now conclude the calibration procedure.

It might be objected that the last step is designed to remove not only all anisotropies but also any differences between the spacecraft. This would be true if it were done for each data point. However, the linear fitting guarantees that only the long-term averages (over weeks or months) are made uniform. Any individual time period can exhibit large anisotropies and spatial differences.

Note that only the final calibration files are released for use by the outside community. The basic and preliminary files are used only internally by the RAPID Team.

The calibration files are extended in time as new data become available.

3.4 The Calibration Procedure for IES

The basic set of parameters for IES are as follows:

Geometry factors are 2.22×10^{-3} cm^2·sr for the "outer" detectors of each head (1, 3, 4, 6, 7, 9) and 2.23×10^{-3} cm^2·sr for the "inner" detectors (2, 5, 8).

Energy conversion is 2.2 keV per bin (Figure 3).

Detection efficiency is taken to be 100%.

Dead layer loss is 6.5 keV. Originally this was taken to be a constant but it has now become apparent that it increases at lower energies (<50 keV), requiring a redefinition of the lowest energy thresholds (Section 7).

There are additional parameters to handle special problems that have arisen since the start of the mission, such as pedestal noise (Section 5.1.3) and solar contamination (Section 5.1.4).

Furthermore, starting about 2007, there is an increasing efficiency decay in all detectors, which is strongly dependent on the angle to the spin axis. Additional time-dependent corrections factors need to be determined and applied (Section 9).

What is periodically changed is the definition of the energy channels in terms of the 256 bin numbers. These are set with the integer parameters:

- P, the bin number of the center of the the pedestal,
- S, the width of the pedestal, in bins,
- $B_1, \ldots B_8$, the upper limits to the 8 energy channels, relative to P.

The lower limit of channel 1 is then $P + 2S$; this is set not only relative to the pedestal position, but also to its width. For channel n ($n > 1$) the lower limit becomes $P + B_{n-1}$. The upper limit of channel n (including 1) is $P + B_n - 1$, one less than the next lower limit.

Since P represents the bin with zero energy, each bin N corresponds to an electron energy in keV of

$$2.2 * (N - P) + 6.5 + \text{energy defect.}$$

See Section 7 for information on the energy defect. For most cases, we have $S = 7$, which leads to a threshold for energy channel 1 of $2.2 * 14 + 6.5 = 37.3$ keV, without the energy defect. When the energy defect of 1.9 keV is added, we have a value of 39.2 keV, the current ideal value to which all electron spectra are standardized.

The P and S parameters are given for each detector and integration time, as can be seen for example in Figure 5; the B parameters exist once per spacecraft, and, since the initial commissioning set, are the same on all spacecraft. What needs to be changed with time are the P and S values as the pedestals shift and widen. Table 1 lists the different sets used so far.

Table 1: Dates when different energy channel definitions came into effect

Nr.	Description	SC1	SC2	SC3	SC4
1	Initial values set before launch, used at start	–	–	–	–
2	Post-Commissioning, first corrected values	2001-05-18	2001-05-18	2001-04-26	2001-05-18
3	Further corrected values	2002-07-25	2002-07-23	2002-07-23	2002-07-30
4	Major change to make S values as uniform as possible	2006-09-21	2006-09-21	2006-08-28	2006-09-19
5	Corrections to P values to allow for long-term pedestal shifting	2011-11-01	2011-10-28	2011-11-01	2011-10-28
6	Corrections to P for further long-term shifting	2013-11-05	2013-11-06	2013-11-06	2013-11-06
7	Fine-tuning P values for SC1	2014-03-14	—	—	—
8	Minor adjustments to SC1, SC3, SC4; major shifts on SC2 following partial failure (Section 10)	2016-05-09	2016-05-09	2016-05-09	2016-05-09
9	Fine-tuning to P all SC	2017-03-01	2017-03-01	2017-03-01	2017-03-01
10	Fine-tuning to P all SC	2018-02-07	2018-02-08	2018-02-08	2018-02-06
11	Fine-tuning to P all SC	2018-09-18	2018-09-17	2018-09-18	2018-09-17
12	Fine-tuning to P all SC	2019-09-12	2019-09-12	2019-09-12	2019-09-12
13	Fine-tuning to P all SC	2020-09-12	2020-09-12	2020-09-12	2020-09-12
14	Fine-tuning to P all SC	2020-10-21	2020-10-23	2020-10-21	2020-10-21
15	Fine-tuning to P all SC	2021-09-12	2021-09-12	2021-09-12	2021-09-12
16	Fine-tuning to P all SC	2022-03-15	2022-03-15	2022-03-15	2022-03-15
17	Fine-tuning to P all SC	2023-05-30	2023-06-01	2023-05-25	2023-06-01
17b	Correction to one value on SC3	—	—	2023-06-30	—

With set 4, S was set to be 7 for all cases, except where the pedestal was too wide to allow this (see also Section 5.1.3). This value of 7 is used even when the pedestal width is in fact much narrower. The reason is to standardize the channel 1 values. Previously they varied considerably, which made the spectral realignment to the ideal thresholds less reliable.

4 Measurement Processing Procedures

4.1 Level 1: The Raw Data Set

The RAPID data ground processing begins by merging the raw data from the CD-ROMs (level 0) to *Merged Science Files* (MSF, or level 1). Each such file contains the RAPID raw data for one spacecraft for a single day, regardless of how many CDs originally contributed to it. Records of instrument housekeeping data, spacecraft housekeeping data, and instrument science data (nominal or burst mode, whichever is current) are interspersed on a common time basis. Whereas the instrument data records are identical to those on the CD-ROMs, the spacecraft housekeeping records are limited to the needed for processing sun reference pulse data plus a temperature byte.

4.2 Level 2: Science Data Processing

A particle instrument like RAPID delivers only a set of counts accumulated over a known time period. Thus, after having processed the raw data set to the so-called MSF, the data have to be calibrated before providing them to the CSA. The standard RAPID software (`MSF2SCI`) produces counts-per-sec or fluxes from the MSF data and calibration files. These are written to files in an ASCII format specific to RAPID (called SCI files), for further processing, plotting, analysis. For CSA, there is a conversion program to put them into CEF (Cluster Exchange Format) which allows subsequent conversion to CDF with existing software.

Calibration is performed with one file per spacecraft and particle type (electron/ions) for 8 in all. Each one contains all the temporal changes to the various parameters. In addition to the raw data processing, caveat and instrument mode files are provided. Knowledge of the instrument mode is required to understand the products. Caveats give information about instrument behaviour, explanations for problems, warnings when the data are unreliable, and why.

5 Results of Calibration Activities

5.1 IES

Features in electron calibrations

- Decay in the IES detector efficiencies starting about 2007, strongest in those detectors looking perpendicular to the spin axis
- Correction of the spectral data (rebinning) to put all detectors on to a common set of energy thresholds. This compensates for:
  - actual differences in the energy channel definitions
  - spectral shifts that depend on (among others) count rate and aging
- Pedestal noise in some detectors on SC3 and SC4
- Solar noise in some detectors on SC3
- Failure of 6 of the 9 detectors on SC2 in 2015.

5.1.1 Efficiency decay

It has been discovered that starting about 2007 there is a loss of detector efficiency that is symmetric about the plane perpendicular to the spin axis. As described in detail in Section 9, time-dependent correction factors are determined for each IES detector and energy channel. These factors are the reduced efficiency, going from 100% for no decay, to 0% for a completely dead detector.

These corrections are applied to the calibration parameters as an additional multiplier to the geometry factors. Thus when converting from count rates to fluxes by dividing by the GF, (Equation 18 on page 86) a higher flux

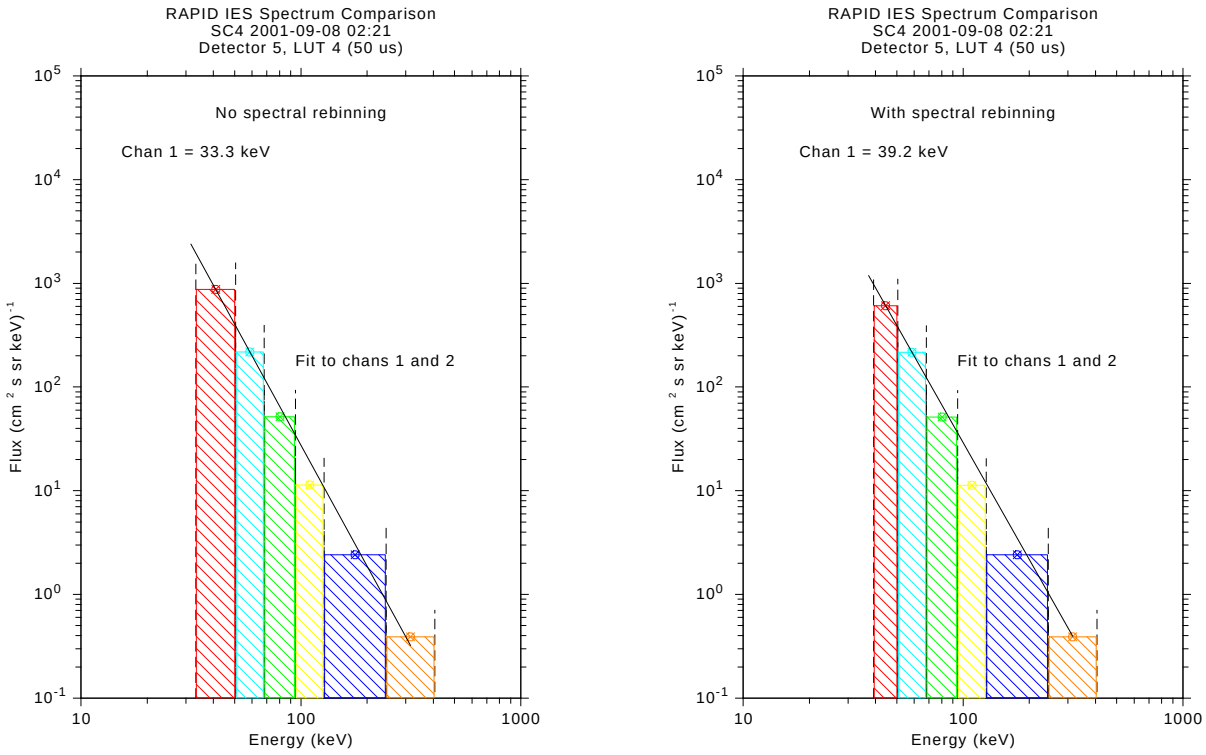

Figure 4: Illustration of rebinning to a standard energy threshold. The spectra on the left is the original raw data, with a threshold for energy channel 1 of 33.3 keV, while that on the right is the "corrected" spectra with the target threshold of 39.2 keV. (Note that the shaded area in each energy channel represents the measured integral flux while the height of the bar is the mean differential flux over that channel.)

will be obtained for the same count rate, as compensation for the reduced detector efficiency, and corresponding lower count rate.

As always, only the fluxes are corrected; the count rates are left as raw original data.

5.1.2 Spectral rebinning

Since as mentioned above the thresholds of the IES energy channels do vary among themselves and with pedestal shifting, it is desirable to correct the measured spectra so that they all are based on a uniform set of values.

The rebinning is illustrated in Figure 4. The spectrum on the left is with the original raw data, and the lower threshold of energy channel 1 is 33.3 keV. A power law is fitted to channels 1 and 2, such that the integral over each channel reproduces the measured integral fluxes (the shaded areas). The value of that power law at the target threshold of 39.2 keV is used to obtain the corrected flux in channel 1 in the spectrum on the right. If the power law is now recalculated on the right, the same result is achieved as on the left.

A similar procedure is used to shift the boundary between the other channels: a power law is fitted to two adjacent channels, it is integrated over the shifted energy between them, and that integrated flux is added to the one and subtracted from the other channel. This is shown more clearly in Section 4.3 in RAP-UG.

5.1.3 Pedestal noise correction on SC3 and SC4

For some of the IES detector strips on SC3 and SC4, there are times when the pedestal is so broad that it contaminates the lowest science energy channels (Figure 5). This noise cannot be corrected for, since it is greater than

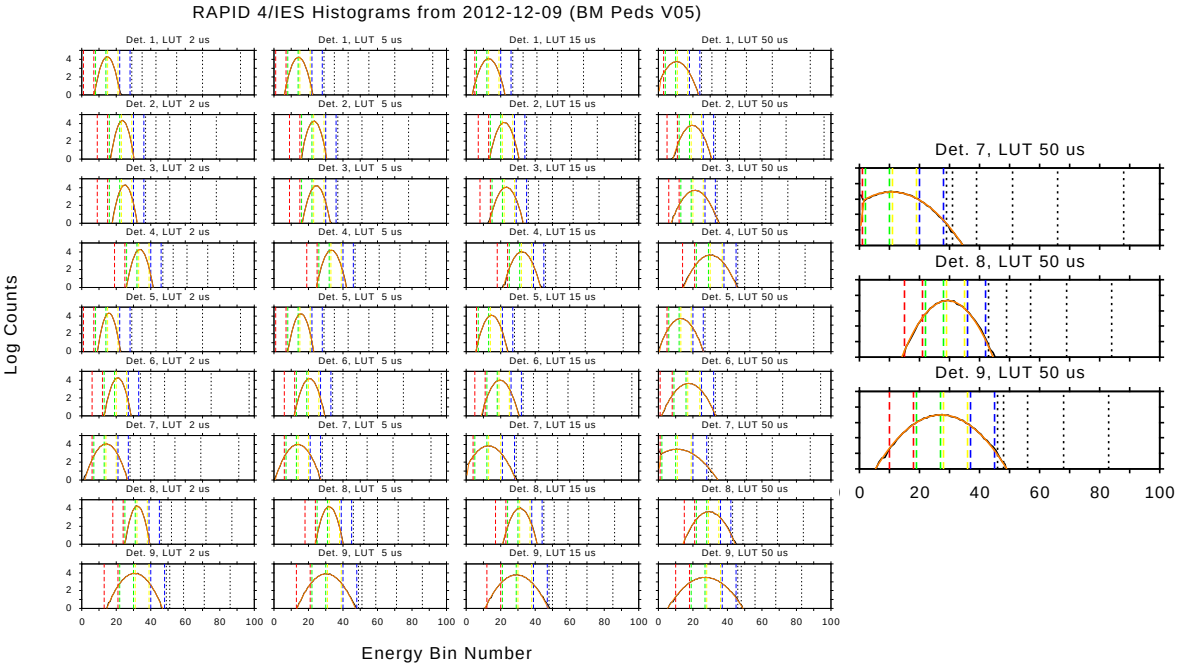

Figure 5: Histogram plots from SC4 on 2012-12-09, for each detector and integration time. The pedestal is especially broad for 50 μs (right column) in detectors 7, 8, and 9 (see blow-up at right). The energy channel boundaries are indicated with black dashed lines. One sees how the pedestal extends to the first energy channel for detector 8, and even into the second one for detectors 7 and 9.

expected signals, so for these times the noisy channels are simply removed by setting them to fill values, as listed in Table 2. This affects both the 3-D data (example in Figure 6) as well as the omnidirectional data.

The result of this pedestal noise correction is shown in summary plots in Figure 7, where the upper panel still contains the noise, and the lower panel has the noisy detectors removed.

Corrections, as always, are made for the fluxes only, never for the count rates.

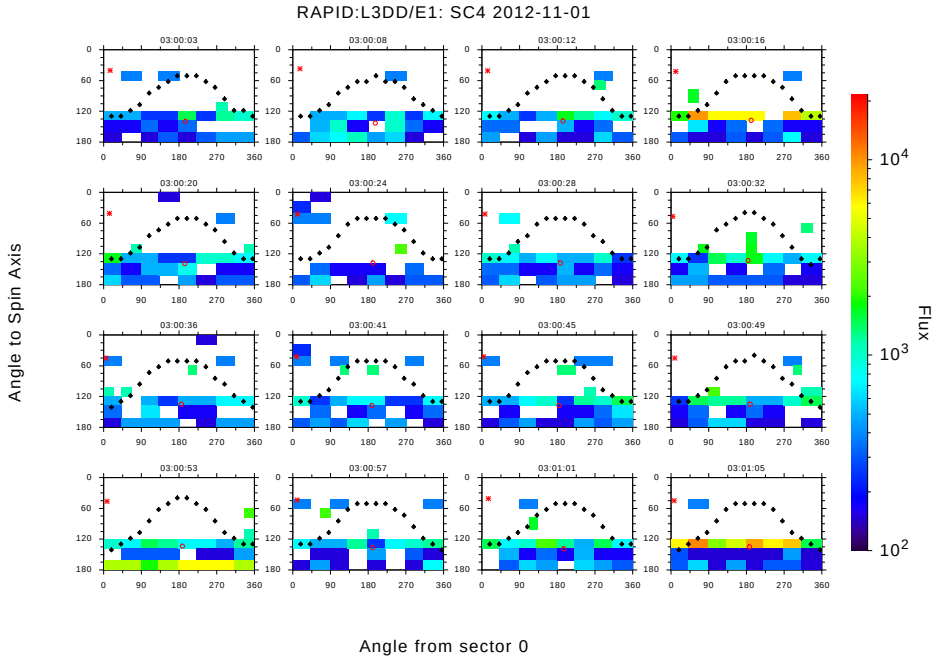

Figure 6: Angle-angle plots in spacecraft frame for SC4, energy channel 1, without eliminating the dominating pedestal noise, which produces the enhanced rates in detectors 7, 8, and 9, the horizontal stripes near the bottom of each panel. In the actual data at CSA, these noisy data are removed, i.e. set to fill values, and we only see background levels.

Table 2: Detectors/channels removed because of pedestal noise

Start Date	Detector	Int. Times	Channels
SC3:			
2004-10-01	5, 8	50 μs	1
2005-05-01	–	–	–
2009-11-01	7	50 μs	1
2011-04-15	–	–	–
SC4:			
Launch	7	50 μs	1
2001-05-18	–	–	–
2003-09-03	9	all	1
2006-09-19	7	50 μs	1
	9	50 μs	1
2007-09-01	7	50 μs	1, 2
2012-05-01	7	50 μs	1, 2
	9	50 μs	1
2012-10-01	7	50 μs	1, 2
	8	50 μs	1
	9	50 μs	1, 2
2017-04-01	7	50 μs	1
	8	50 μs	1
	9	50 μs	1, 2
2018-02-06	7	50 μs	1, 2
	8	50 μs	1
	9	50 μs	1, 2
2019-09-01	7	50 μs	1, 2
	8	50 μs	1
	9	50 μs	1
2020-04-01	7	50 μs	1, 2
	8	50 μs	1
	9	50 μs	1, 2
2020-07-01	7	50 μs	1
	8	50 μs	1
	9	50 μs	1, 2
2020-10-21	7	50 μs	1, 2
	8	50 μs	1
	9	50 μs	1, 2
2021-11-01	7	50 μs	1, 2
	8	50 μs	1
	9	50 μs	1
2023-05-01	7	50 μs	1, 2
	8	50 μs	1
	9	50 μs	1, 2

Last change made August 2023

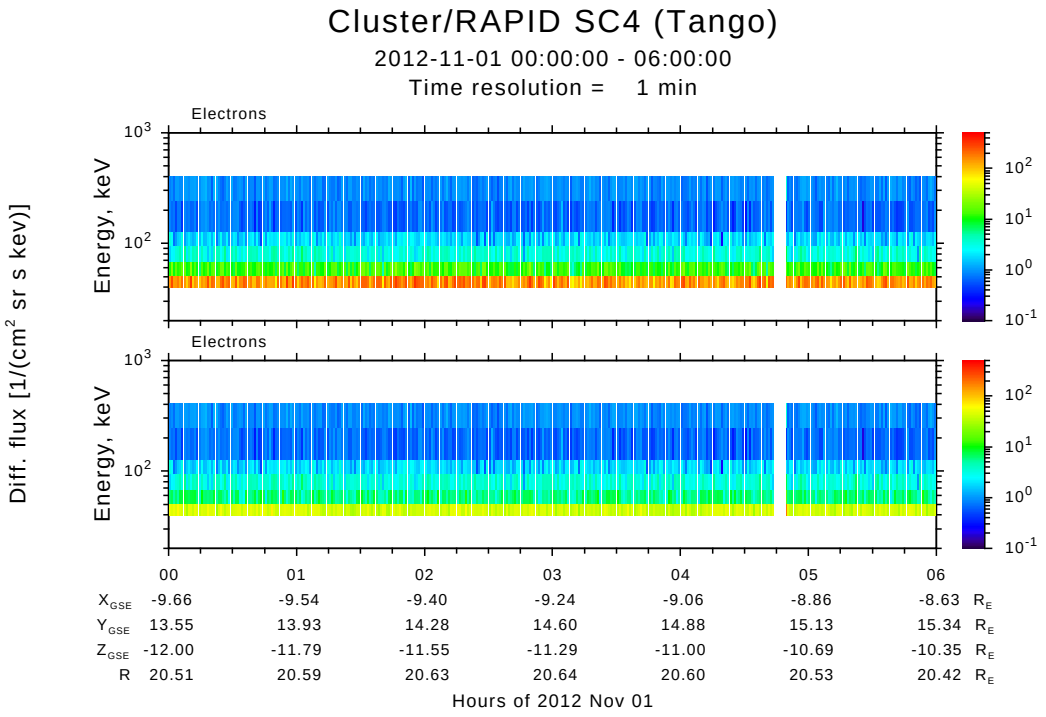

Figure 7: Pedestal noise correction for the omnidirectional electron fluxes. Without correction in the upper panel and with pedestal noise removed in the lower panel.

5.1.4 Solar noise on SC3 and its correction

Sunlight enters the IES head 1 on SC3. This solar noise is very strongly dependent on solar aspect angle (SAA), as shown in Figure 8. It is worst when SAA <94.6°, which is why the range of SAA has been shifted relative to the other spacecraft since Sep 2005. (But see note below for latest development.)

A method for correcting this noise has been developed. During quiet burst mode times, when no other activity is present, the noise in the SC3 electron head 1 can be measured. As seen from Figure 8, the dependence on SAA is reproducible over many sweeps of SAA (it oscillates with a period of several weeks). Having established this dependence, it is possible to determine the noise for all intervals over this long period, even when quiet burst mode is not occurring. The result is a calibration file with the solar noise values for every day. The solar noise is subtracted from the actual measurements, and if the result is less than 3 standard deviations, the value is set to the fill value. This correction is made to both the 3-D (see the examples of uncorrected and corrected data in Figures 9 and 10, respectively) and omnidirectional flux data (see the examples of uncorrected (left) and corrected data (right) in Figure 11).

Once again, the count rates are not corrected at all, since these are meant to be raw data.

Important note: up until May 2014, the spin axes on all 4 spacecraft have been regularly adjusted every few months to maintain the desired range of SAA values. However, on May 19, 2014, the last such manoeuvre was carried out, setting all the spin axes to a fixed direction in celestial coordinates; this direction will only change slightly in future due to tidal effects from the moon and sun. As a result, the solar aspect angle will in the course of a year oscillate between 87.6°–92.4°.

Already on May 1, 2014, the SAA on SC3 crossed the critical value of 94.6°, and the solar noise increased considerably. The manoeuvre of May 19 set the SAA to 88.2°, resulting in extremely large noise *in all energy channels* (lower plot in Figure 8). This is expected to stay this way for the rest of the mission. (The fixed spin axes have been set to avoid an unfavourable configuration becoming permanent when the remaining fuel on board finally runs out. This is not a temporary measure.)

5.1.5 Failure of IES on SC2

On March 26, 2015, there was a failure of the IES instrument on board SC2. Three of the 9 detectors did gradually recover and are still usable, albeit with caveats.

This *partial failure* (or alternatively *partial recovery*) is described in more detail in Section 10.

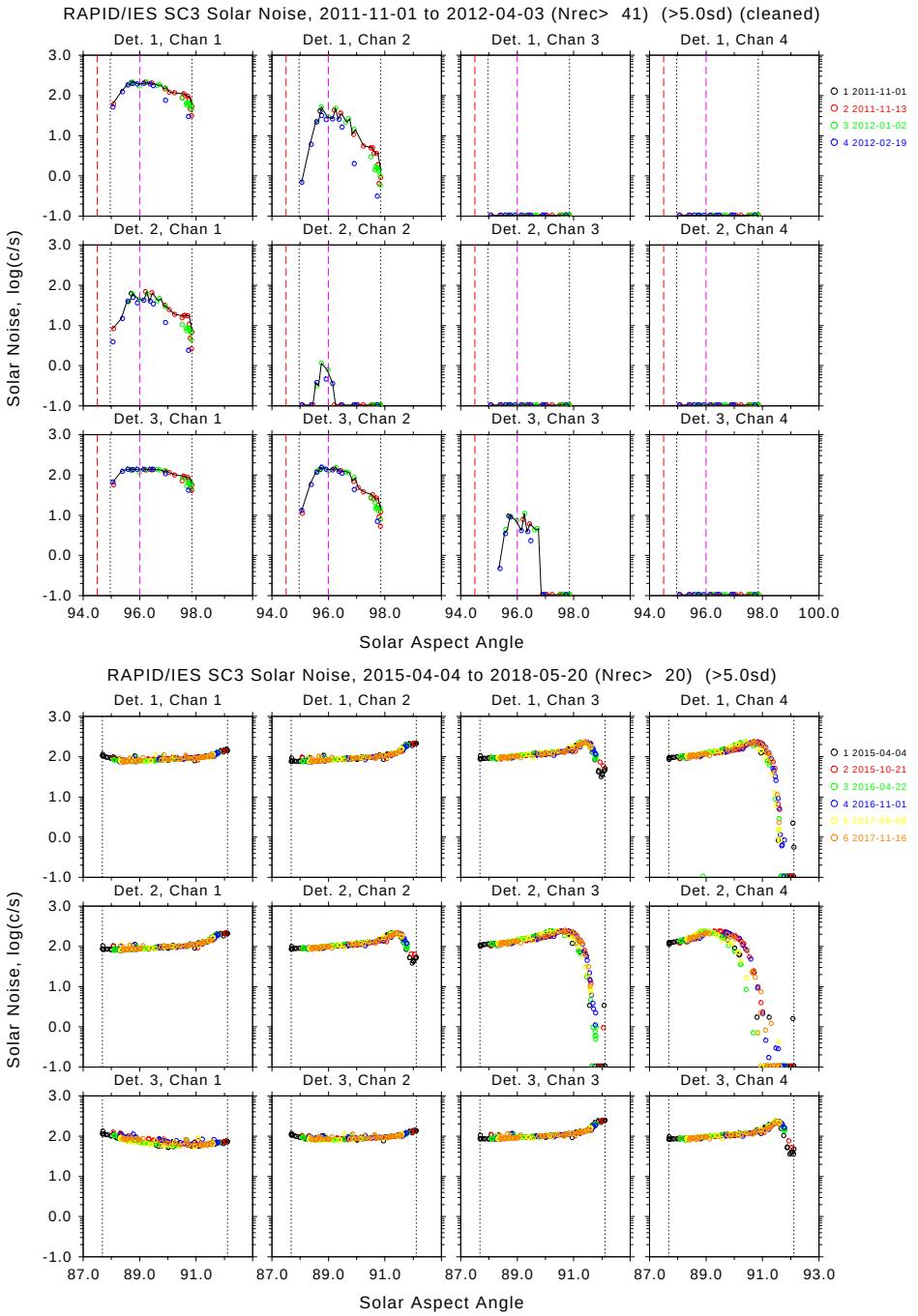

Figure 8: The dependence of the solar noise on SC3 with solar aspect angle (SAA). The plots show the noise for 3 detectors and 4 energy channels. The upper plot is is from a time when the range of SAA on SC3 was shifted to accommodate RAPID (as well as could be done), while the lower plot shows data from 3 years after the space orientations were fixed and the SAA sweeps over the full range over one year. The different colours indicated different sweeps. It is clear that the dependence is reproducible over many sweeps, except for parts of detector 2, channel 4.

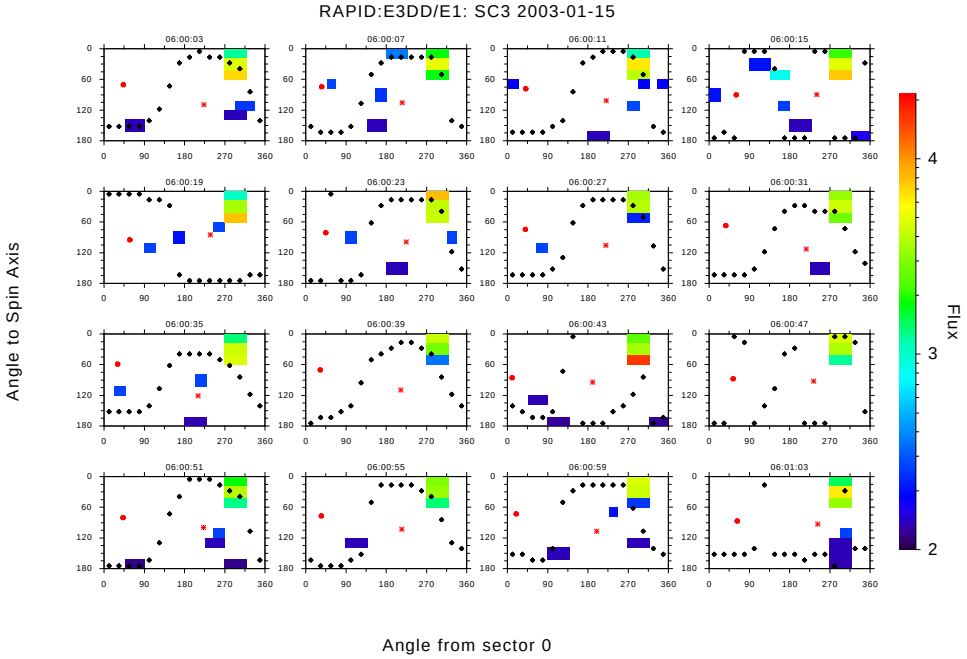

Figure 9: Angle-angle plots, solar noise without correction, SAA=93.8°.

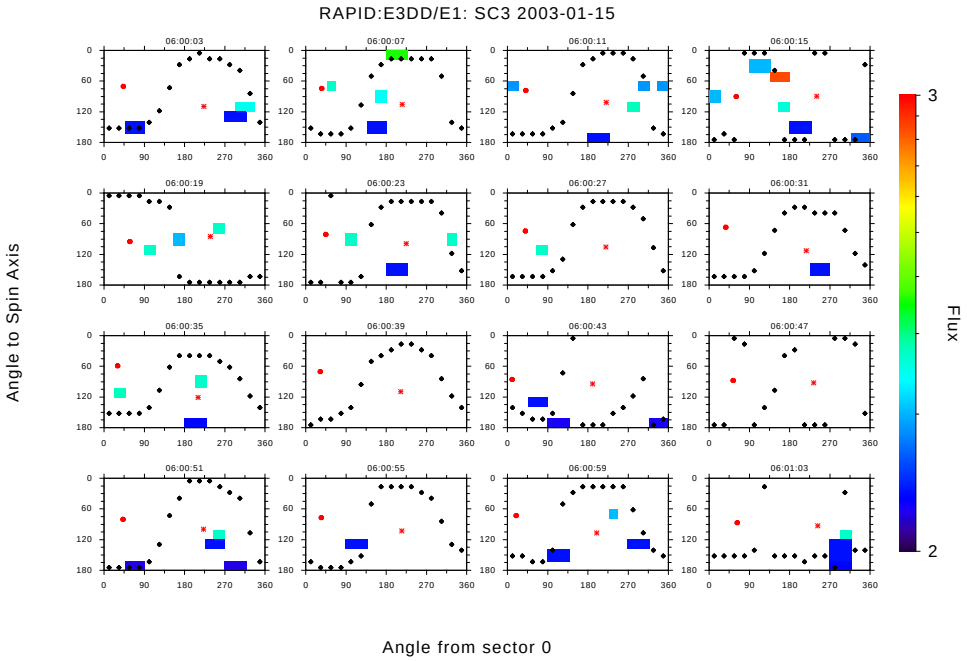

Figure 10: Angle-angle plots, solar noise is removed.

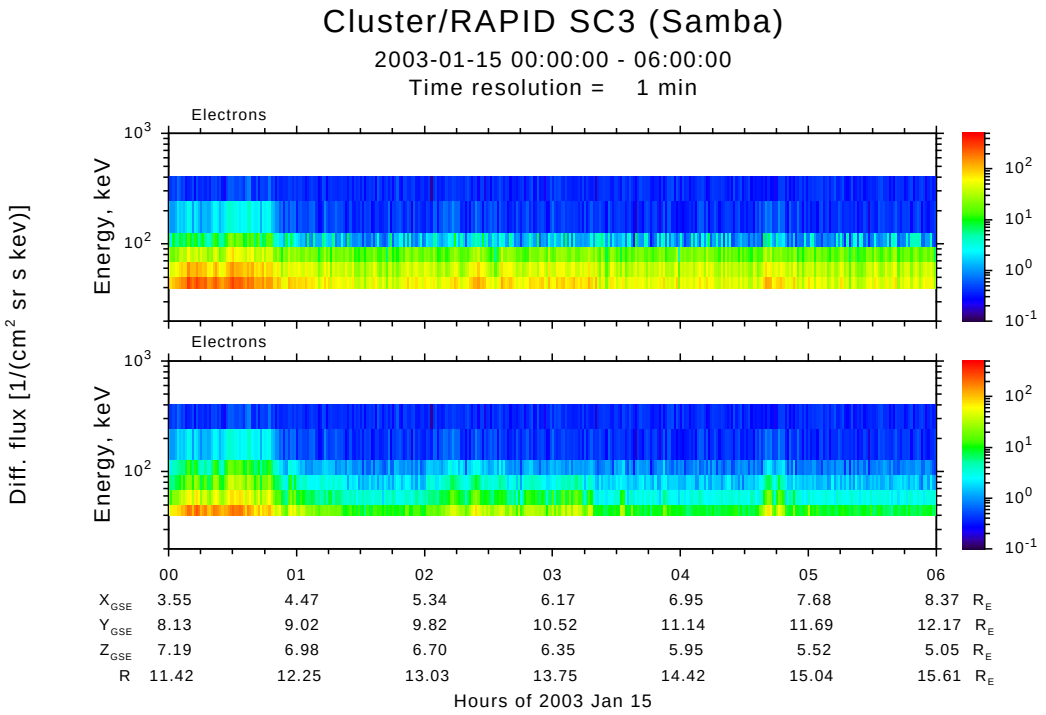

Figure 11: Solar noise correction for the omnidirectional fluxes. Without correction (top) and with correction (bottom).

5.2 IIMS

Features in ion calibrations

Initially a very over-simplistic model of the IIMS instrument was used to get the starting calibration parameters. Once a actual database was available, more realistic aspects could be included, the basis of the 2nd release to CSA:

- Redefine the ion energy channel thresholds
  - In particular, establish that there is a gap between the 1st and 2nd H channels
  - . . . and that the 8th H and He channels are always empty (geom.factor=0)
  - . . . and that the 1st He channel contains mainly H (later it was found that the 1st CNO channel is also mainly H)
- Determine the relationship between omnidirectional and 3-D data (i.e. the efficiency for directional signals)
- Determine the time dependence of the time-of-flight efficiency

5.2.1 Loss of the central ion detectors—"Donut effect"

Within the first few months of operations in 2001, it was immediately noticed that the middle detector heads on all 4 spacecraft rapidly lost detection efficiency, and were no longer available for delivering data at all. Efforts to counteract this by increasing the high voltage on the MCPs only provided a short respite before they decayed once more, as can be seen in Figure 16.

Since these are the heads that look directly towards the sun, it is thought that the MPCs were saturated by photo-electrons produced from sunlight falling on the start foils, and not by sunlight falling directly on the solid state detectors, which otherwise seem to be working fine. However, without the start and stop signals from the MPCs, the time-of-flight mechanism cannot function and the ions cannot be identified. The 3-D distributions are thus missing all data near the perpendicular to the spin axis, i.e., the ecliptic plane.

This is referred to as the "donut" effect, since the distributions have a hole in their middle.

5.2.2 1st He and CNO energy channels

The first He energy channel is in the "underrange" region, where no energy signal is received (see the lower part of Figure 12) and as a consequence the ion classification is done only on TOF information. It has long been recognized that this channel is strongly contaminated by low energy protons. Therefore, the data have been removed by setting them to fill values.

It has since been recognized that even the first CNO energy channel is also contaminated (Section 6.2); as a result, the ion calibration version 3 (3rd release) also set this to fill values.

5.2.3 Time-of-Flight efficiency

A means to estimate the TOF (time-of-flight) efficiency factor (and thus the overall ion response) was developed mid-2006.

Figure 13 shows the ideal TOF efficiencies for H, He, and CNO as a function of incoming ion energy. These curves were generated from laboratory measurements on the RAPID flight units.

To correct for degradation with time, and improvement with increasing voltage on the MCPs, we plot the "triple coincidence rate" (start, stop, plus energy signal, available in the SGLs data product, see RAP-ICD) against the rate of energy signals alone (Figure 14). There are times when these are very strongly correlated; but usually they are a scatter plot. Only the times of high correlations are used; these can be hard to find, especially in summer when Cluster is in the tail.

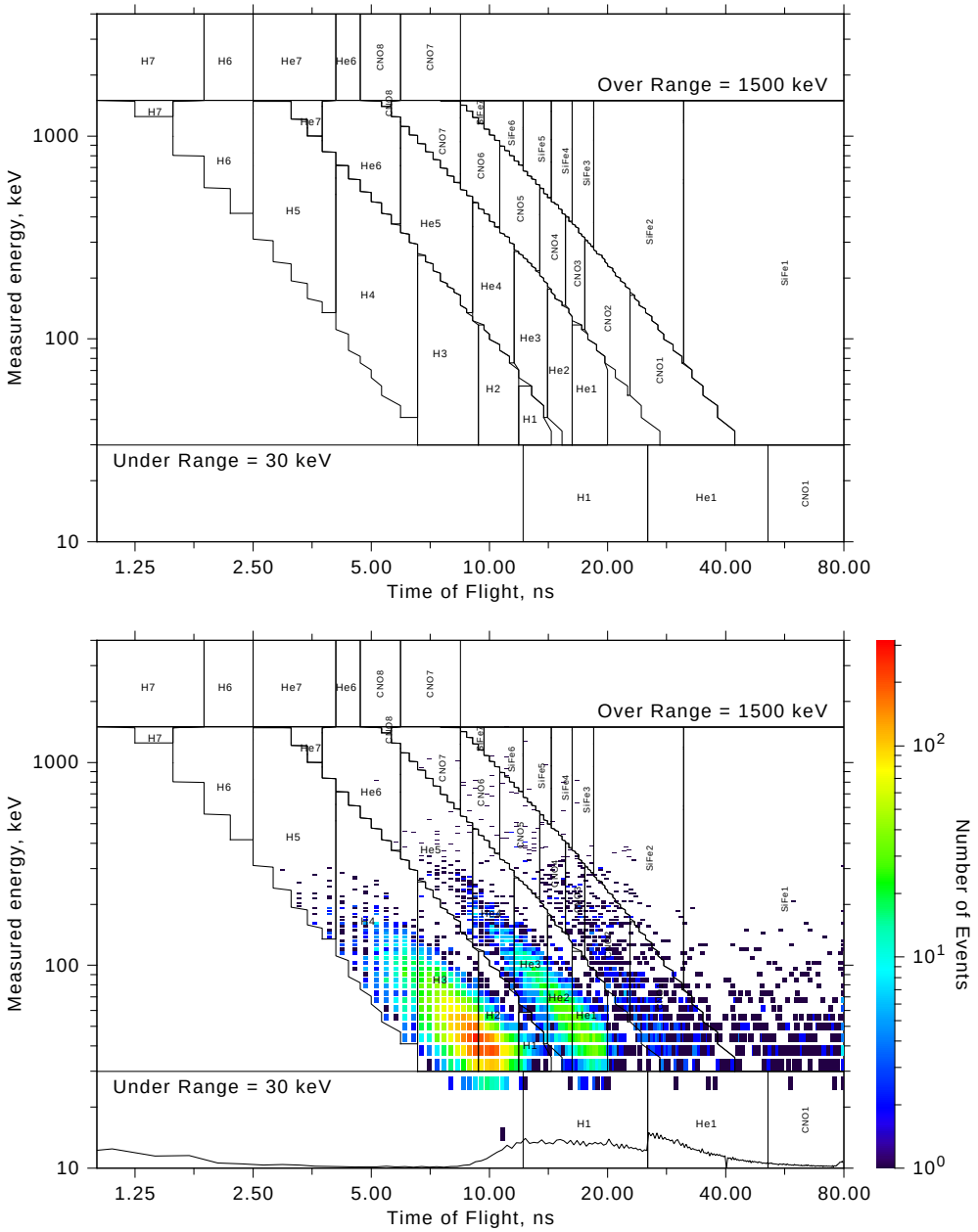

Figure 12: The RAPID ion classification system. Every ion "event" occupies a point in the 256×256 energy-TOF space, which is divided into areas for different ion species and up to 8 energy channels. For events of (internal) energy < 30 keV, no energy signal is produced. In this "underrange" region, species determination is done solely with TOF and the fact that the energy is below this threshold.
The upper panel above shows the arrangement of species-channel areas, without any particles, while the lower panel is exactly the same thing but with real direct event data (CP_RAP_DE) added. One sees the clear separation between the three species. In the underrange area, where energy information is missing, only a normalized intensity curve is shown. The large jump in this curve at the boundary between H1 and He1 is a result of the prioritization system (only a limited number of direct events per spin are accepted, and heavier ions are taken preferentially, see Appendix B in RAP-ICD.)

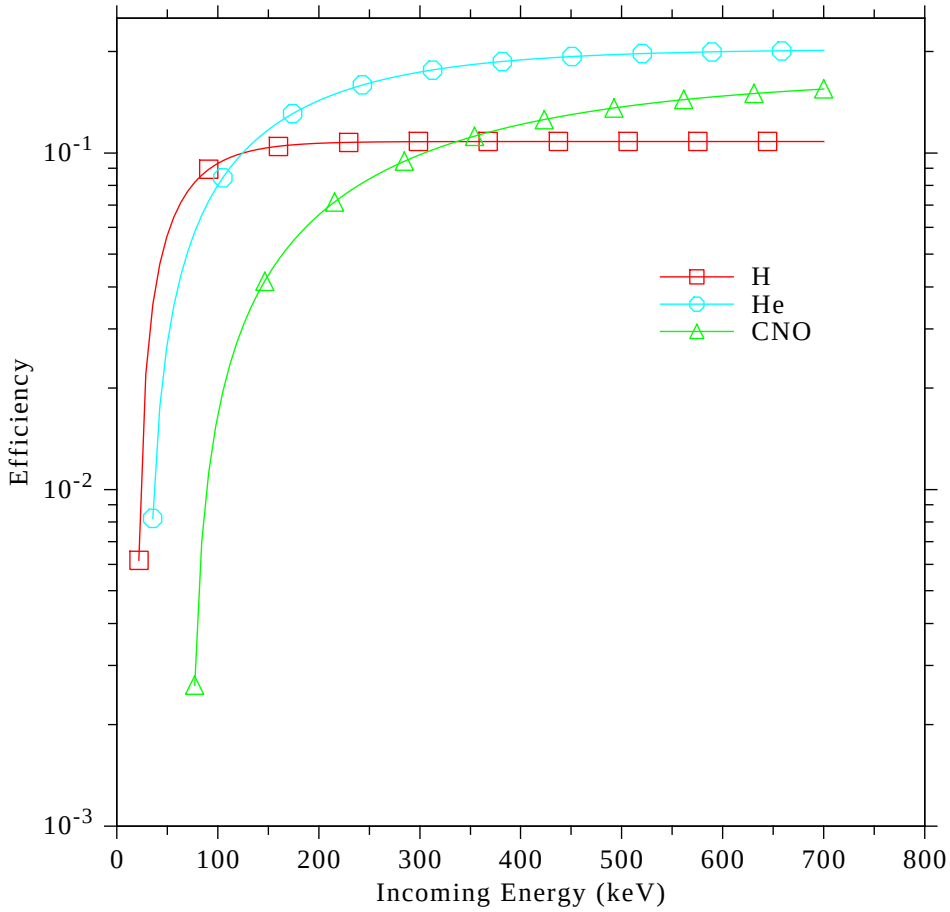

Figure 13: The ideal time-of-flight efficiencies as a function of incoming energy, for each of the three major ion species. These curves are based on laboratory measurements made on the RAPID units prior to launch.

The ideal efficiencies in Figure 13 are used to produce basic geometry factors for each species and energy channel. The true geometry factors are then corrected by the current slope of TCR vs ENY rates relative to its value of 0.5 during commissioning.

The resulting efficiencies behave as expected: they go down after manoeuvres and go up after the high voltages on the MCPs are increased, as shown in Figure 15 for 2004.

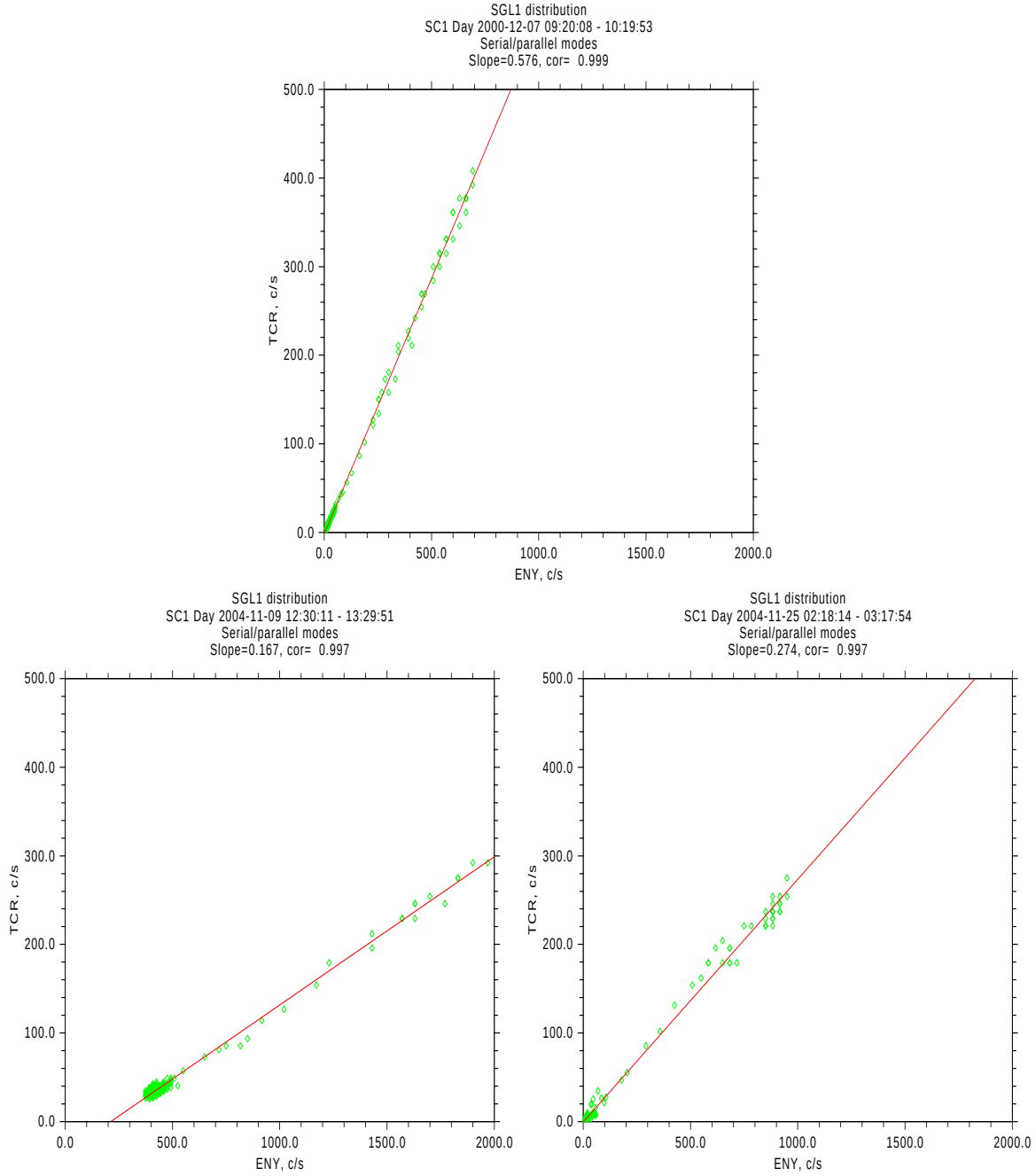

Figure 14: Plots of triple coincidence rate (TCR) versus energy signal rate (ENY) for selected times on SC1. The fitted slope is used to measure the TOF efficiency. The top panel is from the end of the commissioning phase, when the efficiency is considered to be optimal (slope = 0.567). The middle and bottom panels are taken just before and after the increase in MCP voltage on Nov. 15, 2004, indicating the improvement in efficiency (0.167 → 0.274). (See Figure 15 for the fitted slopes over the entire year 2004.)

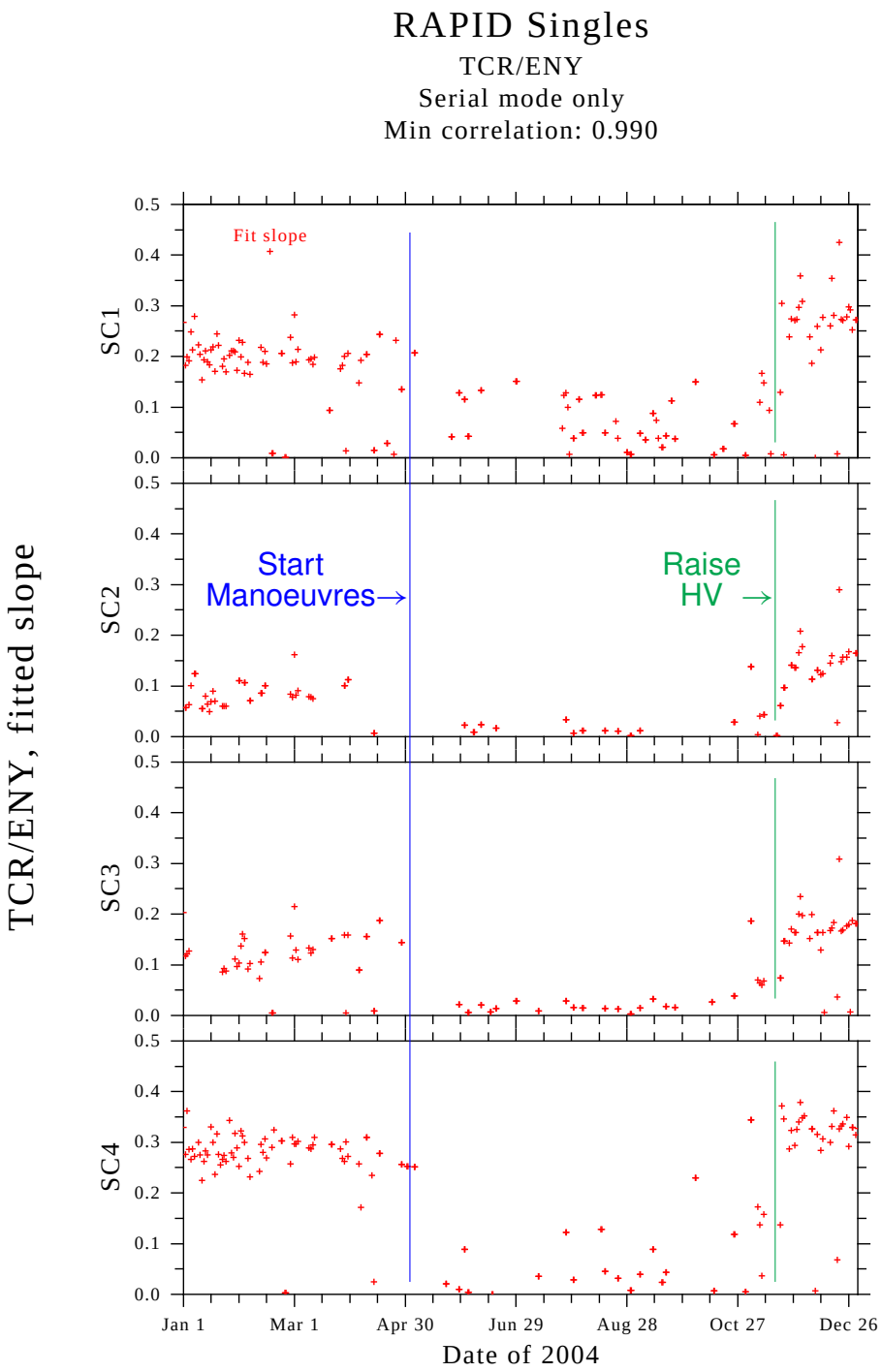

Figure 15: Fitted slopes of "triple coincidences" (TCR) to "Energy Rate" (ENY) signals for all 4 spacecraft for the year 2004. This slope is a good estimate for the time-of-flight efficiency. Each point is the best fit over 1 hour for each day. Only points with correlation factor >99% are included.

5.3 Features of IIMS Series 4

An overview of the behaviour of the ion detectors over the mission lifetime is given in Figure 16, which shows the raw count rates as monthly averages. (Data from the radiation belts have been excluded.) The red lines at the top of each panel indicate manouevres, which are expected to cause deterioration of the detectors, while the vertical dashed lines are times when the voltages on the MCPs were increased, leading to improved efficiency.

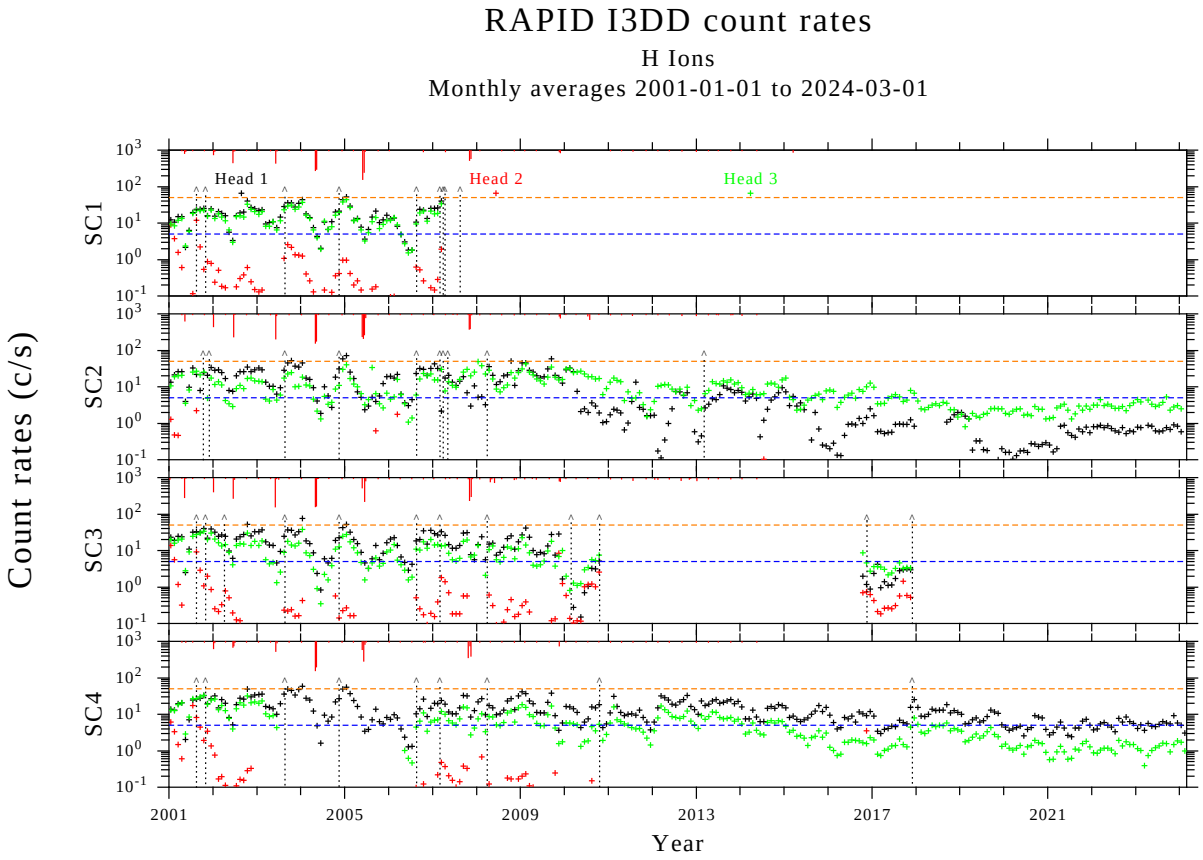

Figure 16: Hydrogen count rates over the mission lifetime. Each point is a monthly average of the rates in each of the 3 detector heads, above 7 R_E. The dotted lines indicate times when the high voltages on the MCPs were changed (usually increased) and the red lines at the top of each panel show when major manoeuvres occurred, the length and width being proportional to the durations. The horizontal dashed lines mark certain count rates for comparison between the panels.
Note the rapid loss of the count rates in head 2 (red crosses), the donut effect.

This figure shows clearly when the ions on SC1 and SC3 failed. (On SC3, data were still collected after the failure, and again during 2017, to see if a recovery were possible, but since the voltages proved to be unstable and the detectors noisy, it was decided not to process these test data.)

Note also the strange mode that SC4 entered on June 21, 2003, when only head 1 was functioning. This lasted until May 09, 2006 when a spontaneous reboot reset the DPU completely. This interval requires special treatment for handling the TOF efficiency, something that was added only at the 4th release.

One also sees in this figure how the remaining two detector heads on SC2 and SC4 start to give quite different results. This is most serious on SC2 where head 1 becomes an order of magnitude less sensitive in 2010, then recovers, then goes bad once more; finally at the start of 2018, it seems to stop functioning completely. On SC4,

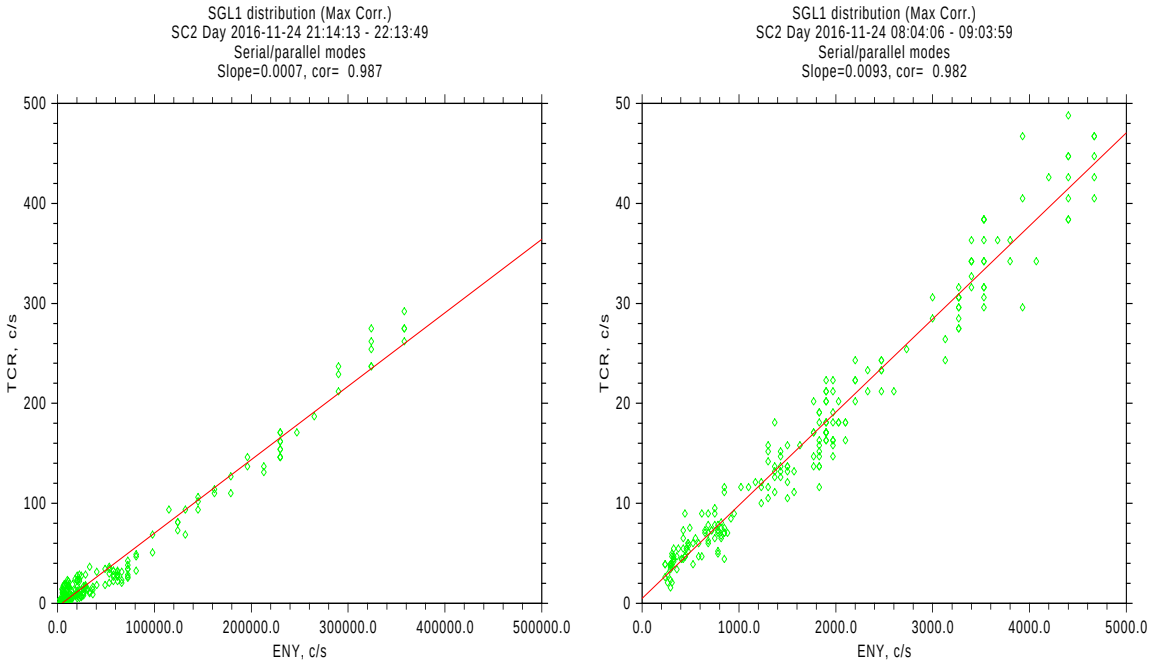

Figure 17: Demonstration of how completely different TOF efficiencies can be determined on the same day and spacecraft. The fit on the left for SC2 was taken at an altitude of 6 R_E, at the edge of the radiation belts, whereas the one on the right a few hours earlier at 12 R_E; its correlation is only slighly less than that on the left, but the slope is more than 10 times higher.

it is head 3 that loses sensitivity, becoming more serious mid 2015.

During the development of the series 3 calibrations (3rd release), it became clear that in the years when the remaining heads had quite different sensitivities, the TOF efficiencies on SC2 appeared to be very much underestimated, something that then produced considerably higher fluxes on SC2 compared to SC4. This was extremely suspicious since the count rates on the two spacecraft were similar and therefore we would expect the TOF efficiencies also to be similar.

It turned out that at these times the maximum correlations for the TOF efficiency, as described above in Section 5.2.3, was often found at the outer edge of the radiation belts, with very high count rates. As shown in Figure 17, the efficiency found here can be much less than that taken a further out at lower count rates. The reason for this could be that electrons from the radiation belts are triggering the energy detectors but not the time-of-flight signal, thus producing an apparently low efficiency for the ions.

For the series 4 (4th release) it was decided to restrict the TOF efficiency determinations to beyond 10 R_E, to make them more reliable. These values also correspond more to what one would expect from the relative count rates between SC2 and SC4. The disadvantage is that at these distances there are fewer times when good correlations can be found in the later years, a result of the overall lower efficiencies since the first years of the mission.

It should be pointed out that the method really only determines the efficiency *averaged over all three heads*, including the non-functioning central one. This average is then split up over the individual heads by means of the *directional distribution* parameters of Section 3.3.

The use of these directional distribution parameters is another change in the 4th release. They determine the differences between the detector heads and their sub-directions in a manner more reliable than what was used in previous releases.

The resulting series 4 conversion factors for hydrogen channel 1 are shown in Figure 18 for the mission lifetime,

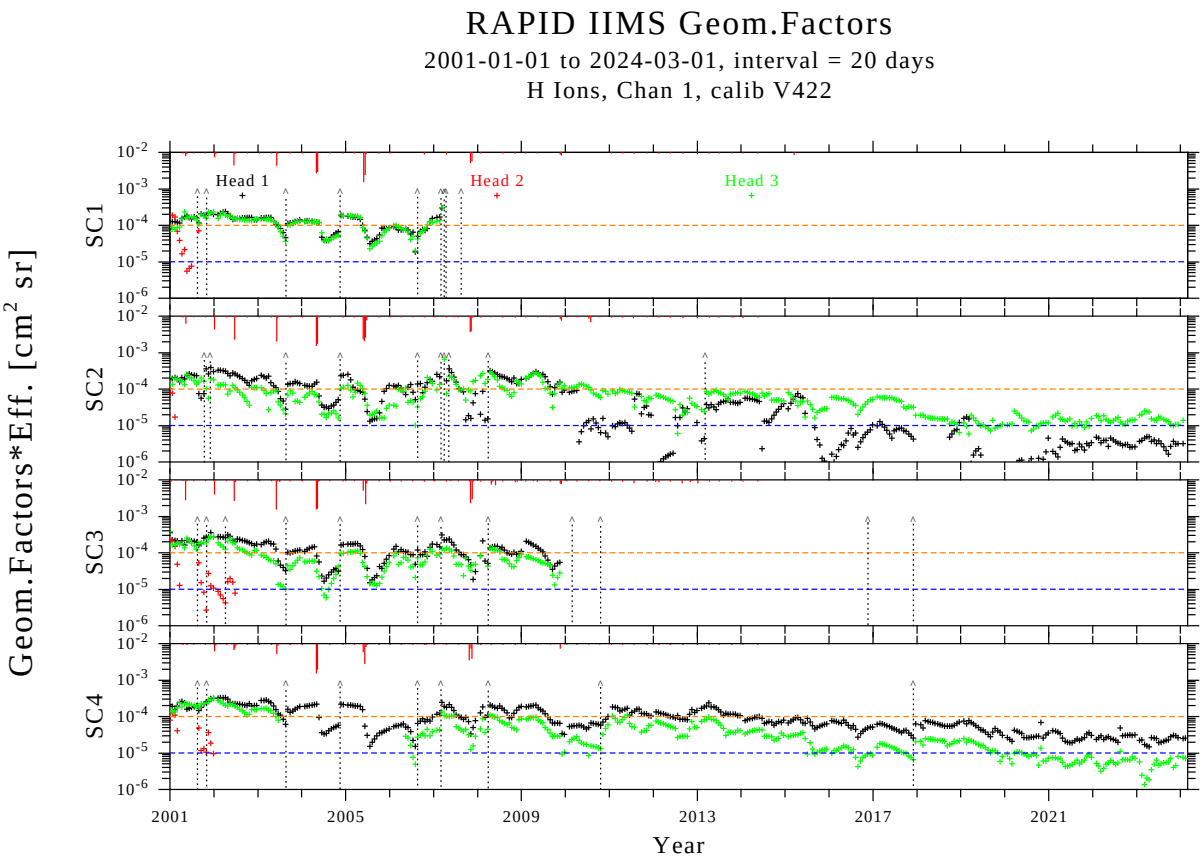

Figure 18: The conversion factors (geometry factor times efficiencies) for hydrogen, channel 1, over the mission lifetime, for each detector head and spacecraft, at intervals of 15 days. As for Figure 16, the dotted lines indicate times when the high voltages on the MCPs were changed (usually increased) and the red lines at the top of each panel show when major manoeuvres occurred, the length and width being proportional to the durations. The horizontal dashed lines mark certain values for comparison between the panels.

demonstrating the deteriorations during manoeuvres, the recoveries when the high voltages are increased, and the large differences in sensitivities between heads 1 and 3 in the later years.

Figures 19–21 show the resulting series 4 fluxes for the 3 ion species H, He, CNO. Note that the differences between the remaining heads in the later years have been compensated for by the difference conversion factors so that the average fluxes in both heads are equal. Of course, the error bars in the less-sensitive head will be much higher since these fluxes are derived from lower count rates.

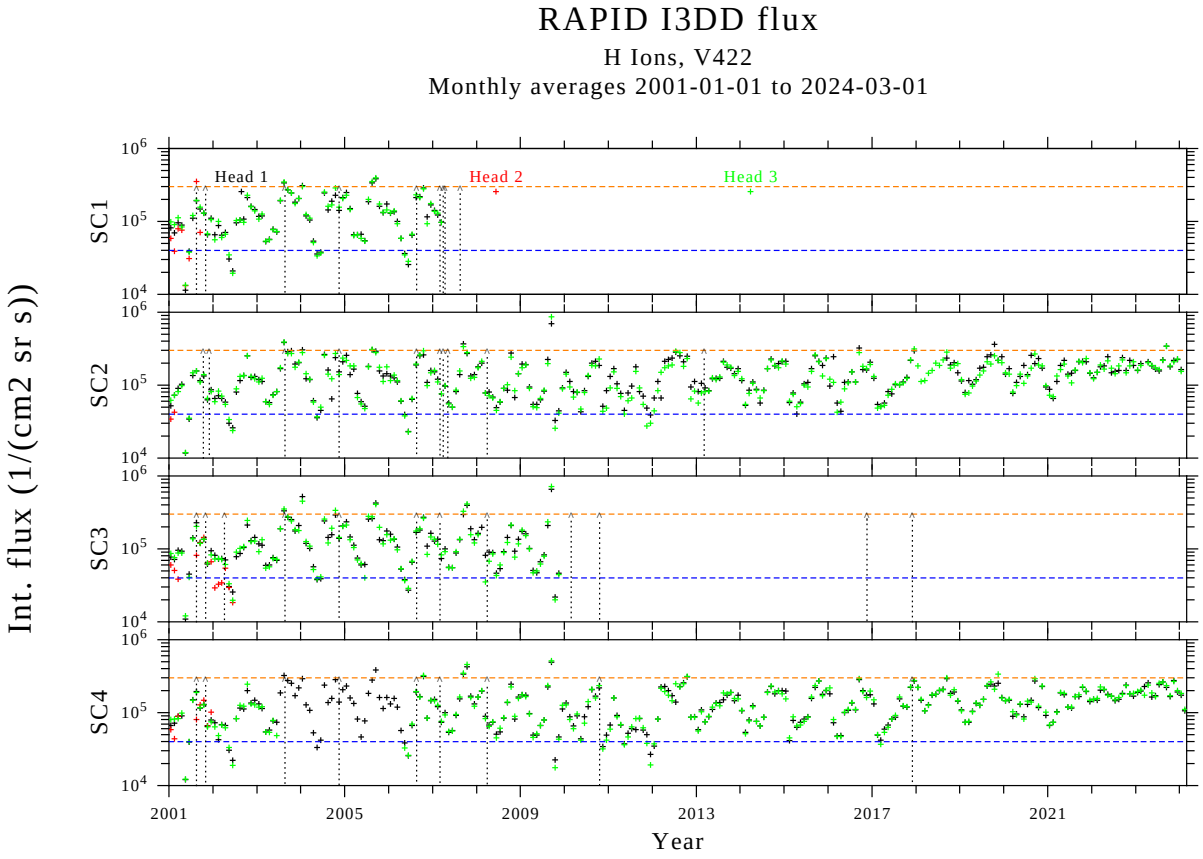

Figure 19: Hydrogen fluxes from series 4 calibration, in the same format as in Figure 16, i.e. monthly averages above 7 R_E.

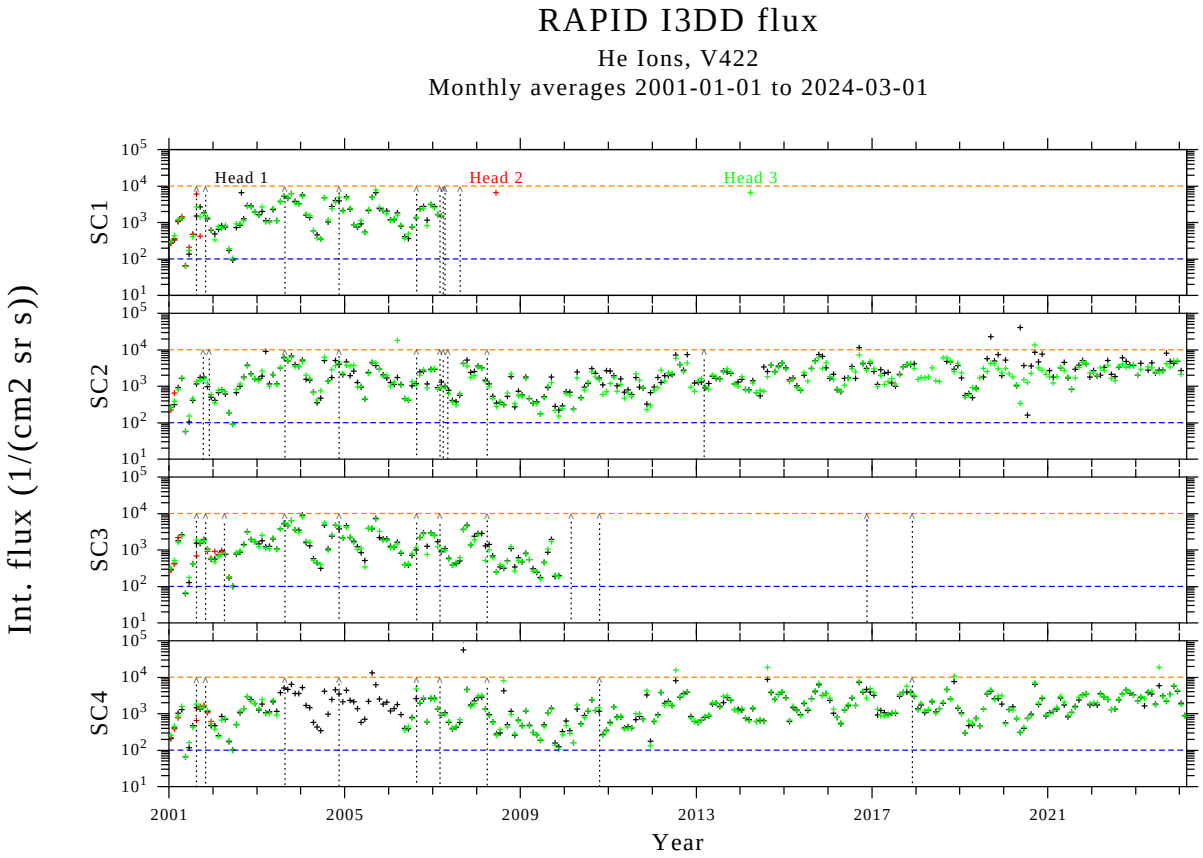

Figure 20: Helium fluxes from series 4 calibration, as in Figure 19.

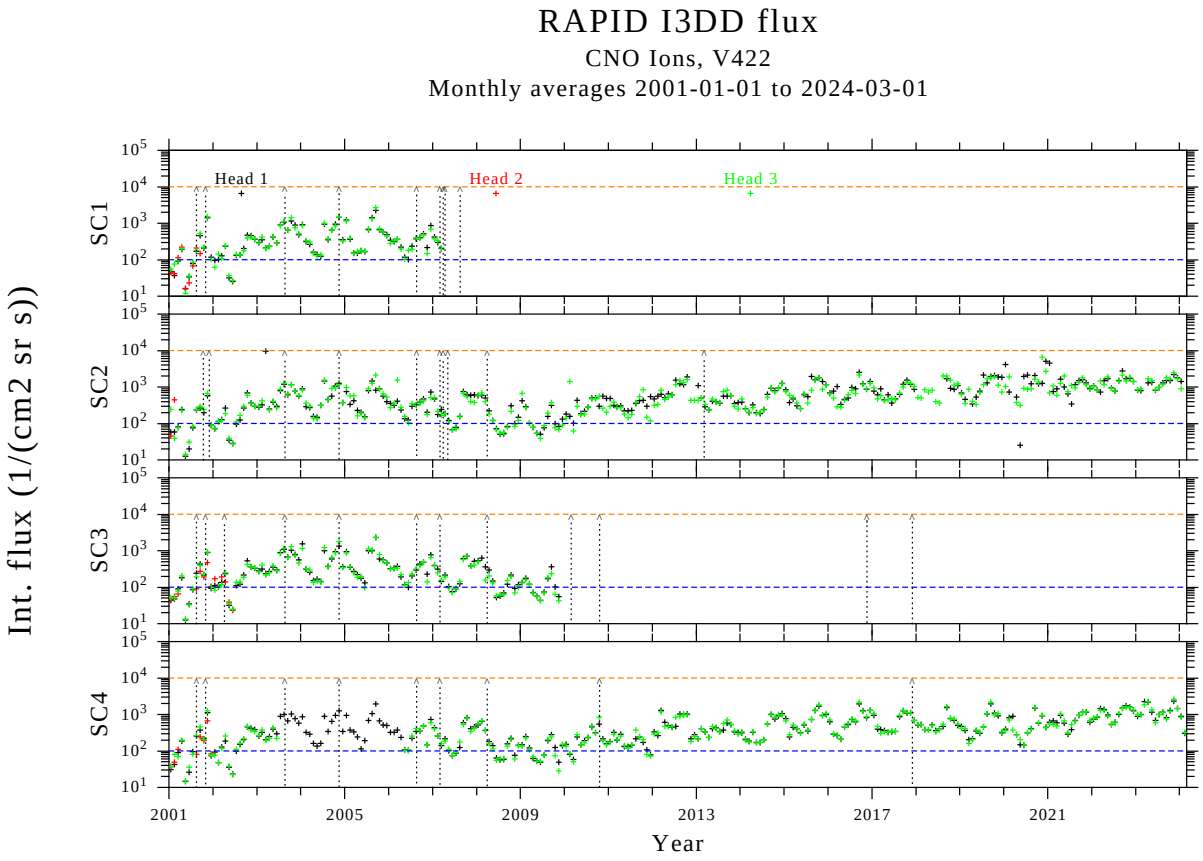

Figure 21: CNO fluxes from series 4 calibration, as in Figure 19

.

6 Results of Cross-Calibration Activities

The performance of the different particle instruments (RAPID, CIS, PEACE) can be monitored by intercalibration between them. It is important to check if the joint spectra are continuous.

6.1 RAPID/IIMS and CIS/CODIF Cross-Calibration

*This Section has been completely updated by **E. Kronberg** in Issue 7.1, December 2021.*

To evaluate the joint RAPID/IIMS and CIS/CODIF spectra we used the omnidirectional proton intensities from C4 for the time period from 2001 to 2018 with the best available calibrations in 2020. SC4 is the only spacecraft which allows joint spectra of these two instruments on a long-time scale. We have selected data only in the magnetosphere, namely when `CIS_MODE` was equal to 13 and resample the data to 1 min average, to have them at the same time tag. Additionally, we have selected only those spectra when all available CIS channels had values larger than 0. The same condition was required for the first RAPID channel. By this we got 892 325 samples of 1 min data. To calculate the ratio between the proton intensities measured by the two instruments we used the highest CIS channel at the energies 30.2–38.4 keV and the lowest RAPID channel at the energies 27.7–64.4 keV with the effective energies, calculated as geometric mean, of 34 keV/42 keV, respectively. To compensate for the difference in effective energies of 8 keV, we extrapolated the CIS proton intensities, f, to 42 keV using the following formula:

$$f_{42\ \mathrm{keV}} = \exp\left[f_{34\ \mathrm{keV}} - \gamma(42\ \mathrm{keV}/34\ \mathrm{keV})\right]$$

where $\gamma = \log(f_{29\ \mathrm{keV}}/f_{34\ \mathrm{keV}})/\log(34\ \mathrm{keV}/29\ \mathrm{keV})$ and 29 keV is the effective energy of the second last CIS energy channel. In Figure 22 one can see the ratios between the proton intensities measured by the CIS and the RAPID instruments averaged to 1 month for 18 years of observations. The median ratio between CIS and RAPID intensities is 0.78. This is very good considering that the proton intensities were measured by the different instruments and the measurements undergo thorough calibrations.

In Figure 23 we present the distribution of the number of samples for the CIS/RAPID proton intensity ratios. The distribution is relatively symmetric around the median value and 91% of the ratio values are within the 0.1–10 range.

The joint spectra between the proton intensities measured by the CIS and the RAPID instrument for 18 years are shown in Figure 24. The joint spectra shows almost perfect match.

The cross-calibration of IIMS CNO/He with CODIF O^+/He^+ intensities cannot be made reliably as two appropriate adjacent energy channels have large separations between each other. The spectra comparisons for IIMS CNO with CODIF O^+ are presented in Section 6.2, Figure 26.

6.2 1st CNO energy channel

While doing investigations on the bow shock, a strange behaviour of the 1st CNO energy channel was discovered, as CNO bursts, see Figure 25, right column, top panel. Also we were puzzled why the CNO intensity gradients between SC1 and SC3 for the 1st energy channel behave differently from the CNO intensity gradients at the higher energies as well the proton and helium intensity gradients. As they show gradients on the earlier stage, see Figure 25. First some physical explanation was sought.

Then we decided that this could be an instrumental effect. The most obvious was first to check if count statistics are sufficient. The raw counts for the CNO are high, i.e. about 30 and RAPID spectra are more or less reasonable. Nevertheless, if one look to the joint CIS/CODIF and RAPID/IIMS spectra for this event we can immediately see that the 1st RAPID CNO energy channel has too high intensities, while the further channels would continue the CIS spectra, see Figure 26.

Intensity bursts of CNO (1st channel) at about 12:00 to 13:30 helped to solve the problem. As it was noticed there is a correlation with the low energy ($\sim$ 2–30 keV) protons and helium in the CIS energy range, see energy spectrograms in Figures 27.

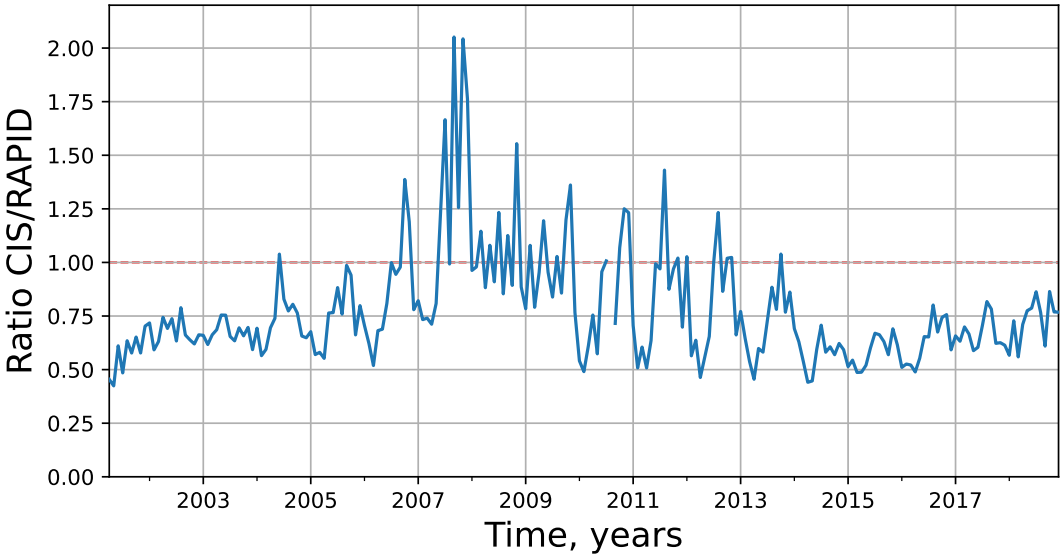

Figure 22: The median ratios between the CIS and RAPID proton intensities averaged to 1 month for 18 years of the Cluster observations.

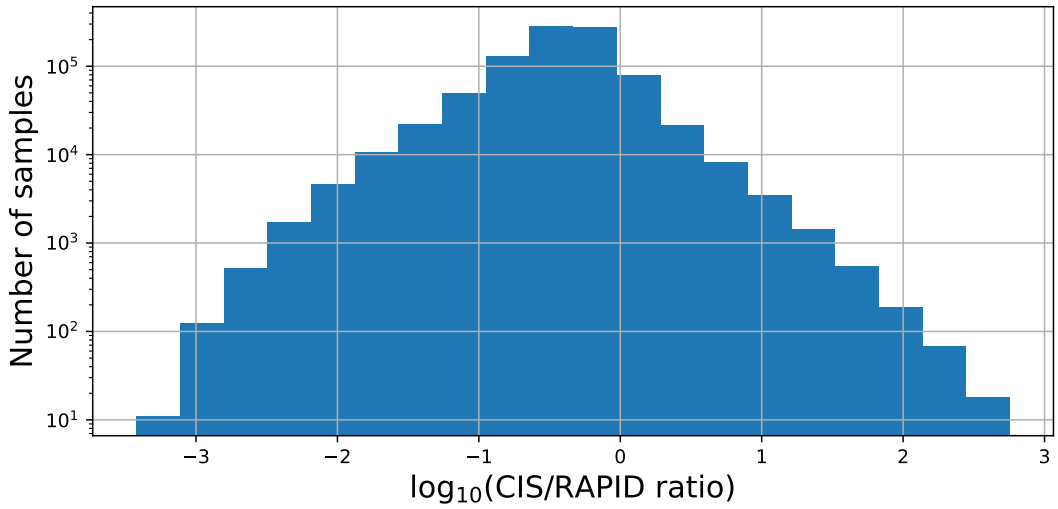

Figure 23: Number of samples of the CIS/RAPID proton intensity median ratios averaged to 1 minute for 18 years of the Cluster observations in the logarithmic scale.

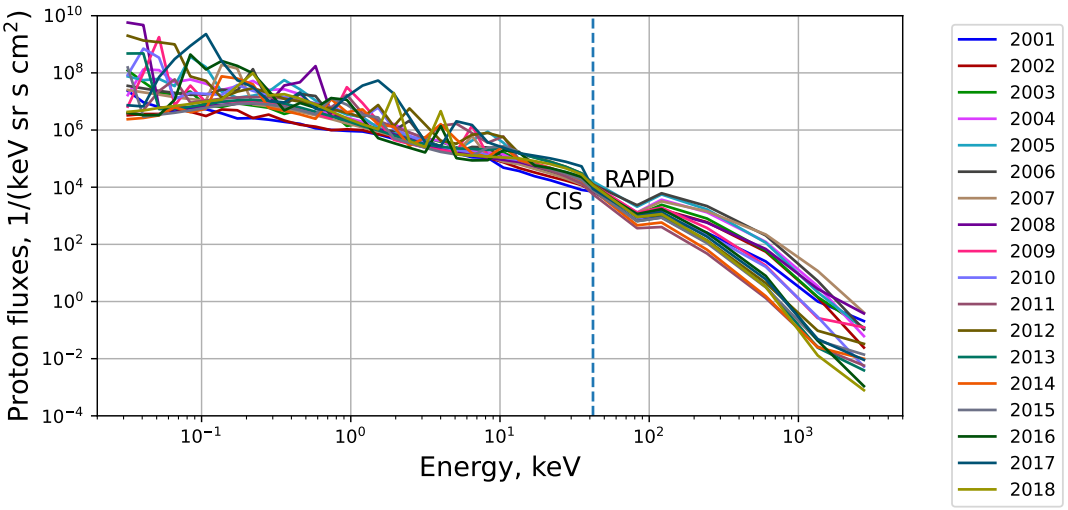

Figure 24: Joint spectra between the average proton intensities measured by the CIS and RAPID instruments for the 18 years of observations. The dashed vertical line is at 42 keV.

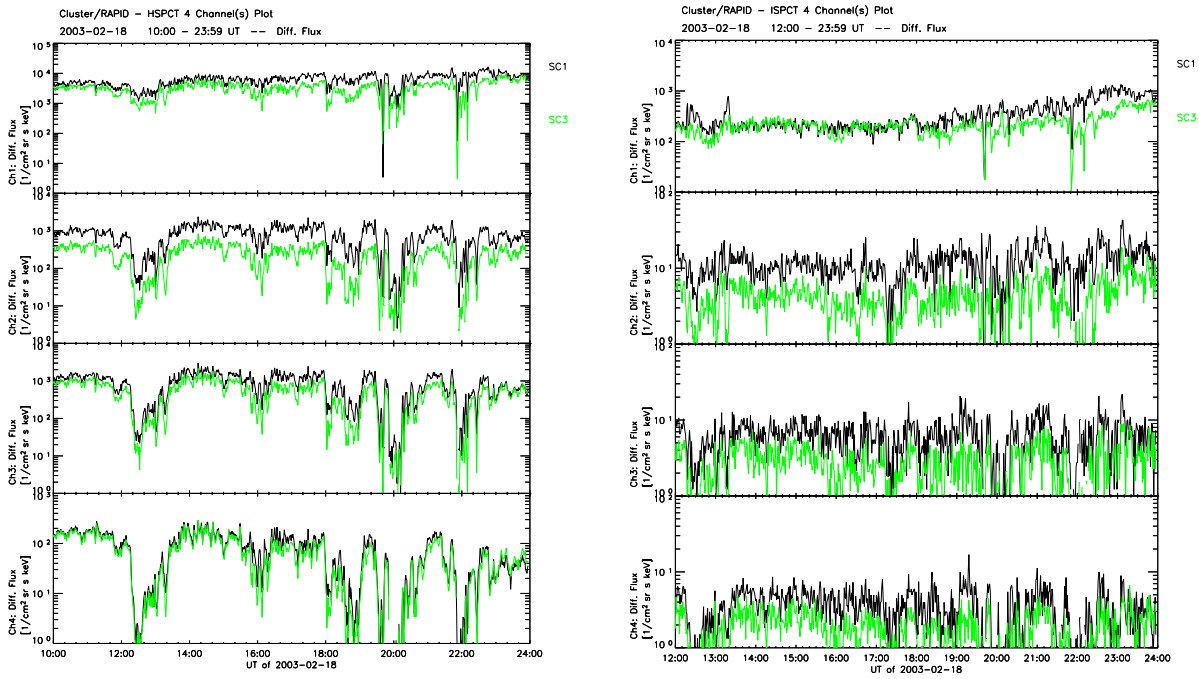

Figure 25: Proton and CNO fluxes for the upstream event in 18 February, 2003, for SC1 and SC3.

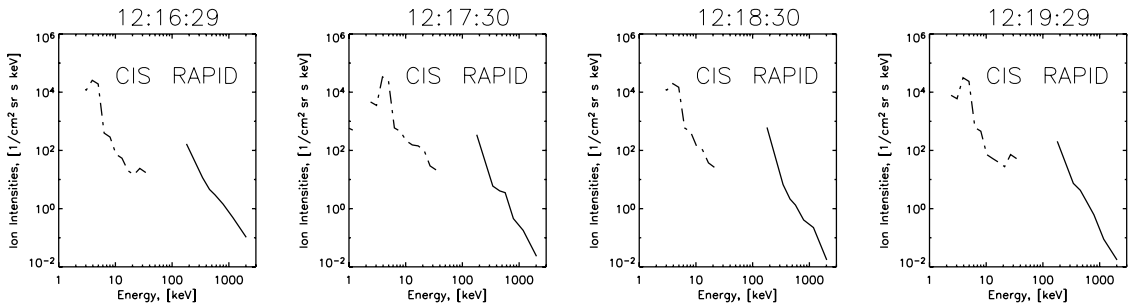

Figure 26: Joint CIS/CODIF O^+ and RAPID/IIMS CNO spectra for the upstream event in 18 February, 2003, for SC1.

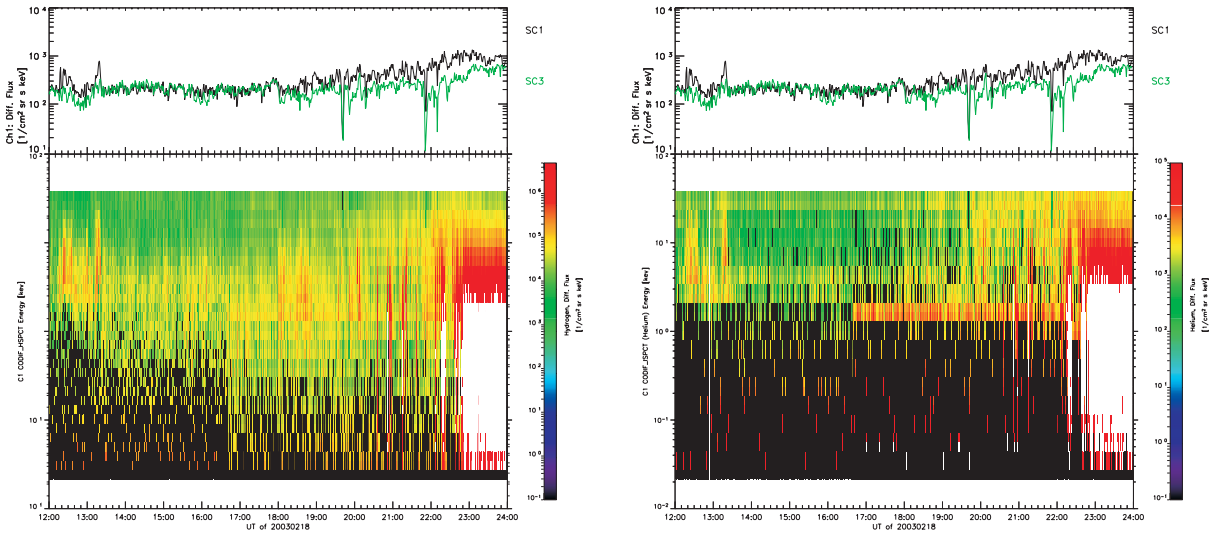

Figure 27: Energy spectrograms for CIS and RAPID proton (left) and helium (right) fluxes, 18 February, 2003.

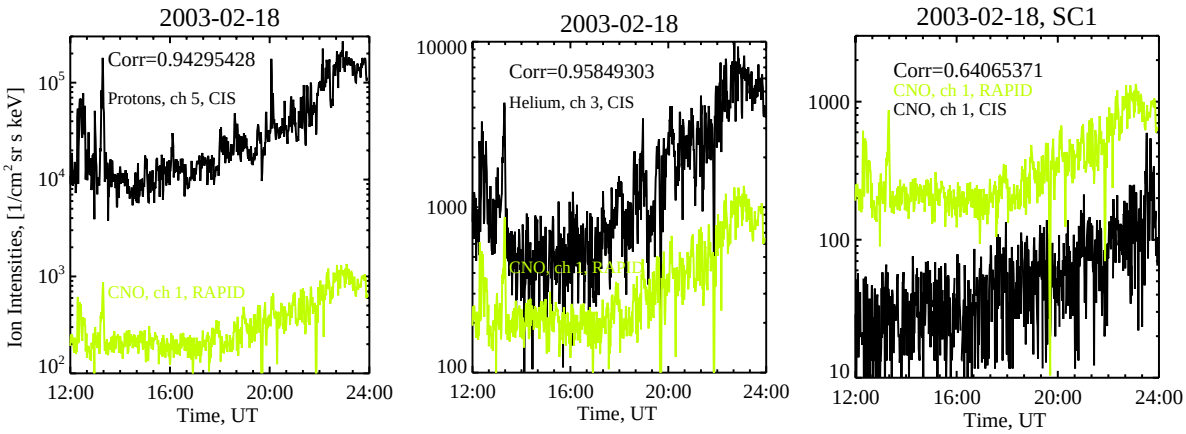

Figure 28: Proton (5th CIS energy channel, 11.5–14.5 keV) and CNO (1st RAPID energy channel, 83.8–274.4) fluxes (left); Helium (3rd CIS energy channel, 18.6–23.7 keV) and CNO (1st RAPID energy channel, 83.8–274.4) fluxes (center); CNO fluxes (1st CIS energy channel, 30.1–38.2 keV) fluxes (right) and CNO (1st RAPID energy channel, 83.8–274.4) fluxes for the upstream event in 18 February, 2003, for SC1.

As for the 1st He energy channel the ion classification is done only on TOF information (see Section 5.2). Therefore the species determination is not very precise. We estimated the energies for protons and helium at which particles could trigger the TOF signal erroneously counted as a CNO. For the protons the predicted energy range is 12–14 keV (or CIS energy channel 5) and for the helium 16–25 keV (or CIS energy channels 2–4). We tested the correlation between the proton and helium intensities at corresponding energies and the intensities of the 1st CNO energy channel. The results with the best correlation are presented in Figure 28. The correlation of the intensities of the 1st CNO energy channel with intensities of the predicted energy channels is surprisingly good, i.e. $\sim$0.94 and $\sim$0.96, for protons and helium correspondingly, and it becomes gradually worse for the adjacent channels. The correlation with the CIS 1st CNO channel is not satisfactory, $\sim$0.64.

Our conclusion is that the first CNO energy channel is contaminated by low energy helium and protons; for this reason, we have removed it by setting it to fill values.

6.3 RAPID/IES and PEACE Comparison: Histogram Mode Analysis

*This Section is based on work by **C. H. Perry** and **A. Åsnes.***

RAPID/IES histogram mode is a special test mode which is run about once per month. It returns a few spins of data from each detector at each integration time. The mode provides full pulse-height determination (256 energy bins) at best energy sampling (2.2 keV). This compares to normal/burst mode data which give 6/8 logarithmically spaced energy channels.

The purpose of this analysis is to examine the lower energy threshold of RAPID and try to reduce the energy gap between highest PEACE and lowest RAPID flux measurement.

For the cross-calibration PEACE CP_PEA_3DXPH dataset was used. This provides full 3-D distribution with 6 polar directions. For the data comparison the nearest PEACE sample to histogram-mode spin was selected. Then the PEACE polar zone closest to each of the 9 RAPID detectors was chosen and PEACE azimuths were integrated to produce spin averaged products.

Figure 29 shows the overlaid PEACE and RAPID spectra for two detectors. Inspecting the RAPID histogram mode data (bottom panels), the falloff in efficiency of the RAPID detectors towards lower energy is apparent. There is also evidence for this in the lowest science energy channel of the IES when compared with the extrapolated PEACE data.

Additionally several intervals of hot magnetotail plasma sheet were investigated for the cross-calibration using kappa-fit, see Figure 30.

The kappa-fits were performed (using PEACE SPINPAD, RAPID IES ESPCT products) using the energy range from 3–400 keV, but excluding the lower RAPID channel and the top PEACE channel.

Visual inspection of several magnetotail plasma sheet intervals show that the kappa fits join PEACE and RAPID IES data nicely most of the time, as long as the distribution assumes a kappa-function shape.

Note: in all these Figures there is a deviation of the RAPID data at the low energies from the fitted curves. This *energy defect* is treated thoroughly in Section 7 below.

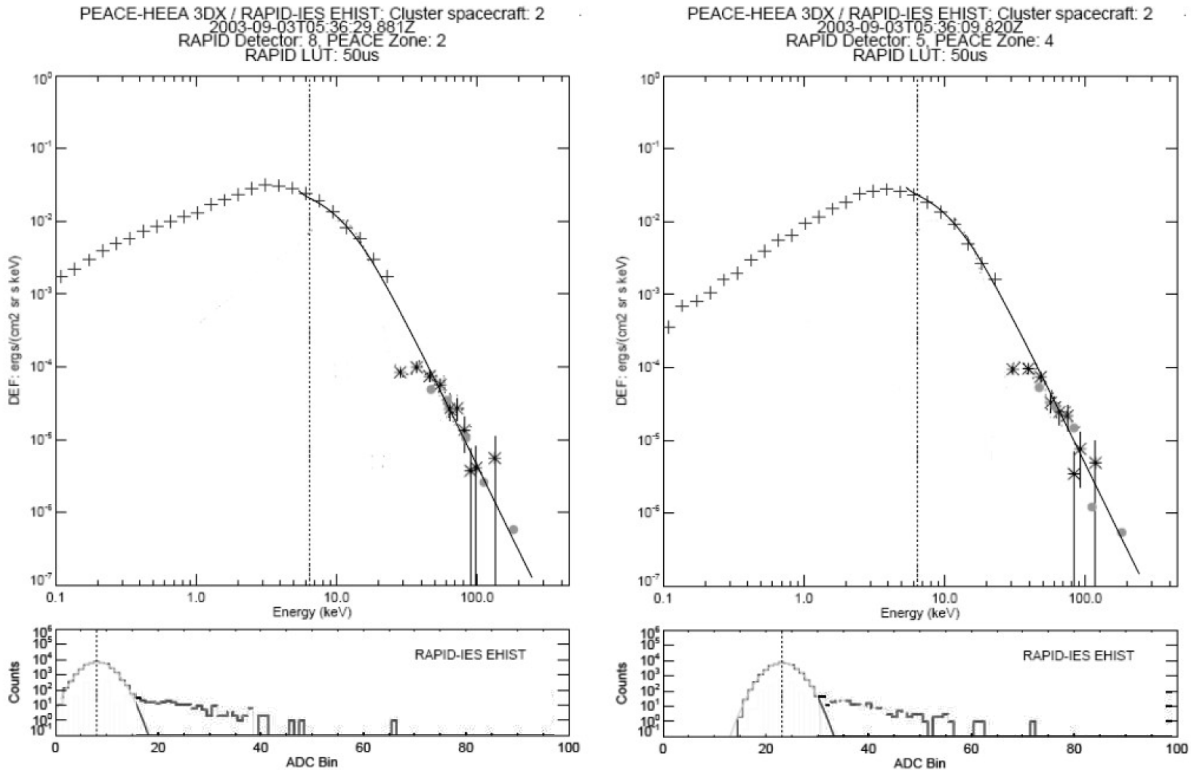

Figure 29: The electron differential energy spectra from the PEACE and RAPID instruments covering the range from 100 ev to several hundred keV. The plots are from two different polar look directions from the Cluster 2 spacecraft. The upper panels show PEACE 3DX data (+) together with RAPID/IES E3DD (•) and background subtracted, 5 point averaged, RAPID histogram mode data (*). The lower panels show the corresponding uncorrected RAPID histogram mode data including the Gaussian fit to the background noise distribution (pedestal).

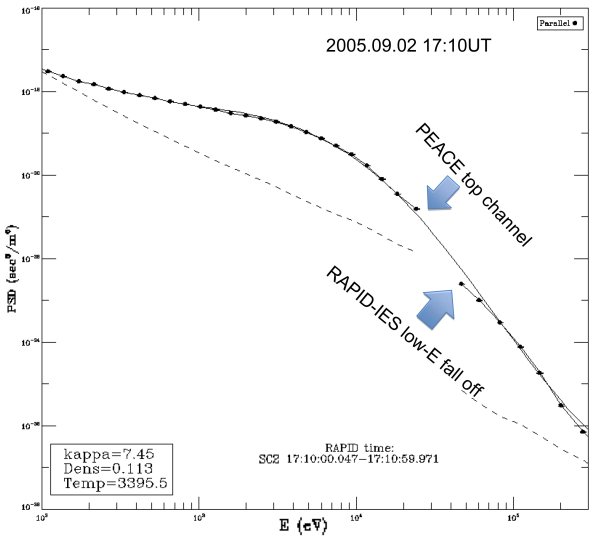

Figure 30: Kappa-fit on joint 1-minute averaged PEACE and RAPID IES spectrum. One-count levels of the instruments are shown as dashed lines.

6.4 RAPID/IES and PEACE: Electron Spectra Comparison

*This Section has been added by **E. Vilenius** in Issue 10.0, April 2024.*

6.4.1 Input data

In this PEACE/RAPID comparison we have used data from the years 2001–2020. The energy ranges of PEACE and RAPID are different and there is no overlap between the two instruments. When PEACE is operated its energy range is varying and does not cover the entire possible range of 0.6–26 460 eV at any given time. The highest measured energy channel of PEACE, which can be approximately 26 keV or significantly lower, is followed by an energy gap until the RAPID range starts. The lowest energy channel of RAPID has been changing over the mission in the range 37–41 keV but the energy channel definitions of RAPID are constant during operations and changed only occasionally by updating on-board settings. The probability that PEACE operates at its highest energies depends on the telemetry mode. In the Nominal Mode (NM) telemetry PEACE produces electron 3-D distributions only for low energies and rarely for higher energies. Therefore, we concentrate on Burst Mode times only. We also limit this comparison to data above L=7 to avoid using RAPID/IES corrections due to radiation belt effects.

For RAPID spectra we use the ESPCT6 electron omnidirectional flux product, which contains omnidirectional fluxes in 6 energy channels over one spin of the spacecraft, both in Nominal and Burst modes. It also contains the standard deviations for the flux values. In addition to the fluxes we use the product IES_BG which gives the long-term electron background for all the 9 detectors in 6 energy channels accumulated over one hour. In IES_BG, if the variance over one hour is from a Poisson distribution of constant mean then this mean value is assigned as the background value, otherwise a fill value is given in the product for that hour (see Section 11).

The PEACE instrument has two sensors: LEEA (Low-Energy Electron Analyser) and HEEA (High-Energy Electron Analyser). Both are capable of measurements at high energies but HEEA was usually used to measure them. HEEA has a greater geometric factor than LEEA and is suitable for low-density regions of the magnetosphere. From PEACE/HEEA we use the enhanced resolution 3DXPH product when available and otherwise the standard resolution electron 3-D distribution 3DRH. The numbers of energy channels in these products are either 13, 15 or 30. These PEACE products contain also the background flux levels but there are no uncertainties given for the fluxes. We determine these errorbars from the directional PEACE data when calculating the omnidirectional averages.

To avoid effects of temporal changes in the spectrum during the averaging we use time blocks of 30 s. In this time the spacecraft typically move 17–160 km depending on their true anomaly angles along their orbits. Our tests with spectra averaged over 60 s (as used in some earlier comparisons) indicate that there are cases when one instrument has a few records at the beginning of a minute and the other instrument at the end of the same minute such that the assumption of a constant spectrum may not be valid.

We make quality checks on the data points before they are accepted to be used in further analysis. For these checks we consider the quality flags given in the data files, the PEACE energy range accepting only cases where PEACE has measured up to at least 13 keV, and the flux level of data points. We require that the measured flux is at least 3σ above the background level. Examples of spectra are shown in Figure 31.

6.4.2 Analysis

We model the combined PEACE+RAPID spectrum by a κ function and the RAPID-only spectrum by an exponential, which in log-log plots is a straight line. Since there are occasionally spectra which do not follow a κ function we have an automatic algorithm to remove such cases. The form of the κ function in terms of the energy E is

$$f(E) = \frac{Nc}{\pi\sqrt{2\pi m_e}} \frac{\frac{E}{\kappa W}}{\sqrt{\kappa W}\left(1+\frac{E}{\kappa W}\right)^{\kappa+1}} \frac{\Gamma(\kappa+1)}{\Gamma\left(\kappa-\frac{1}{2}\right)}, \quad (1)$$

where the fit parameters are the number density of electrons N, the energy at maximum flux W and the κ parameter. The other symbols are c for speed of light, m_e for electron mass and Γ for the gamma function. Two

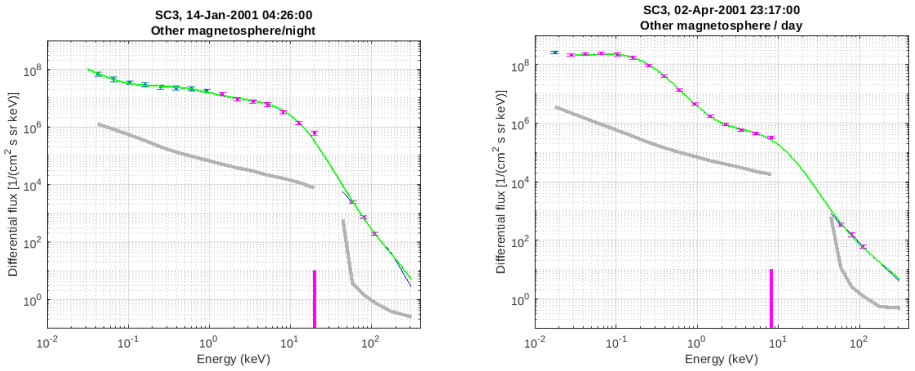

Figure 31: Examples of observed PEACE and RAPID spectra from spacecraft 3. The gray thick curve is the background level for both instruments with the energy gap shown as a discontinuity. It can be noted that the maximum PEACE energy channel (indicated by a vertical magenta bar) is different in the two cases. In the PEACE spectra the magenta data points have been accepted after all the quality checks listed in this section whereas the blue data points did not pass all the checks. From RAPID we take energy channels 2–4 as the first channel is known to have an energy defect. The blue thin curve goes through all the six RAPID points. The green thin curve is a smooth curve guided by all the data points but not necessarily going through them.

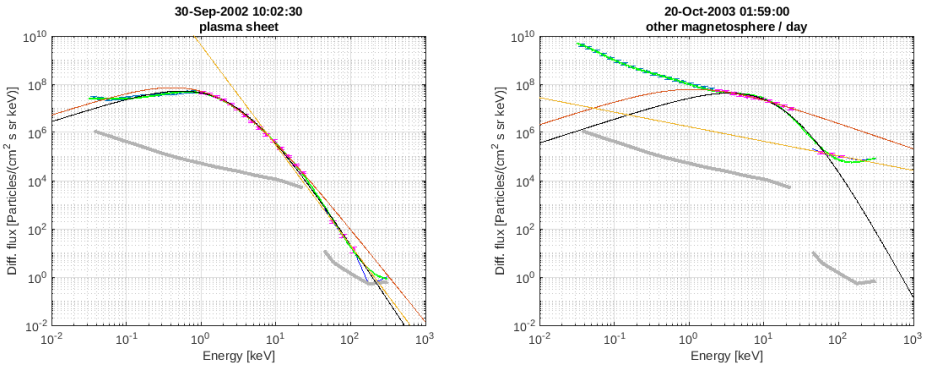

Figure 32: Examples of fitted κ spectra and power laws (RAPID-only) from spacecraft 2. The black curve is the PEACE+RAPID κ fit, the red curve is a PEACE-only κ fit, and the yellow straight line is the RAPID-only power law fit.

limiting cases can be noted: at high energies this function approaches a power law and as κ approaches infinity the resulting function gives the Maxwellian distribution.

Examples of fits are shown in Figure 32. While this figure shows two cases, a good compatibility between PEACE and RAPID as well as a poor compatibility, it is useful to analyse larger amounts of spectra. Such examples are shown in Figure 33. The combined PEACE+RAPID fits are almost always steeper than RAPID-only power law fits and the histogram shows an offset of 1–2.

6.4.3 Conclusions

Based on statistical analysis of several thousand spectra we conclude that there is a difference between PEACE+RAPID fitted spectrum vs RAPID-only power law parameter: the combined fit κ spectrum is systematically steeper by 1–2 (in κ). Furthermore, RAPID-only power law fits have a range which is limited such that large values of γ are missing whereas κ is much more distributed. This is especially apparent when the "electron temperature" ($kT_e = W\,\kappa/(\kappa - 1.5)$) is high. The compatibility has a weak dependence on the region of geospace: there is better agreement between the spectra in tail lobe.

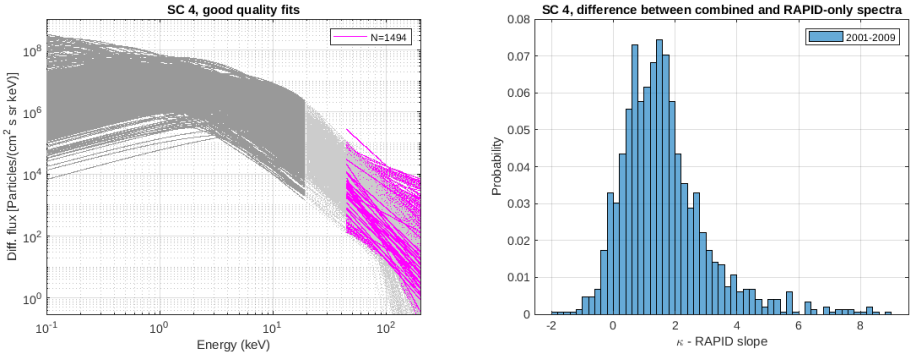

Figure 33: Examples of fitted κ spectra and power laws (RAPID-only) from spacecraft 2. On the left side only the fitted curves are plotted without any data points. The gray curves are the κ fits such that the darker gray indicates the (maximum) PEACE energy range and the light gray is extrapolated to higher energies. The magenta lines are the RAPID-only power law fits. The histogram shows the distribution of κ-γ where γ are the RAPID-only power law slopes.

7 The IES Energy Defect

7.1 RAPID/IES Calibration: Statistical Study

As a side-effect of the histogram studies in Section 6.3, it appears that there is a problem with the IES calibration at the lowest energies (Figures 29 and 30). Calibration studies from before launch suggest that the energy losses in the detector dead layer could be energy dependent and greater than the assumed 6.5 keV at the lower energies.

To investigate this systematically, a spectral analysis program was developed, as shown in Figure 34. Following the method outlined in Section B.1, a power law $j(E) = A \cdot E^{-\gamma}$ is fitted to energy channels 2 and 3, and then extrapolated back to channel 1. To be more precise, the power law is found such that its integral over channels 2 and 3 yield the measured integral flux in these channels, and it is then integrated over channel 1 as well. The ratio of this extrapolated flux to the measured flux in channel 1 is then the indicator of the mismatch.

A database of 1-minute averages of the E2DD6 data (spin averages for each of 9 detectors) was created for the months of March and September for every year from 2001 to 2012. These two months were selected to ensure that both solar wind and tail regions are included. Further selection criteria for the database are:

- distance from the Earth $> 6\,R_E$, to avoid the radiation belts,
- flux in energy channel 3 > 10 (cm^2 sr s keV)$^{-1}$, to ensure sufficient statistics

For the analysis itself, we apply the additional conditions:

- the spectral index γ lies between 3.0 and 6.0 (for a flat spectrum the mismatch would disappear even the effect were there)
- the γ for channels 2 and 3 differs no more than 0.2 from that for channels 3 and 4, i.e., we have good power law spectrum over all 3 channels and can assume that it can be extended to energy channel 1 as well.

Figure 36 shows the results for spacecraft 1 for 2 months, one early in the Mission, and one more recently. The mismatch is very clear, in all detectors. The other spacecraft exhibit similar mismatches.

It might appear that the effect was greater in the earlier plot, but this is due to the fact that then the actual channel 1 threshold was set much lower than 37.3 keV, in a region where the discrepancy is expected to be greater.

A similar analysis on channel 2, by fitting channels 3 and 4 and extrapolating back produces no significant systematic mismatch. Thus the effect applies only below 50 keV, something that is also confirmed by the analysis in

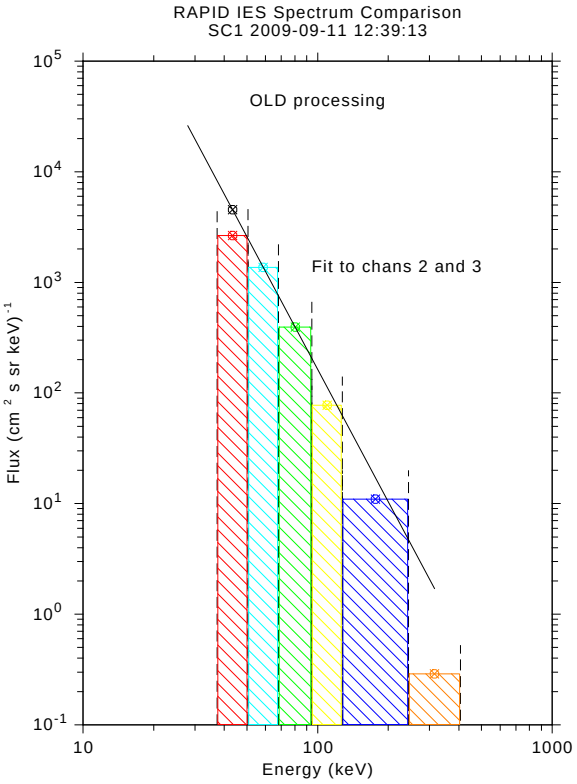

Figure 34: Example of the spectral analysis: a power law is fitted to channels 2 and 3, and then extrapolated back to the energy of channel 1 and compared to the measured flux.

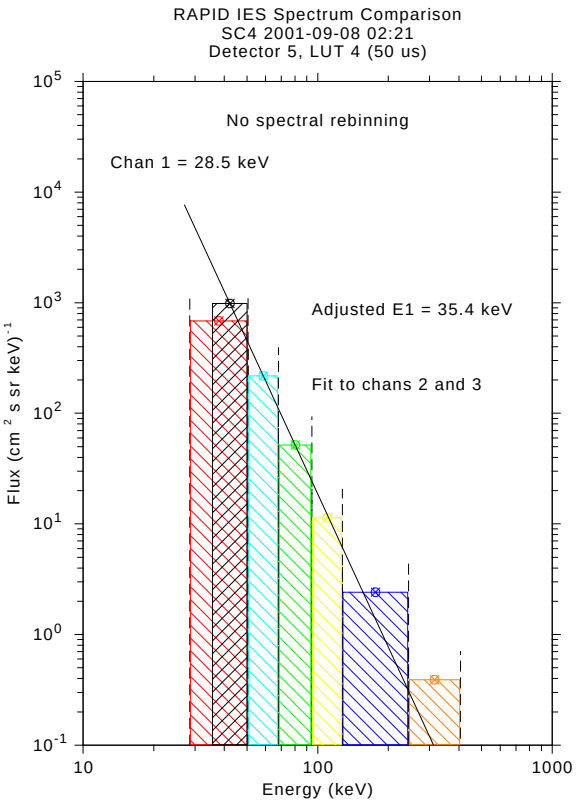

Figure 35: Determination of energy defect from spectral analysis: a new threshold for energy channel 1 is found such that the integral of the fitted power law (black region) equals the measured integral flux in channel 1 (red region).

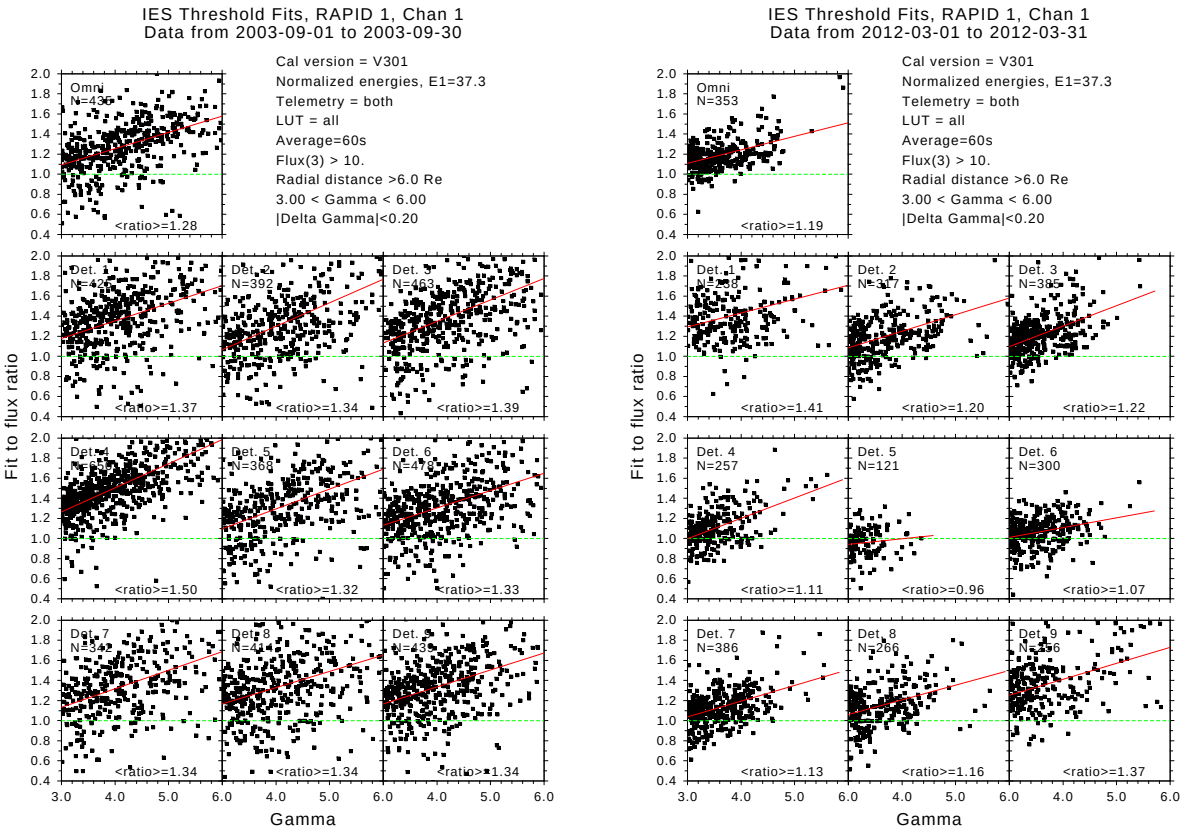

Figure 36: The ratios between the extrapolated power law and the measured flux in energy channel 1 in each of the detectors on SC1, for two widely separated time periods, plotted against spectral index γ. Each point represents a 1-min accumulation meeting all the conditions described in the text. The data were produced with calibration V301, without any energy defects. The mean value of the ratios is given at the bottom of each panel.

the next section.

We therefore see that there is a systematic discrepancy between the electron fluxes in the first energy channel and the fluxes expected from a power law extrapolation of the rest of the spectrum. This could be due to energy-dependent efficiency at lower energies, or to increased dead layer losses (energy defect) at low energies. The latter is not only expected, it is also confirmed by the fact that the mismatches seen in Figure 36 increase with γ. A mismatch due to efficiency fall-off should be independent of the spectral slope.

We conclude that we have an energy defect problem, which we now wish to compensate for or, even better, to correct.

7.2 Corrections for the Energy Defect

To date we have had 3 "solutions" to this problem.

1. When the initial spectral analysis was carried out in 2010, it was found that the spectra could be "fixed" by assuming the first channel had a threshold of 40.7 keV, without reprocessing any of the existing data at CSA. The metadata at CSA were correspondingly altered, in anticipation that once a true energy defect was determined, the data would be reprocessed and the metadata once more adjusted.

   This clearly was only a temporary measure and an unsatisfactory one at that.

2. By 2012, values for the energy defect at different energies had been determined. A new calibration version V311 was produced. The energy for channel 1 was now set at 41.2 keV, the original 37.3 keV plus the new energy defect at that energy.

   The CSA electron data for 2011 were produced with this calibration version.

3. The spectral analysis of Section 7.1 was repeated with the new calibration. However, it became obvious that this was in fact an overcompensation. The extrapolated fluxes were now lower than the measured ones.

   These energy defects had been determined using histogram data, which are taken for only a few minutes each month. Hence they have either poor statistics, or they are taken inside the radiation belts, a region deliberately avoided in the other studies.

   The search started for a better determination, which is described below. It produces a corrected value for the first channel of 39.2 keV. New calibration version V330 is now employed. All the IES data at CSA, including metadata, have been reproduced using this value.

7.3 Latest Determination of the IES Energy Defect

To carry out the new determination of the energy defect, we once again make a new database, with the same criteria as before, for March and September, 2001–2012, but this time using data that have not been rebinned to the standard set of energies (Section 5.1.2). Especially in the time before August 2006, we have "raw" energies going down to as low as 20 keV, which allows us to investigate the energy defect at a wide range of energies. And the distortion from the rebinning is not present, making the results much easier to interpret.

The pedestal shift is still taken into account. This shifts the thresholds of all the energy channels. Pedestal shifts are always present, and are even stronger with higher count rates. This shifting does have the advantage for this study of producing additional energies for the defect determination. It is not limited to a set of fixed values.

Figure 35 illustrates the method used. Once again, a power law is fitted to energy channels 2 and 3, but now the energy is found for which the integral from that new energy equals the measured integral flux in channel 1.

The same conditions are applied as for the spectral analysis ($3.0 < \gamma < 6.0$, $|\Delta\gamma| < 0.2|$), but with the additional condition that the pedestal shift be within ± 5 keV (about 2 bins), since large shifts are subject to error and also indicate extreme situations.

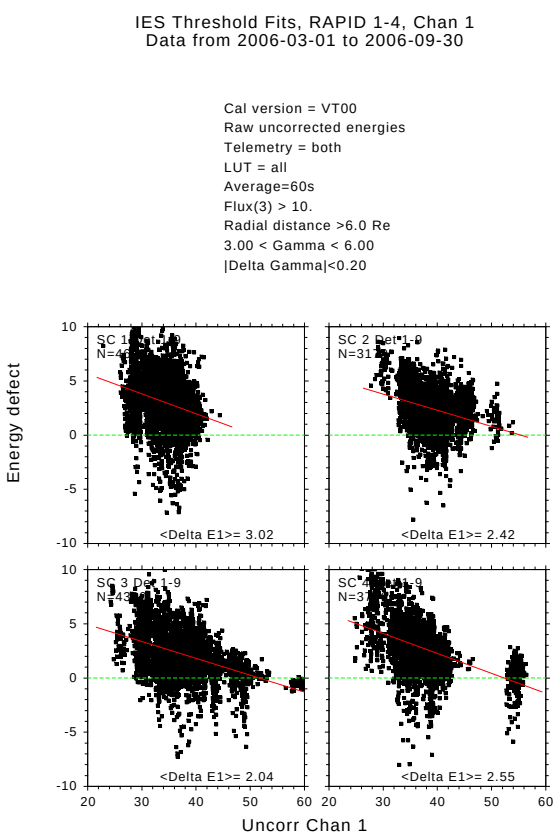

Figure 37: The energy defect on the 4 spacecraft calculated for March and September 2006, plotted against original energy. The red lines are a linear fit to the data.

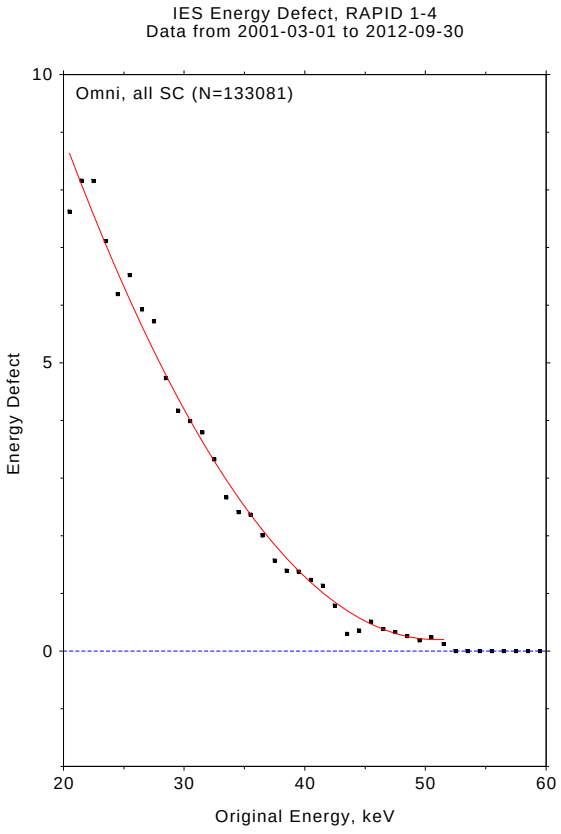

Figure 38: Energy defect plotted against original energy, for all spacecraft, all detectors, all modes, over 12 years from 2001 to 2012. The red curve is a quadratic fit to the defect values below 52 keV.

Figure 37 shows the results for the 4 spacecraft (all detectors together) for March and September, 2006. This period is chosen because it spans the change in the channel definitions from August, 2006, and so has a wider range of original energies than other time periods. Each 1-min interval meeting all the conditions is plotted as a dot, which then produces the black cloud of points. There is considerable spread in the energy defects, but the trend is clear and conforms to what was expected.

In order to view the results more clearly, they are sorted into 1-keV bins by original energy and the average defect in each bin is found. Figure 38 shows these averages for the period from 2001 to 2012, with all spacecraft and detectors combined. The red curve is a quadratic equation, fitted to the defect values below 52 keV. Even at 50 keV, the defects are $\sim$<0.2 keV, which is below the accuracy limit anyway.

The question is now, how well does this global solution in Figure 38 fit to the individual detectors? This is shown in Figure 39 where the average defects are plotted for each of the 9 detectors on all 4 spacecraft. The red curve in each panel is the global solution once more. It can be seen that the global solution is quite acceptable on most detectors, but there are some exceptions, most noticeably on SC4, detectors 6–8. However, these are the ones affected by very wide pedestals (Figure 5) and for which the energy channel 1 thresholds are set higher than for the others. This could possibly play a role here.

Note also that the detectors 1–3 on SC3 are empty. These are the ones subject to solar contamination (Section 5.1.4) and therefore were removed from the study right from the start.

We therefore conclude that the global solution in Figure 38 is perfectly acceptable for all the individual detectors. Some fine tuning might be possible by fitting each detector separately, but the effort is not worth the slight (and probably insignificant) gain.

With the global solution, we get a formula for the corrected electron energy as

$$E' = 0.0091E^2 + 0.0728E + 23.8153, \quad \text{for } E < 52 \tag{2}$$

where E is the "original" energy without the defect, and E' is the original plus defect. In particular, for $E = 37.3$, $E' = 39.2$ keV, which now becomes the new ideal value for channel 1 and serves as the target for the spectral rebinning.

It remains now only to see how well this solution works. Once again, a 12-year database is produced, this time with the new IES calibration version V330. Figure 40 shows the fit-to-flux ratio, the mismatch parameter, for the 4 spacecraft for the same two periods as in Figure 36. There is still considerable scatter in the individual results, but on average, the mismatch is now greatly improved.

We can be hopeful that we have finally corrected this thorny problem that has plagued us so long.

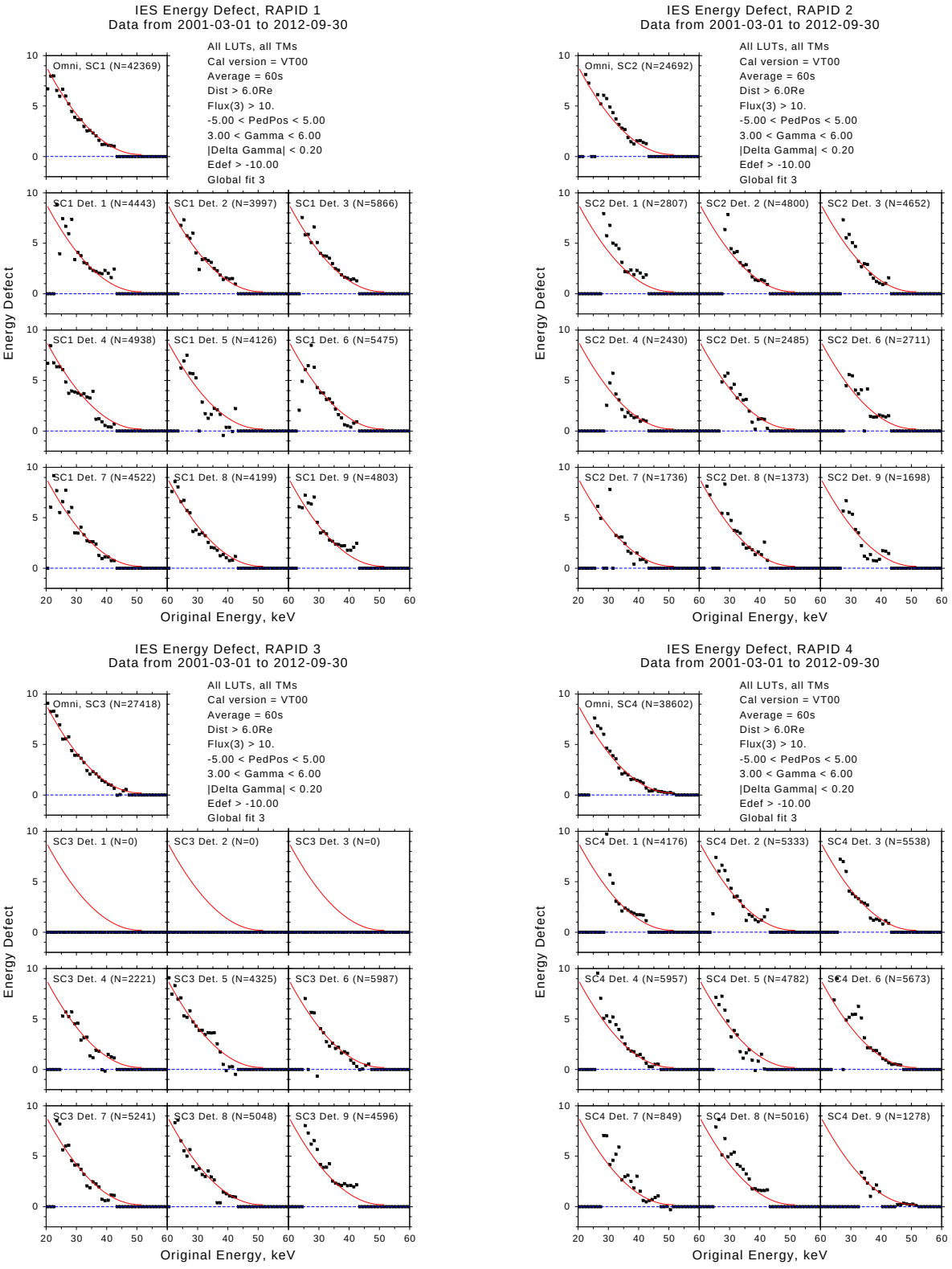

Figure 39: Energy defect for each detector on all 4 SC for all modes; the red curve is the fit from Fig. 38 superimposed on each panel.

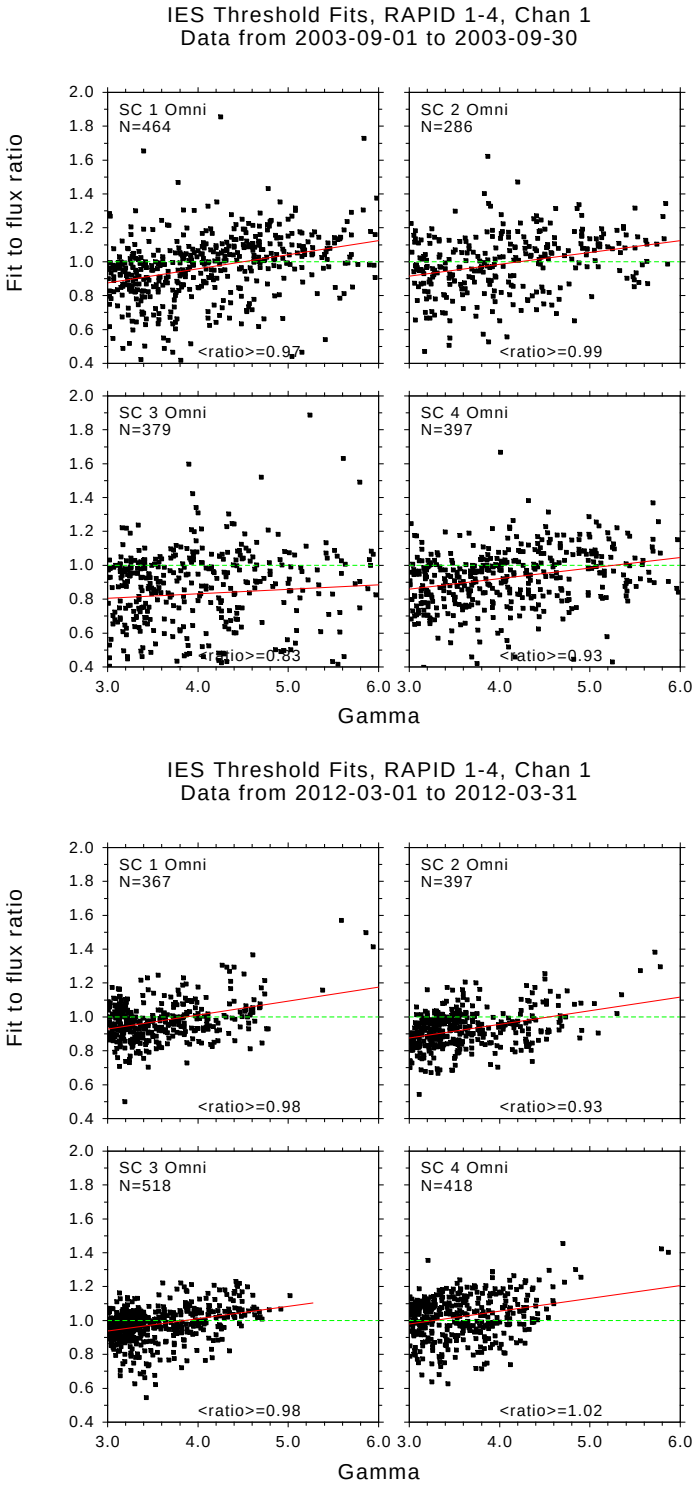

Figure 40: Ratio of extrapolated to measured flux in energy channel 1 after adding the energy defect. Data produced with IES calibration version V330.

8 Automatic Spike Removal

Like any physical instrument, RAPID is subject to random glitches in its data stream subject to various external and internal causes.

For example, very often at turn-on, as the instrument is booting, there can be some leftover garbage in the buffers as the data outputting begins. Or mode changes can also cause displaced data. And there are frequent times when a complete spin is skipped, resulting in random values in the buffer either before or after the skip. This can happen in both electron and ion data.

As an example of an external cause is the turning on of thruster thermistors, as described in Section 8.2 below.

The next sections explain how these two types of noise, or glitches, can be automatically removed during the data processing.

8.1 The Despiking Procedure

The rules for detecting a spurious data spike are basically quite simple:

> Spikes are defined as single records that are *significantly higher* than their *neighbours*.

The words in italic are the things that need better defining. A simple ratio is not sufficient (like 10^5 times the values on either side) since this could be within statistical noise, and if the neighbours are 0, then what do you do?

After much experimenting, we have decided to use the following criteria:

- The data from a single record (spin) are summed over all directions and energies to provide a single value for each record.
- Neighbours are the 5 records on either side of the record to be tested, provided there is no data gap (time difference of >1 min.) within them. At a data gap, the 10 records on the one side are taken as neighbours, and the test point is then not centered.
- For the test parameter, we need
  1. the value V of the test record;
  2. the average A of the neighbours (may be zero);
  3. the expected deviation σ, found from the standard deviation of V and the actual measured variation of the neighbours; thus if the neighbours are noisy, the expected deviation is increased.
- The condition for declaring the test record to be a spike is that

$$\frac{V - R \times A}{\sigma} > L$$

We use the values of $R = 50$ and $L = 5$, which appear to give acceptable results, conservative enough that only extreme spikes are removed.

An additional condition is also required:

- The test record must be at a time jump of at least one record.

This last ensures that very short-lived but real events are not removed. During the test phase such “spikes” were discovered, but which with closer inspection were clearly physically real.

Figure 41 demonstrates data with and without the spike removal applied.

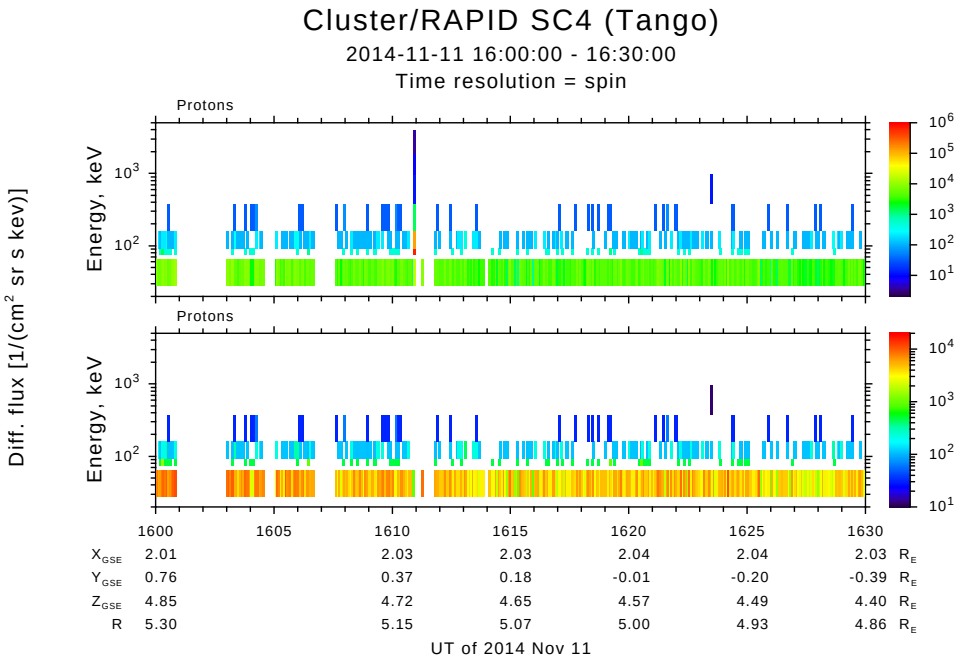

Figure 41: Sample of proton data without (upper panel) and with spike removal (lower panel).

8.2 Heater Spikes (Hatchets)

Another source of spikes in the electron data is the turning on of thruster thermistors (heaters) near the RAPID instrument, which create a brief voltage surge that causes the IES pedestals to shift drastically, with resultant noise in the electron data. These occur at regular intervals of ∼30 min. as the thruster temperature is regulated.

Figure 42, upper panel, shows such spikes in SC1, which started to show up around 2012, and which have become slowly stronger over time. These spikes are really only visible when we are down in the background level; they are not that large. They are also to be seen on SC4, although not so obvious or intense.

These spikes were first observed in 2005 during the months of August and September, on SC2 and SC4. Then they were very much stronger, but like those currently on SC1 and SC4, their times correlated very well with those of the thermistor firing. (Figure 43, upper panel.)

The angle-angle plot in Figure 44 shows the shape of these spikes: they occupy a single sector in head 2, and a double-sector in head 1 (which has only 8 spin sectors in all, unlike head 2 with 16). It is possible to detect these spikes by means of this “hatchet” shape. The rules are:

- take data from heads 1 and 2 only;
- find the 4 pixels with the highest counts;
- check if they are all in the same sector or double-sector (need not be connected);
- check if ratio of these 4 pixels to the rest is over a given threshold;
- if so, remove this record.

Take 4 pixels to ensure that more than one head is being tested; take no more because there are weak hatchets that have only 4 points. And test that the 4 have counts well above the other pixels to avoid being at noise levels.

The lower panels for Figures 42 and 43 show the results of removing these hatchet spikes.

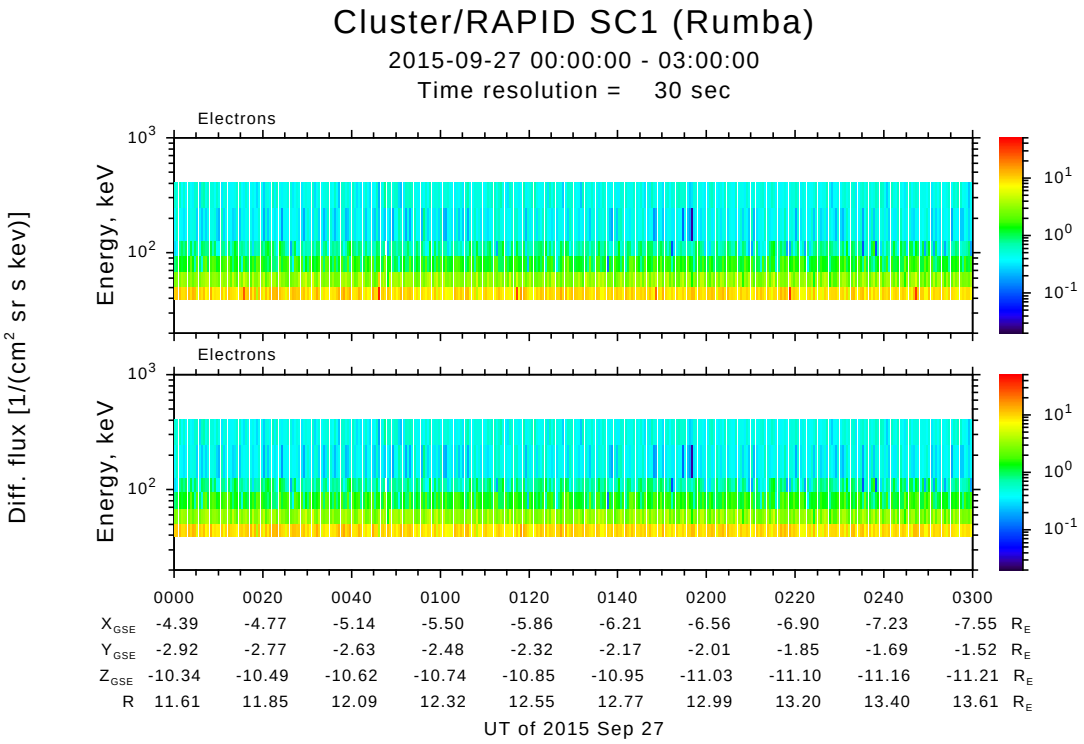

Figure 42: An example of heater spikes (hatchets) on SC1 in the electron data (upper panel), with the result of their removal in the lower panel.

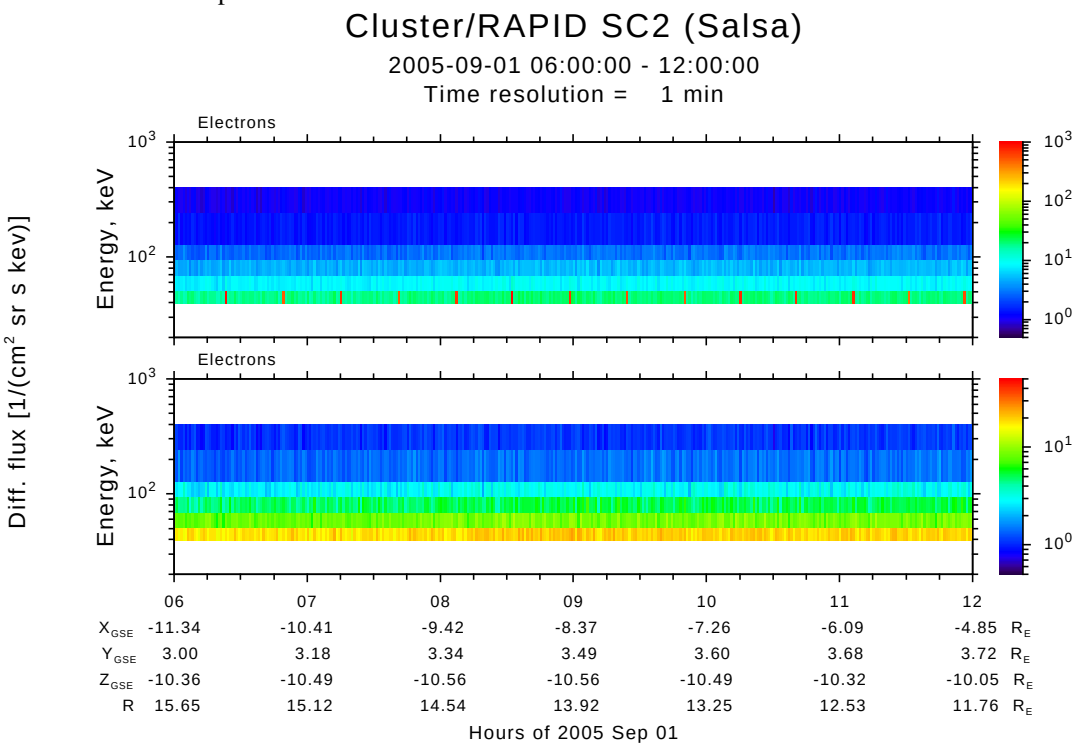

Figure 43: An example of the extreme heater spikes on SC2 in the electron data (upper panel), from August-September 2005; the same plot with their removal is shown in the lower panel.

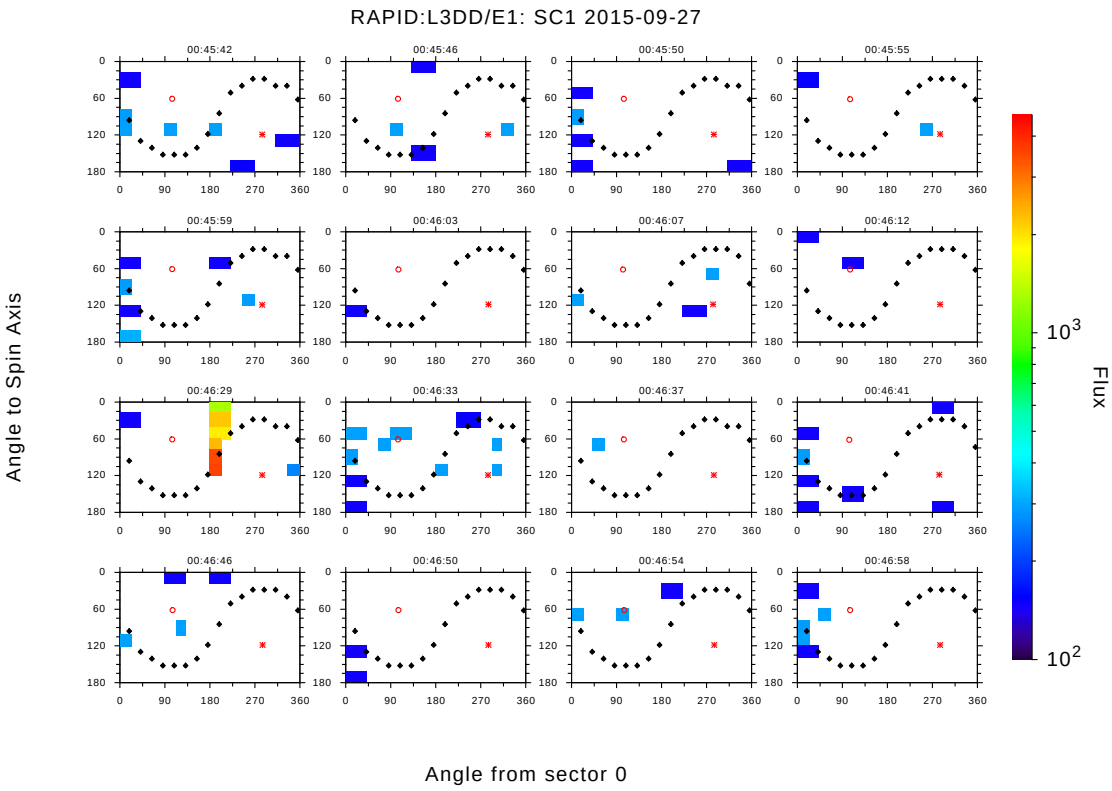

Figure 44: Angle-angle plots showing the shape of the heater spikes, that they are restricted to a single sector in head 2 and to a single double-sector in head 1. This typical shape reminds us of a hatchet (small axe), hence the name for this spike.

9 IES Detector Decay and Detector-to-Detector Corrections

This section describes version 15.5 of the calibration corrections of the IES electron spectrometer to compensate for the electron "donut" effect: long-term degradation affecting most the detectors looking into the perpendicular direction with respect to the spin axis of the spacecraft (see Figure 2 / middle plot). As for the similar effect in the ions (Section 5.2.1), the word "donut" refers to "a hole in the middle" meaning a significant reduction of flux in the electron distributions in the direction of the ecliptic plane (see Figures 45 and 46). If not compensated for the donut effect would lead to a false conclusion that there is a bidirectional flow of electrons along the spin axis. Unlike in the case of the RAPID/IIMS ion spectrometer we are able to compensate for this missing flux. The donut corrections are determined in Section 9.4. The significant degradation of the detectors started in approximately 2007 when the orbits' perigees became so low that they reached the inner radiation belt (see Section 9.7).

We also correct for properties of the instrument which have been present since the beginning of the mission: different flux levels given by each of the nine detectors when averaged over long time ranges, see Section 9.3.

9.1 The Previous Version and Reasons for Update

An earlier version of the electron data sets in the Cluster Science Archive had been corrected for the donut effect (version 13.2) based on the high-resolution E3DD_R count rates product available only during Burst Mode, which usually occurs during a few hours per orbit (P=54–57 hours). From each Burst Mode instance directions perpendicular to the magnetic field were selected (to avoid effects from pitch angle distributions) and averaged to determine one data point for each of the 9 detectors in each energy channel to describe the depth of the donut effect relative to detectors 1 and 9. A piecewise-nonlinear analytical function was fitted to this time series. The problem was that this data set was sparse and scattered as some Burst Mode intances did not have enough useful data to determine the depth of the donut effect and those instances which did gave a scattered time series. This problem was worse in the higher energy bands, where only few data points became available to sample the entire mission duration. Another problem was that after 2015 this method seemed to give too optimistic correction curves, i.e. not correcting enough, when compared to a validation data set based on omnidirectional fluxes from the product E2DD6. This old method had difficulties to determine the depth of the donut effect when there was not a strong signal available such as for the high-energy part of the spectrum or when the detectors had already degraded significantly. These problems lead to the decision to change the method.

9.2 Orbital Averages for Long-Term Calibration

For both the detector-to-detector corrections as well as for the donut corrections we use the same data set. We calculate orbital-averaged fluxes above L>7 using the Nominal Mode E2DD6 product (spin-averaged) and then apply suitable filtering techniques in order to have curves over the mission time which are then used to determine the correction factors. For the donut correction we use detectors 1 and 9 as the reference level and divide the curves of the other detectors by this reference level to determine how much degradation there is. These ratio curves are fitted by a monotonic piecewise non-linear function. The fitted parameters of this function are stored and used to calculate a value for the correction at any required time instances. The corrections are flux-independent. The data flow of the corrections is shown in Figure 47.

As mentioned above we use the E2DD6 product for the long-term calibration. This product has full polar resolution (9 directions) and six energy channels accumulated over all azimuthal directions, i.e. it is spin-averaged. During Burst Mode we simulate E2DD6 from a higher-resolution data product. An exception is spacecraft 3 where we do not have fluxes from detectors 1-3 due to contamination from sunlight (see Section 5.1.4). The orbital averages are calculated from data above L>7 to avoid contamination from the radiation belts (see Section 12). We also select only the longest integration time of 50 μs, which is the usual case and which then excludes high count rates. As shown in the flow chart of Figure 47 the E2DD6-based orbital averages as a function of the mission time are filtered before they are used to determine correction factors. Figure 48 shows the large scatter in the individual values of the orbital averages. They are first filtered with a 7-day median filter and converted into a uniformly spaced time axis. Then they are filtered either with a Wiener filter (for gain and contrast corrections) or a low-pass

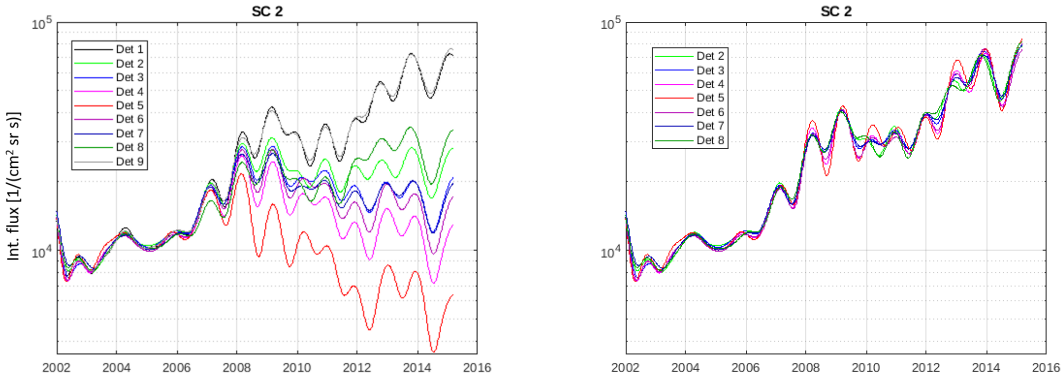

Figure 45: Orbit-averaged integral fluxes (Wiener-filrered, see text) of spacecraft 2 / energy channel 3 before and after the donut corrections. Detectors have been gain-corrected and contrast-corrected (see Section 9.3). The donut effect causes decreased fluxes and is strongest in the direction perpendicular to the spin axis (detector 5). Symmetric pairs of detectors (e.g. 3 and 7) have approximately similar levels of degradation.

filter (for donut corrections).

The E2DD6 product has six energy channels as the higher-resolution IES products have eight channels. The corrections are calculated for the six channels and mapped into eight channels so that the two highest channels 5 and 6 are mapped into channels of the high-resolution product 5->(5,6) and 6->(7,8), where the channels in the parentheses are channels of the high-resolution product.

9.3 Detector-to-Detector Corrections

Since there is no in-flight absolute flux calibrator available for IES we make relative corrections comparing the detectors to each other. Here we make an assumption that statistically in the long term all detectors see the same flux outside of radiation belts where the magnetic field direction is more randomly oriented than within the belts. The detector-to-detector corrections have two components, one constant and one a function of time: (i) a comparison of median fluxes in the early mission before the donut effect started provides constant gain corrections (see Figure 49), and (ii) detectors 1 and 9 are compared to each other as a function of time to correct their different relative degradations (see Figure 53). This we call the contrast correction.

For determining the constant gain corrections we calculate medians of filtered orbital averages (Section 9.2) before 2006 when the donut effect had not yet started (see Figure 45). Figure 50 shows the filtered orbital averages. While the curves generally have the same shape for all the detectors there are differences in the detailed shapes at specific time ranges. For calculating medians we have chosen a time range for each spacecraft providing a robust estimate for the detector-to-detector differences. The time ranges start in 2002-2003 and end in 2005-2006, except for spacecraft 4, where a shorter time range is used. However, these medians for each detector are not the final ones but are fine-tuned during the validation process of the corrected data set (see Section 9.5). The final multiplicative correction factors are shown in Figure 51. The median values calculated for each energy channel form an “average spectrum” which is shown in Figure 52.

Detectors 1 and 9 have look directions close to parallel and anti-parallel to the spin axis (see Figure 2 / middle plot). These two detectors give the reference level for the donut corrections. We assume that on the average these two detectors should give similar fluxes. The constant gain corrections adjust the levels comparing data from the early mission before the donut effect started. There are also changes in the relative levels of detector 1 and 9 as a function of time as shown in Figure 53. The two detectors degrade at a different pace which is seen as changing differences between them. This is corrected in a statistical way for each spacecraft and applied to all energy channels when possible. There are a few exceptions when these contrast corrections are determined for

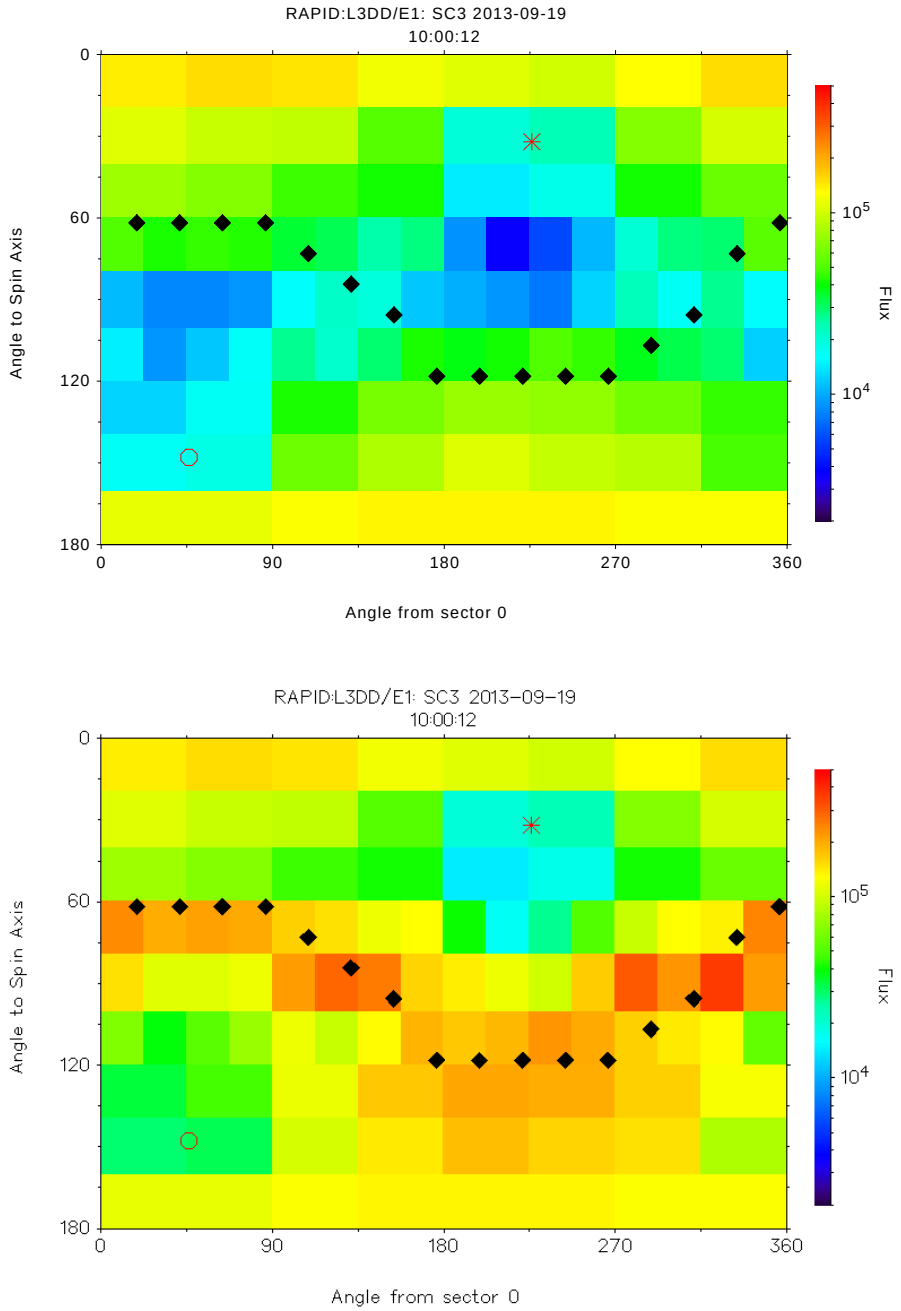

Figure 46: Example of differential flux L3DD data (9 polar and 16 azimuthal directions, 2 energy channels) before and after correction for the long-term decay effect. The circle and asterisk give the magnetic field direction and the dotted black line is the direction perpendicular to the magnetic field. The flux unit is 1/(cm^2 sr s keV).

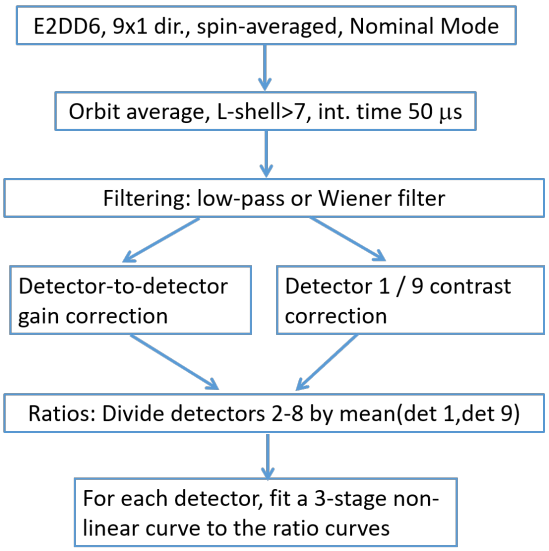

Figure 47: Data flow of detector-to-detector corrections and the donut correction (see text).

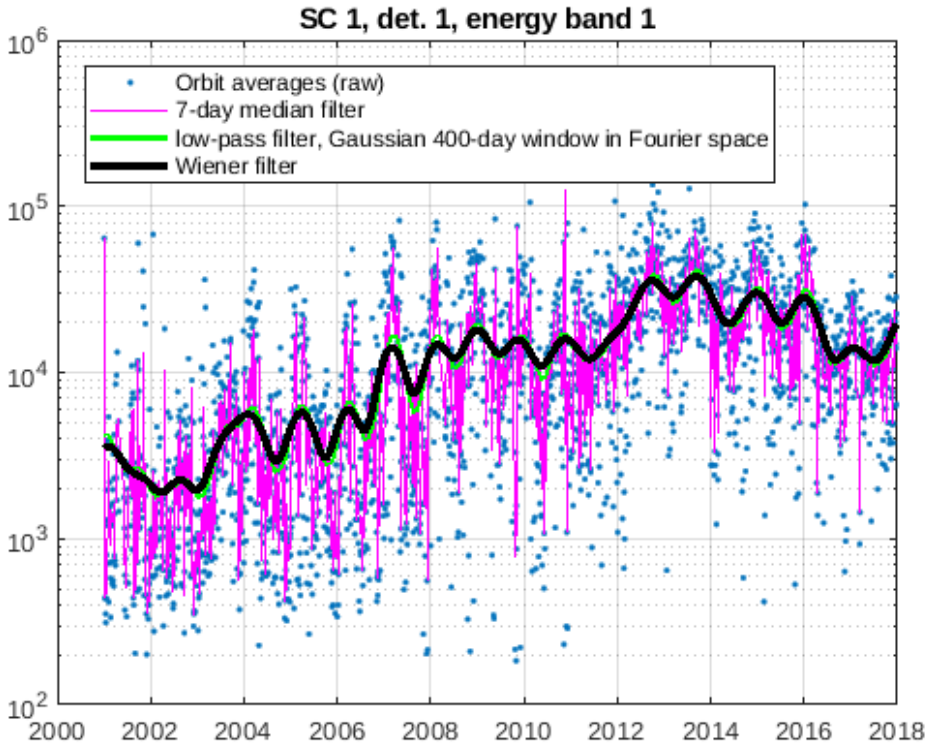

Figure 48: Orbital averages (L>7) of detector 1 on spacecraft 1 and the median-filtered and Wiener-filtered curves. A low-pass filter with a 400-day Gaussian window is shown for comparison. The y-axis is integral flux in 1/(cm^2 sr s).

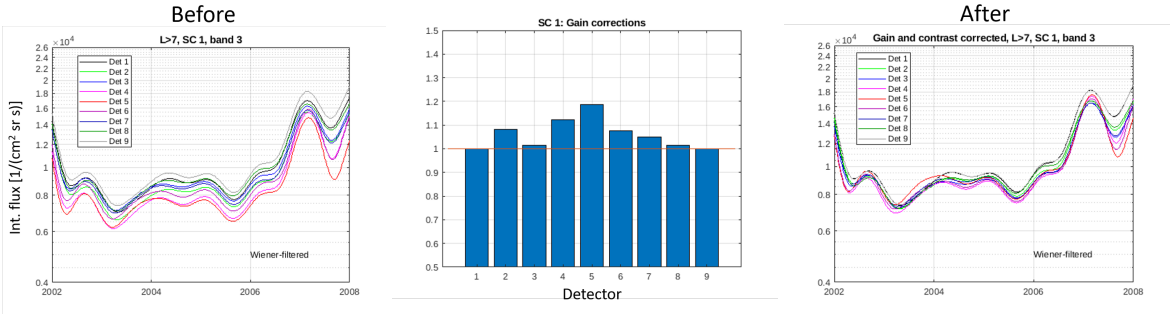

Figure 49: Different detectors give different flux levels on the average (left). Constant gain corrections are determined relating the median flux level of all detectors (middle) and the result (right) is independent of the detector (polar direction).

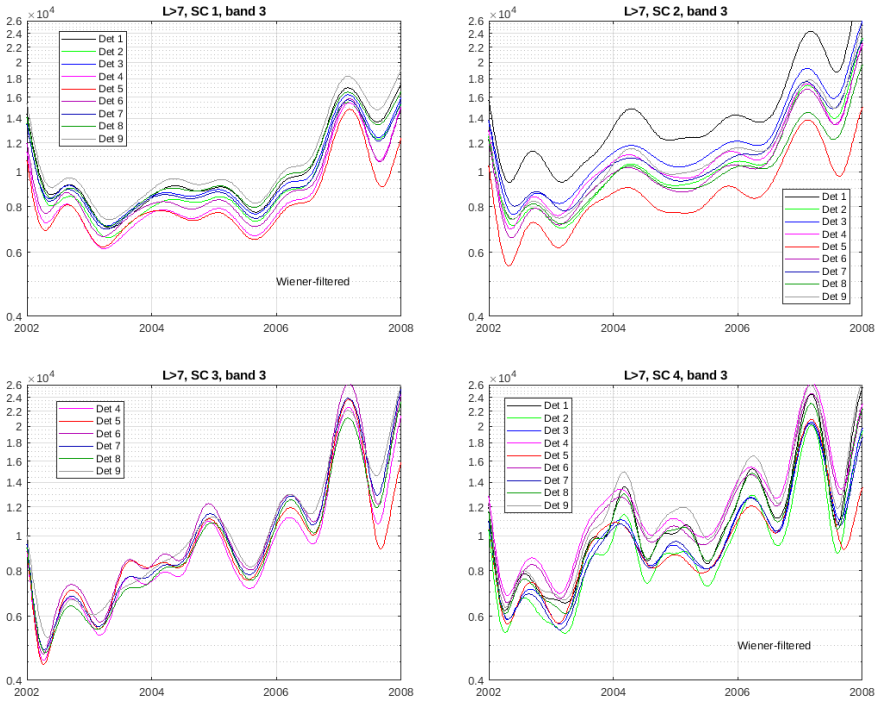

Figure 50: Uncorrected Wiener-filtered fluxes from median-filtered orbital averages (L>7) at energy channel 3 for the 9 detectors (polar directions) during the early mission. Note the scatter in the flux levels of the detectors especially on spacecraft 2 and the difference in the shape of the curves on spacecraft 4.

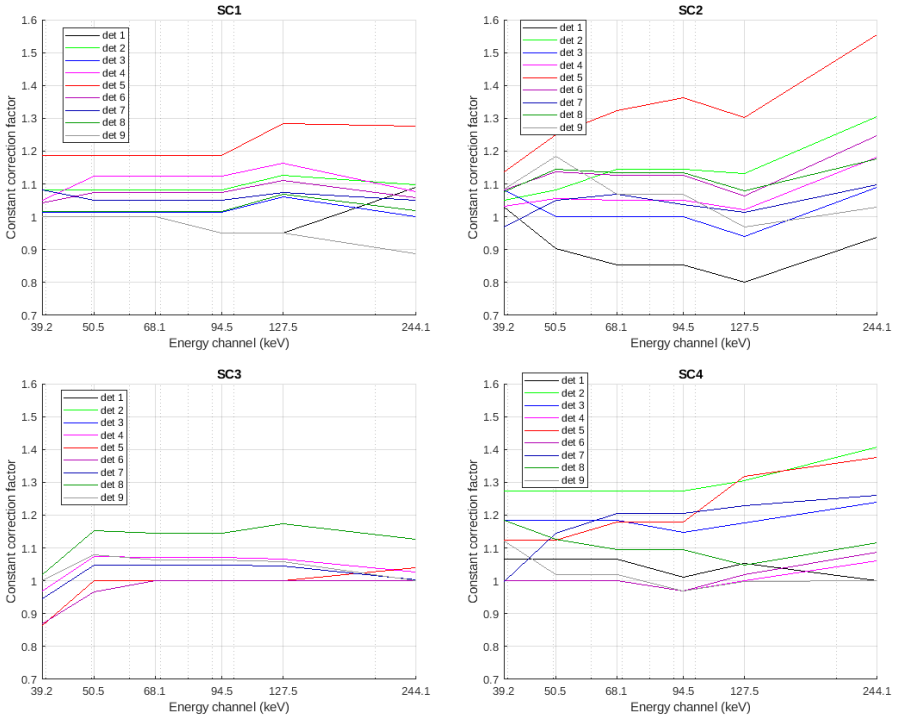

Figure 51: Gain corrections of the four spacecraft at the different energy channels.

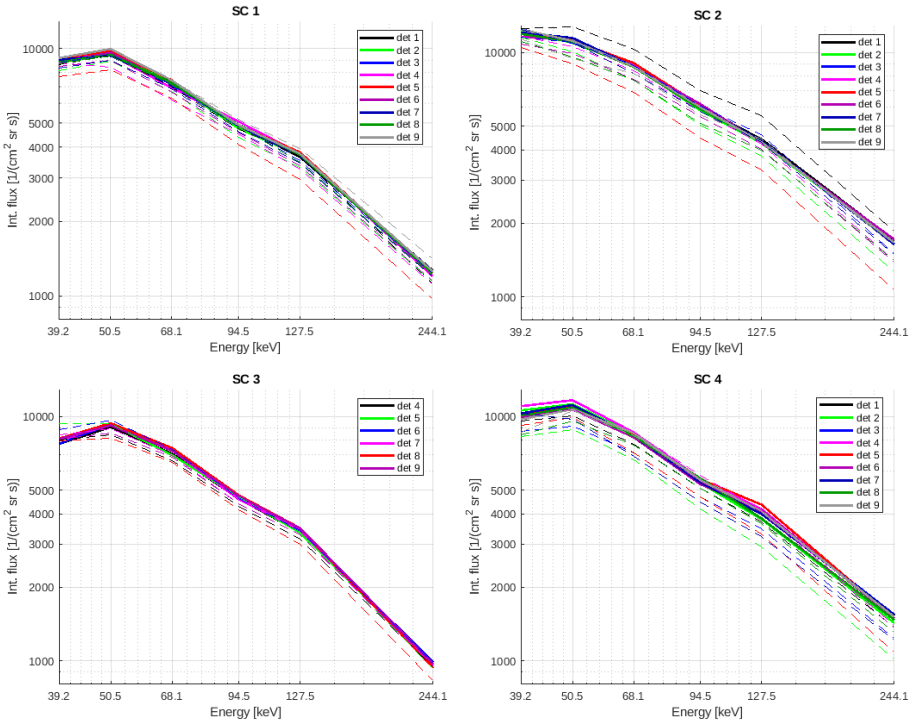

Figure 52: Medians of Wiener-filtered orbital averages (L>7) at each of the six energy channels and for the 9 detectors (polar directions) during the years 2002-2005 before the donut effect started. Solid lines: after gain correction, dotted lines: before corrections.

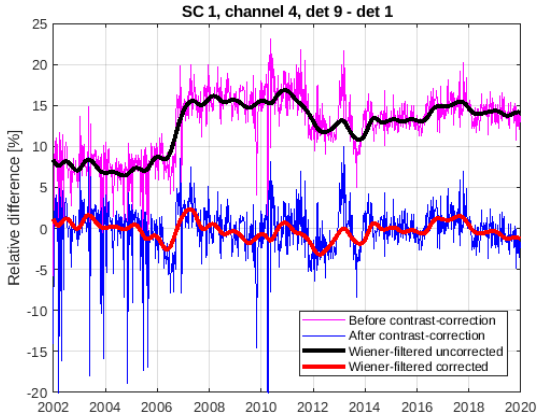

Figure 53: Relative difference between detectors 1 and 9 before and after contrast- correction. In the ideal case the relative difference would be zero.

individual channels: channel 4 of spacecraft 1, channel 1 of spacecraft 2, and channel 6 of spacecraft 4.

9.4 Donut Correction

As shown in the flow chart of Figure 47 the donut correction is based on data which is first corrected for constant gain offsets and contrast corrections (detectors 1 and 9) described in Section 9.3. These correction factors, which have been determined and saved at an earlier stage, are applied to the orbital averages (see Section 9.2) after the initial filtering by a short-window median filter and before the final filtering. For the donut corrections we apply a low-pass filter and then calculate the ratio where each of the detectors 2-8 is divided by the reference level (see Figure 54), which is the mean value of the filtered detectors 1 and 9.

There are significant fluctuations in the ratio curves. Since the data are omnidirectional in the azimuth direction (see Section 9.2) there is no possibility to exclude certain directions to avoid effects from pitch angle distributions as was done in the old method (see Section 9.1). Hence, we do not use the whole data set but select months from each year to minimize the fluctuations on the ratio curves, as shown in Figure 54 / right panel. The months selected in this way are coincident to the times of the year when the spacecraft are flying mostly in the tail region and do not cross the magnetosheath. We fit a 3-stage analytical function (consecutive half-Gaussians) to the ratio curves. The fit is done independently for each detector and energy channel. Examples of the fitted curves are shown in Figures 55 and 56. The starting time of the donut effect in these modelled curves is in September-October 2006 for energy channels 1-5 and later for channel 6 (October 2008 for spacecraft 1 and 4, October 2007 for spacecraft 2 and November 2006 for spacecraft 3). In all spacecraft, the degradation effect is stronger at channels 1-4 than at channel 5 (127.5–244.1 keV) or especially channel 6 (244.1–406.5 keV), where the effect is weakest and starts to be seen later than at lower energies. An example of this is shown in Figure 56 / left panel.

9.5 Validation and Caveats

The validation and quality-checking process of the corrections has been done in an iterative way to fine-tune the gain corrections and some parameters (starting time of the donut effect, transition times between the stages of the piecewise-nonlinear function, the exact time range selected from each year of data) of the analytical fit in the case of donut corrections. We use the same data set of orbital averages (see Section 9.2) as used for determining corrections but do not apply any filtering. For each time instance of orbital averages we calculate the relative

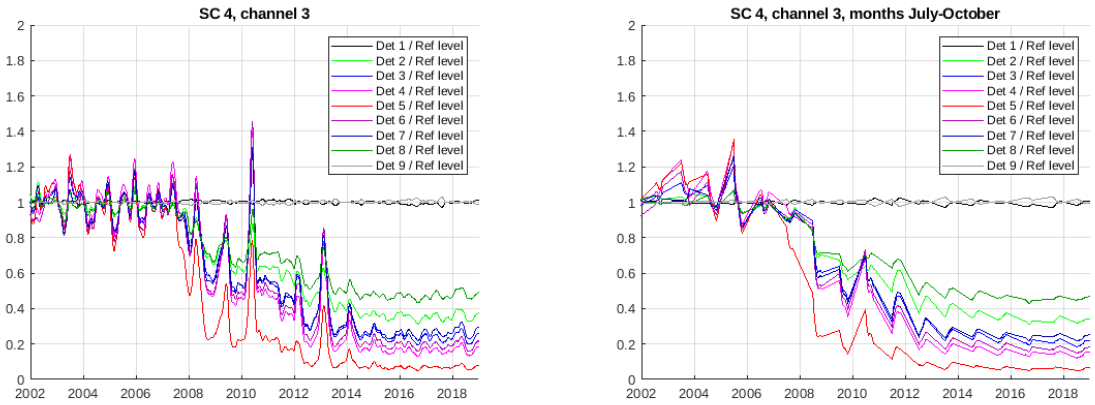

Figure 54: Variations in ratio curves are large when all data is included (left). They can be reduced by selecting a suitable time of year (right, data from July-October of each year). The data have been filtered with a low-pass filter (120 days Gaussian window) and then divided by the average of detectors 1 and 9.

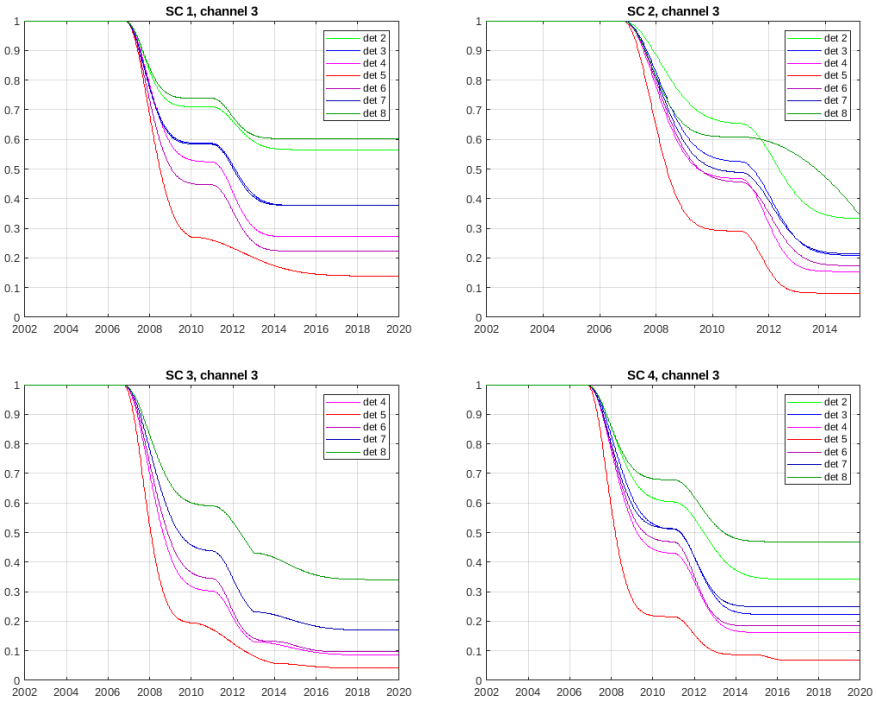

Figure 55: Analytical correction curves for energy channel 3. The flux is divided by the value of the correction curve. IES on Spacecraft 2 had a partial failure in March 2015 (see Section 10) and no calibrated orbital averages are available beyond that.

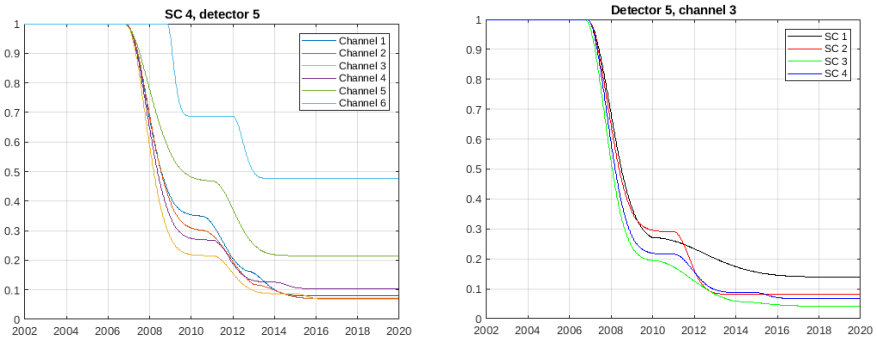

Figure 56: Analytical correction curves for the donut effect. Detector 5 of spacecraft 4 at different energies (left). The two highest energy channels have significantly less degradation than lower energy channels. This is similar for all spacecraft. The right panel compares the middle detector (detector 5) of the four spacecraft (see also Section 9.7).

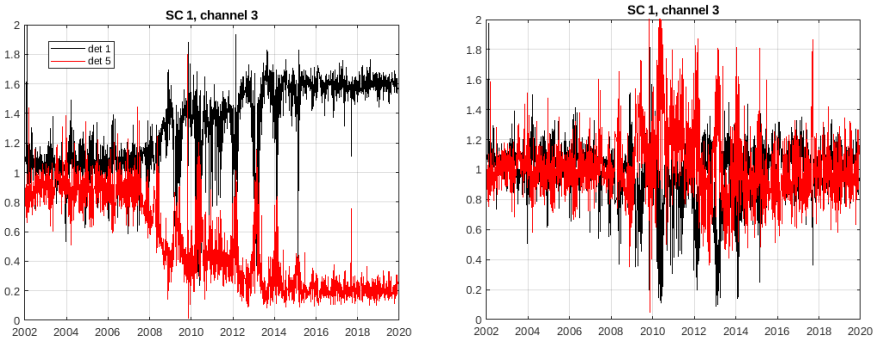

Figure 57: Relative contributions (see Equation (3)) from detector 1 and detector 5 before (left) and after gain and donut corrections have been applied. In the ideal case these unfiltered orbital averages would scatter around one. Note the offset in the early mission until 2007 between the detectors (left panel) which has been corrected by the gain corrections (right panel).

contributions of each of the detectors:

$$b_i\,(t) = \frac{\mathrm{det}_i\,(t)}{\sqrt{\frac{1}{N}\sum_{j=1}^{N}\mathrm{det}_j\,(t)^2}}, \tag{3}$$

where b_i is the relative contribution of detector det_i (see Figure 57) and N is the number of detectors[1]. This method gives the relative contributions independent of the total flux at any given time: it shows if some detector seems to give too high fluxes ($b_i > 1$) or too low fluxes ($b_i < 1$) relative to other detectors. These b_i values in the early mission until 2006 are used to fine-tune the constant gain corrections (see Section 9.3).

9.5.1 Caveats

As explained in Section 10 IES on spacecraft 2 experienced a partial failure in March 2015. Gain corrections and donut corrections have not been determined beyond that time for spacecraft 2. In spacecraft 3 we do not have fluxes of one of the detector heads (detectors 1–3) due to solar noise as described in Section 5.1.4.

[1] N=9 except for spacecraft 3 N=6.

We have inspected the long-term relative fluxes based on equation (3) and found that on some time intervals the corrected data are not optimal. If a detector deviates 10–25% from the others in a long time range then we say that it is "slightly high" or "slightly low". If the deviation is greater than 20–25% we say that it is "high" or "low". Note that only detectors 5 and 6 have long-lasting deviations.

- Spacecraft 1 / energy channel 1: detector 5 in 2010 and first half of 2011 is too high and detector 6 in the years 2016-2019 is slightly too low.
- Spacecraft 1 / energy channel 2: detector 5 in 2010–1Q/2012 is slightly too high and detector 6 in the years 2016-2019 is slightly too low.
- Spacecraft 1 / energy channel 3: detector 5 in the years 2010–2011 is too high.
- Spacecraft 3 / energy channel 1: detector 5 in first half of 2010 is too low and in 4Q/2018 and first half of 2019 slightly too low.
- Spacecraft 3 / energy channel 2: detector 5 in first half of 2012 is slightly too low and from 4Q/2012 to almost mid-2013 too low.
- Spacecraft 3 / energy channel 3: detector 5 from 4Q/2012 to almost mid-2013 is too low.
- Spacecraft 4 / energy channel 1: detector 5 in second half of 2010 and in 2011 is slightly high and in 4Q/2013 and in first half of 2014 the same detector is too high.
- Spacecraft 4 / energy channel 2: detector 5 in 4Q/2013 and first half of 2014 is slightly high.
- Spacecraft 4 / energy channel 3: detector 5 in 3Q/2014 to 3Q/2015 is slightly too low.

9.6 Mission Overview

An overview of the behaviour of the electron fluxes on all 4 spacecraft for the whole mission lifetime is shown in Figures 58 and 59, for uncorrected and corrected data, respectively. Each point is a monthly average of the fluxes taken above L-value of 7.

In Figure 58 one clearly sees the decay of head 2 (detectors 4–6, red points) starting around 2007, whereas the fluxes in Figure 59 have been adjusted with the corrections described in this section.

Also clearly visible is the partial failure on SC2 in 2015 (Section 10), after which no further corrections were taken.

9.7 Environmental Effects

As shown by Figure 55 all detectors showed relatively fast degradation in 2007–2009 and again with a smaller amplitude in 2011–2013. In this section we present environmental factors which may explain the timing of this degradation. During the long Cluster mission the 4 spacecraft have spent less than 5% of each orbit within the radiation belts until 2009 after which this fraction increased significantly and occasionally reached values of more than 12%, see Figure 60. The definition of radiation belt in this plot is L<6. The upper right panel shows the L-value during the orbits. The minimum L-value started decreasing in late 2006 and continued to decrease until 2011 when the perigees of the orbits reached their minimum and started increasing. The minimum L-values reached the level of the early mission again in 2014–2015.

Using the orbits of the spacecraft and the SPENVIS (Space Environment Information System) tool of ESA [*Heynderickx et al.*, 2002; *Kruglanski et al.*, 2009, 2010] we have computed the absorbed radiation dose as a function of time (see Figure 60). The component which correlates with the "donut effect" is the trapped protons with an increased dose in 2007 compared to any of the earlier years of the mission. The dose increased until 2009, remained at a high level until 2012 and then decreased in 2013. The perigee of the orbits was low enough to bring the spacecraft down to the altitude of the inner radiation belt (approximately L=1.5–3) in 2007-2014. The timing of the first degradation in 2007–2009 coincides with the increasing radiation dose from trapped protons. The linear

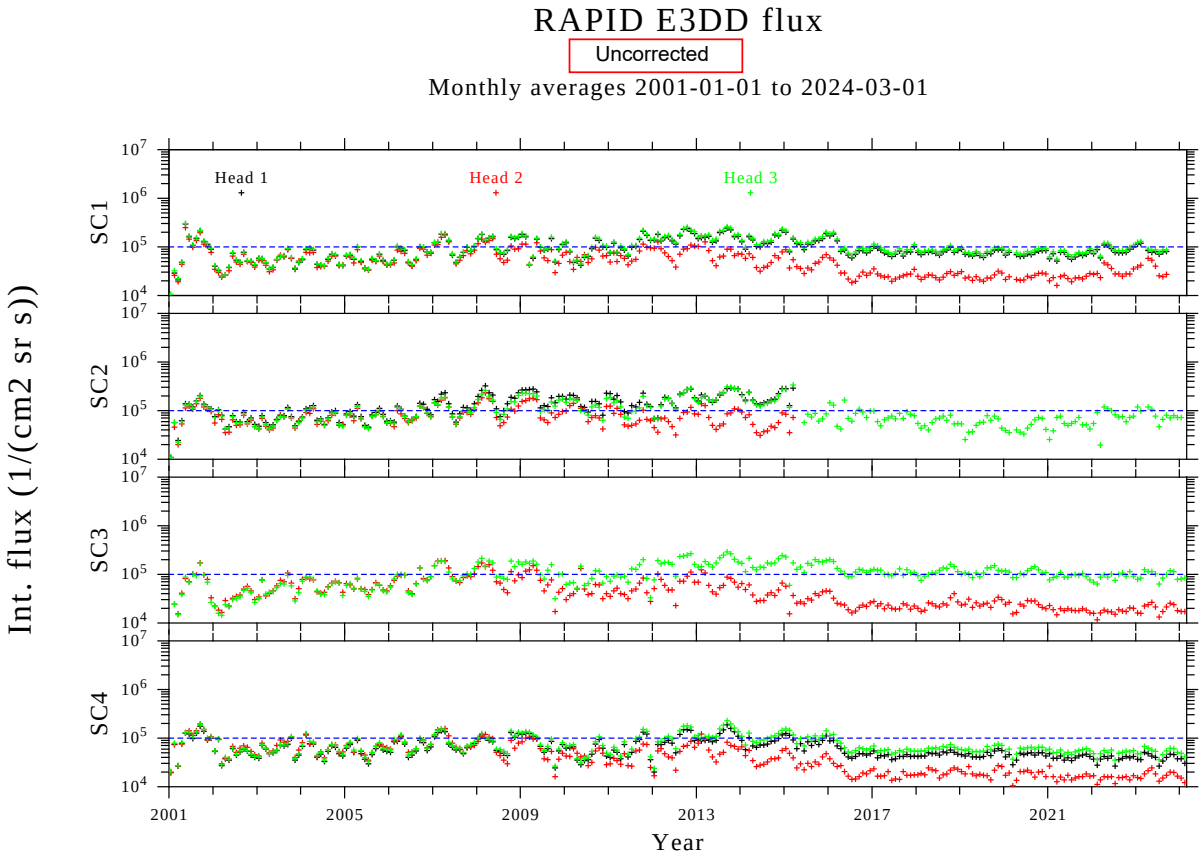

Figure 58: Uncorrected electron fluxes over the mission lifetime for all 4 spacecraft. Each point is a monthly average of the fluxes in each of the 3 detector heads, for L>7. The horizontal dashed line marks a certain level for comparison between the panels.

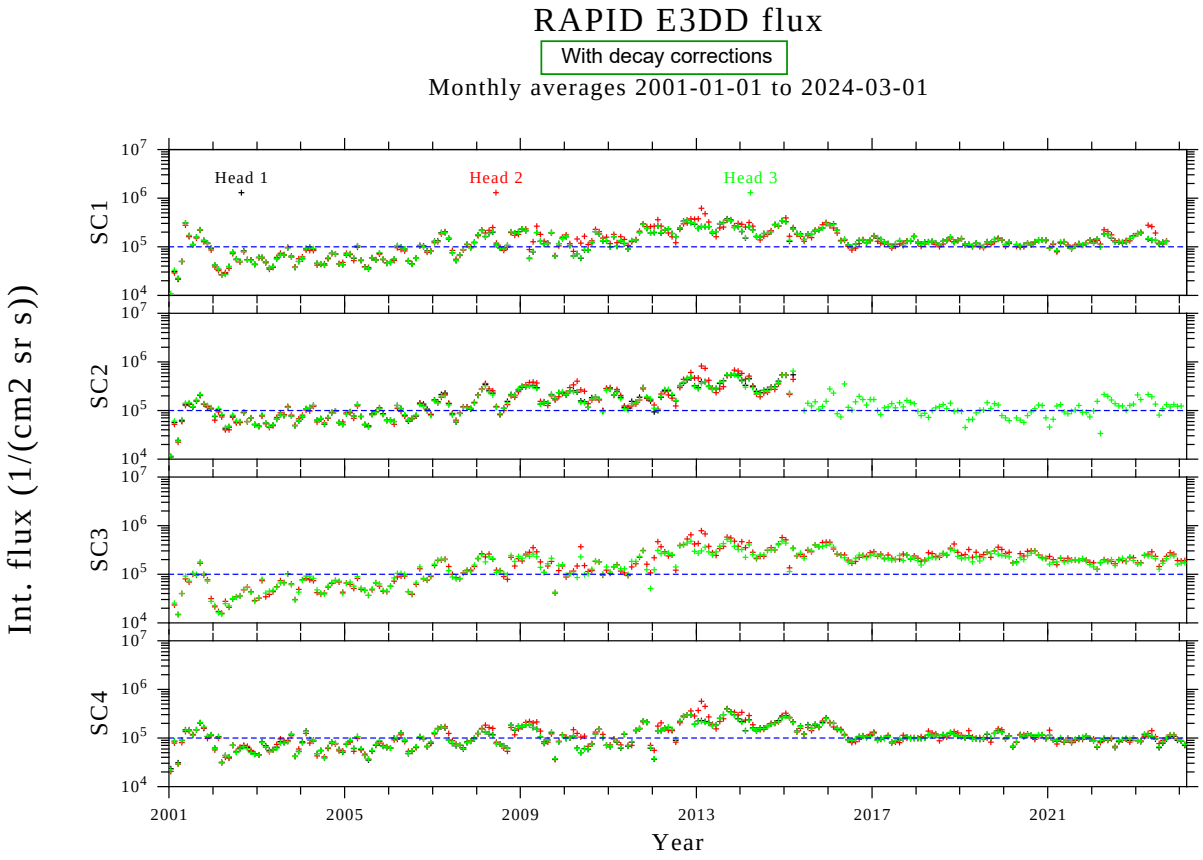

Figure 59: The same as Fig. 58 but with the decay correction included.

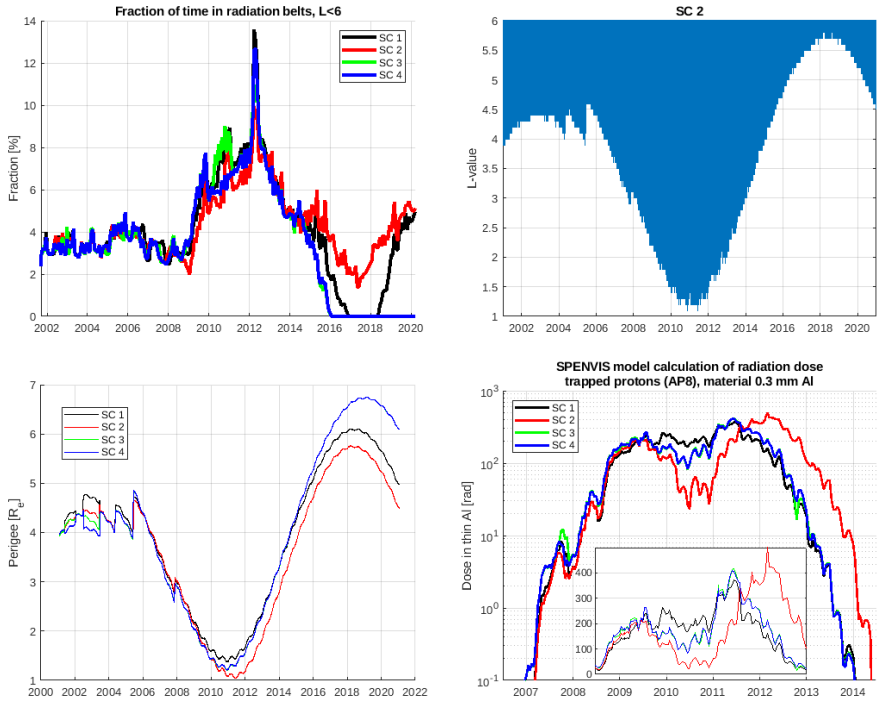

Figure 60: Upper row: Fraction of time spent below L=6 in each orbit and the L-values of spacecraft 2 every half an hour (NASA Satellite Situation Center https://sscweb.gsfc.nasa.gov/). Other spacecraft have slightly higher minimum altitude of L≈1.5. Lower row: perigee (Cluster Science Archive). The radiation dose (lower right) has been modelled with the SPENVIS tool using the actual orbits (this work has been contributed by Cassian Herbon). The dose is relatively high when the perigee is $< 3\,R_E$. Spacecraft 3 and 4 are on similar orbits and their curves are mostly overlapping.

scale plot of radiation dose in Figure 60 shows that there were two maxima, the second one in 2011–2012 being the higher maximum. This is compatible with the second decrease in detector efficiency in 2011-2013.

The dose as a function of time indicates that spacecraft 3 and 4 had appriximately the same dose. This is compatible with the fact that, as of 2005, they are on the same orbit, but with a time shift. Figure 56 / right panel compares the middle detector of the four spacecraft, namely their analytical fitted curves. While the original data set has been smoothed before calculating ratios to the reference detectors and then an analytical curve with a fixed starting time has been fitted, the correction curves of spacecraft 3 and 4 are similar given the uncertainties and given the fact that they are independent components. Detector 5 in spacecraft 2 had a lesser dose in 2010 than the other spacecraft, which is consistent with the less deep correction curve in that year. On the other hand this spacecraft absorbed a larger dose in 2012 and reached a similar level of degradation as spacecraft 3 and 4.

The fact that the degradation has a “donut” like shape can be explained by the orientation of the spacecraft. The solar aspect angle is around 90 deg with a few deg annual variation, which means that detector 5 looks perpendicular to the magnetic field while in the radiation belts and collects more particles than other polar directions (=detectors). The instrument is a simple pin-hole camera without electrostatic or magnetic deflection. It has a foil designed to protect against incoming ions up to about 350 keV.

The perigee had its maximum in 2018–2019 and will be decreasing until the end of the mission.

10 Partial Failure of IES on SC2

On March 26, 2015, at 07:00, the IES on SC2 started to go crazy, in that the counts in the pedestal channels either went to zero or were shifted by a large amount, depending on the detector. This would indicate enormous pedestal displacements, making subsequent data analysis impossible.

The unit was then rebooted twice in an attempt to restore it, but without success. We then ordered a special histogram mode test to get a more detailed picture of the output, something that normally is done just once a month. Fortunately the previous histogram test had just been carried out a few days before the failure, on March 22 (Figure 61) so a good comparison of before and after could be made.

The pedestals in the histogram test of April 2 are shown in Figure 62 are clearly very pathological. In detectors 1 and 2, they have disappeared completely, in 3, 4, 5 they are extremely narrow and even distorted, in 6 there is just an almost uniform background, while in 7, 8, 9 there are still recognizable pedestals, although much broader than before.

It was decided to suppress the data processing for IES on SC2 for the time being, but to closely monitor it with the intention of possibly recovering the three detectors that still appeared usable. The monthly histogram tests were continued, and indeed by Oct 20, 2015, (Figure 63) it seems that they have stabilized in that the pedestals are much as they were before the failure, although slightly shifted and somewhat broader, and that the additional background noise is gone. Subsequent analysis of the regular data indicates that the recovery likely took place before mid-June, 2015. Data processing has been reactivated as of June 12, 2015.

The data processing was altered to allow for missing detectors, meaning the omnidirectional IES data is constructed from only the 3 remaining ones. Thus it is a rather lopsided omnidirectional result.

However, several other problems now also became apparent.

Channel definitions: because the pedestals have shifted from their previous positions, it was necessary to redefine the energy channel thresholds, something that is done every few years anyway. The new values were uploaded to the RAPID unit on May 9, 2016.

Autoswitching: the automatic changes of integration time depending on count rates needed to be corrected, since it was previously using data only from non-functioning detectors. This change was uploaded to the RAPID unit on June 17, 2016.

New noise spikes: Figure 64 shows the noise spikes that are now present after recovery; a method has been developed to detect and remove them automatically, shown in the lower panel. However, there might still be some spikes that survive the algorithm. At other times, there are so many spikes removed that the cleaned data show many long data gaps. This method is applied in the data processing on the ground and so can be done retroactively to the entire time period.

Possible decreased sensitivity: it was at first suspected that the recovered detectors were considerably (<10%) less sensitive than on the other spacecraft. Initially the geometry factors were corrected accordingly for the deliveries to CSA. However on further inspection, it became obvious that the "corrected" data were an order of magnitude (or more) above the others, and the uncorrected data were only slightly different. Thus this erroneous correction has now been removed from the data deliveries of the 4th release.

In summary, we have a partial recovery of the IES unit on SC2, making use of 3 of the 9 detectors, but one should observe the following caveat:

> *Given the many issues listed above, plus the partiality (3 out of 9 detectors) the recovered IES data on SC2 can not be used reliably for pitch angle distributions, spectra determination, or even for absolute fluxes. They can however be used for indicating the existence of electron events and for their timings.*

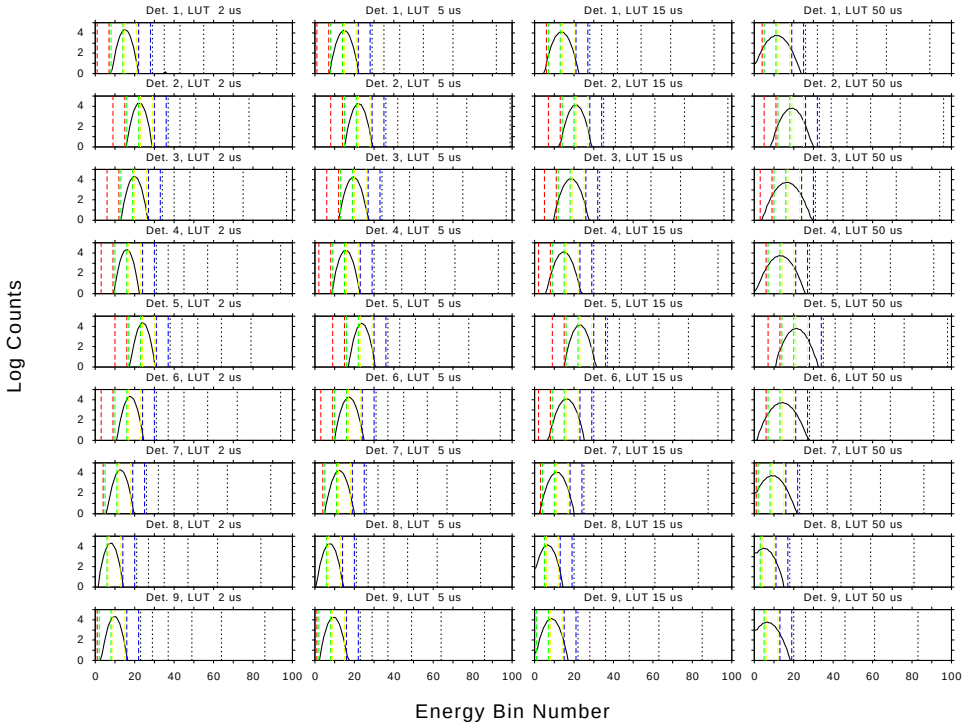

Figure 61: A healthy set of pedestals on SC2 from the histogram data taken a few days before the failure.

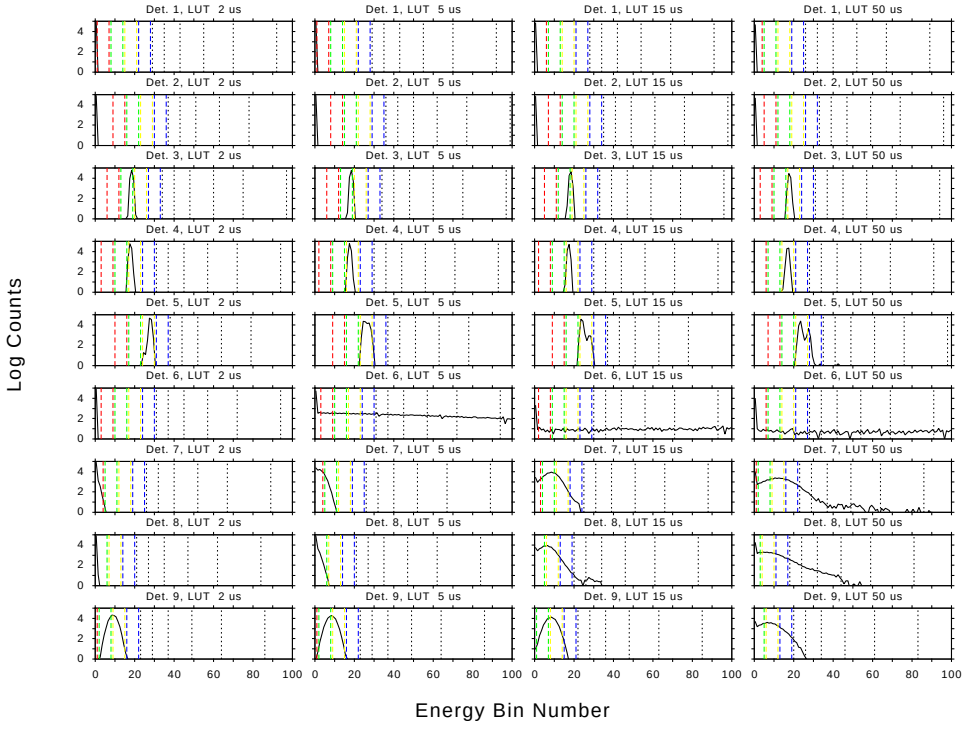

Figure 62: The sick pedestals on SC2 from the special histogram data taken a few days later.

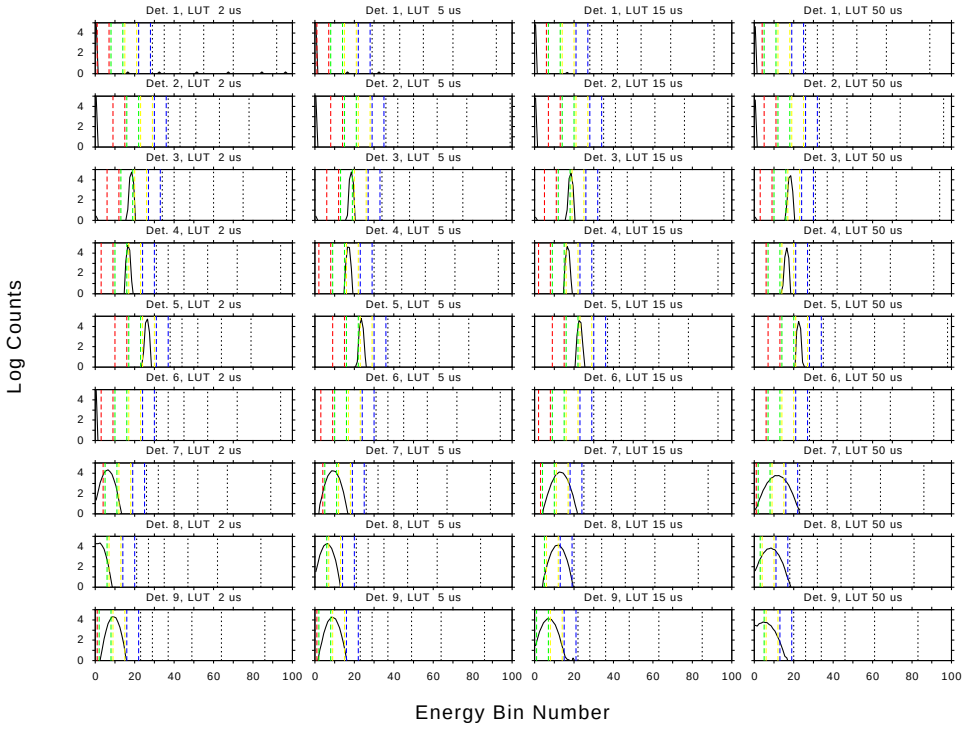

Figure 63: Histogram results from Oct 20, 2015, showing that the pedestals in detectors 7, 8, 9 have settled down, while those in the other detectors are still hopelessly lost.

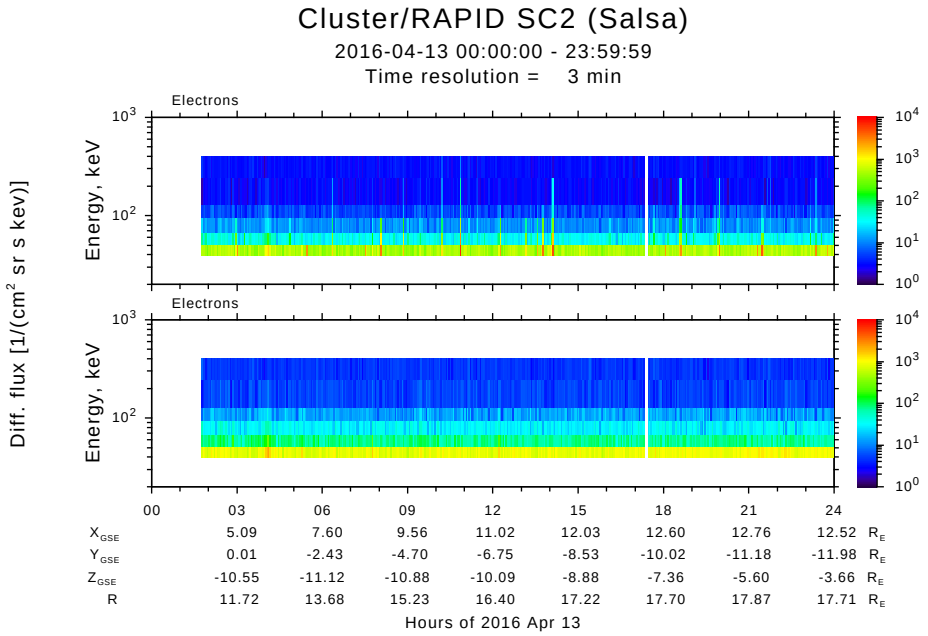

Figure 64: Additional noise spikes appear in the IES data after the partial recovery (upper panel) which can be detected and removed (lower panel).

11 Electron Background Counts

11.1 The Background

It has long been observed that the count rates in the IES electron detectors never go exactly to zero, but always remain at a certain relatively constant low level, well below $1\,\mathrm{c\,s^{-1}}$. The background is also spread over all the energy channels, as can be seen in Figure 65.

It was only after sufficient data had been accumulated that a proper analysis could be undertaken. The first question is whether this noise is some kind of internal buzzing at a fixed rate, or of stastical nature. Initial investigations confirm that it does indeed obey Poisson stastistics, so that it is random. The next question is whether it is internal or external. To this end it is desirable to know the long-term time dependence, if any.

11.2 Background Product

To carry out such an analysis we first need a database of the noise. We create new data products called `IES_BG_R` (count rates) and `IES_BG` (corresponding fluxes), although both are derived from the actual number of counts per measurement.

We take the `E2DD6` counts in NM (which can be emulated from `E3DD` in BM), and accumulate the counts in each of the 6 energy channels, 9 detectors, and 4 spacecraft, for each spin (∼4 s) over a "long" period of time. In this case "long" is meant to be long enough to carry out a reasonable statistical analysis on the low numbers involved.

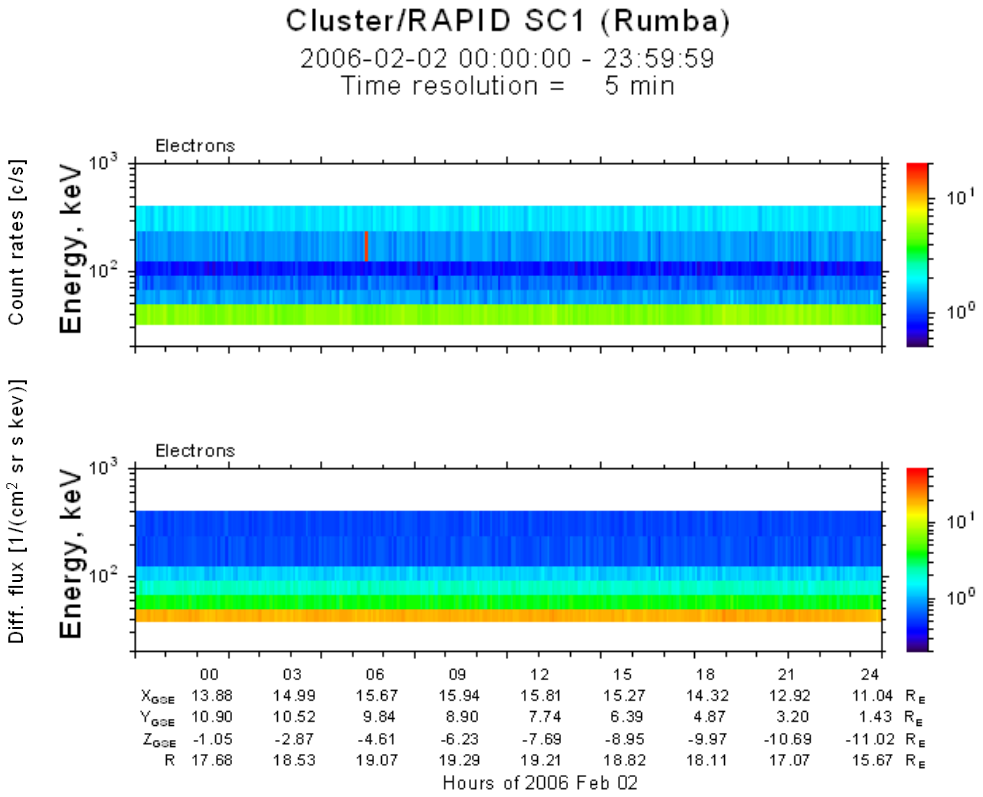

Figure 65: Example of electron background, a non-zero floor to the count rates when averaged over longer periods of time. Upper panel shows raw count rates, the lower one differential flux. Note that the background exists in all energy channels.

We use 1 hour, which is about 900 measurements. The majority of these measurements contain zero counts, and a number of them a single count, and a few 2 or more. The average is less than 1 per spin, which makes the statistical analysis tricky.

For example, here is a sequence of 40 measurements from the data in Figure 65:

0 0 1 0 1 0 2 1 0 0 1 0 0 0 0 0 0 0 1 1 0 0 0 1 0 0 0 0 2 0 0 1 0 0 0 0 0 2 0 0

It contains 29 0's, 8 1's, and 3 2's. A Poisson distribution with mean λ has as the probability for n counts:

$$\Pr(n) = \mathrm{e}^{-\lambda}\frac{\lambda^n}{n!} \tag{4}$$

Setting $\lambda = 0.35$ as in this sample, we would get the average number of 0's, 1's, 2's for 40 samples as 28, 10, 2, respectively. Hence this sequence appears to be consistent with a Poisson distribution.

However we want to have a more rigid mathematical test. The 900 samples in one hour also form a more reliable basis for any testing.

We wish to select intervals for which we can be certain that we are at the background level and not within some true event. Our selection criteria are:

- the integration time must be 50 μs, since any other value occurs only when count rates are high;
- the distance from the Earth exceeds 7 $\mathrm{R_E}$, to avoid radiation belts;
- the distribution of counts within the interval be consistent with a Poisson distribution of fixed mean; this applies to each energy channel and detector individually;
- if all channels and detectors fail the tests, the output record is skipped; if only some fail, a record is output with those failed entries set to fill values.

It is the third point that is the most complicated and needs further explanation.

11.3 Poisson Testing

To test whether a set of integers is consistent with a single Poisson distribution we need some measure (a *statistic*) and we need to know its likely deviation from the ideal value. For example, in the sample above the mean value is 0.275 and the variance is $\langle n^2\rangle - \langle n\rangle = 0.424$, which is considerably higher than the expected value of 0.275. (Recall, the variance should also be λ.) Is this unreasonably high? For this small sample size, probably not, but we would like to quantify that statement.

We emphasize that we work here only with the raw counts, not count rates nor fluxes, since the Poisson statistics apply only to such counts. The counts background is then converted to rates or fluxes afterwards.

First let us explain the data model and define some terms. We have a set $\{x\}$ of N samples, such that each sample x_i is subject to a Poisson distribution, all with the same mean value λ.

$$\begin{aligned}\forall\, i,\ \langle x_i\rangle &= \sum_{n=0}^{\infty} n\Pr(n) = \sum_{n=0}^{\infty}\frac{n}{n!}\lambda^n\mathrm{e}^{-\lambda}\\ &= \lambda\end{aligned} \tag{5}$$

The *mean value* $\langle\rangle$ is a sum over all values of the distribution, valid for an infinite number of samples, while the *average of the sample values* is summed over the N values of the set $\{x\}$ and depends on the values in that

particular set.

$$\text{Sample average:} \quad \bar{x} = \frac{1}{N}\sum_{i=1}^{N} x_i \tag{6}$$

$$\text{and its mean value:} \quad \langle \bar{x} \rangle = \frac{1}{N}\sum_{i=1}^{N} \langle x_i \rangle = \lambda \tag{7}$$

The *statistic* $\bar{x}$ is thus an *unbiased estimator* for the population mean value λ.

Here are some other mean values that will be needed:

$$\begin{aligned} \langle x^2 \rangle &= \sum_{n=0}^{\infty} \frac{n^2}{n!} \lambda^n \mathrm{e}^{-\lambda} \\ &= \sum_{n=0}^{\infty} \frac{n(n-1)+n}{n!} \lambda^n \mathrm{e}^{-\lambda} \\ &= \lambda^2 \sum_{n=0}^{\infty} \frac{\lambda^n}{n!} \mathrm{e}^{-\lambda} + \lambda \sum_{n=0}^{\infty} \frac{\lambda^n}{n!} \mathrm{e}^{-\lambda} \\ &= \lambda^2 + \lambda \end{aligned} \tag{8}$$

from which we can derive the population variance $\langle x^2 \rangle - \langle x \rangle^2 = \lambda$. The *sample variance* on the other hand is

$$\mathrm{Var}(x) = \frac{1}{N}\sum_{i=1}^{N} x_i^2 - \bar{x}^2 \tag{9}$$

$$\begin{aligned} \text{with mean value} \quad \big\langle \mathrm{Var}(x) \big\rangle &= \frac{1}{N}\sum_{i=1}^{N} \langle x_i^2 \rangle - \frac{1}{N^2}\sum_{ij} \langle x_i x_j \rangle \\ &= \frac{1}{N}\sum_{i=1}^{N} \langle x_i^2 \rangle - \frac{1}{N^2}\sum_{i \neq j} \langle x_i \rangle \langle x_j \rangle - \frac{1}{N^2}\sum_{i} \langle x_i^2 \rangle \\ &= \lambda(\lambda+1) - \frac{N-1}{N}\lambda^2 - \frac{1}{N}\lambda(\lambda+1) \\ &= \frac{N-1}{N}\lambda \end{aligned} \tag{10}$$

The sample variance is a *biased estimator* of the true variance since its mean value is not exactly the same, but differs by the factor $(N-1)/N$.

Similarly mean values of other powers can be found as:

$$\langle x^3 \rangle = \langle x \rangle^3 + 3\langle x \rangle^2 + \langle x \rangle \tag{11}$$

$$\langle x^4 \rangle = \langle x \rangle^4 + 6\langle x \rangle^3 + 7\langle x \rangle^2 + \langle x \rangle \tag{12}$$

What we now use for the Poisson testing is the sample average as an estimator for λ and the sample variance $\times N/(N-1)$ and see how far it deviates from its expected value λ. To test the significance, we once more need

the variance of the sample variance, which can be derived with considerable algebra as

$$\begin{aligned} N(N-1)\ \mathrm{Var}(\mathrm{Var}(x)) = {} & (N-1)\ \langle x^4 \rangle \\ & -(N-3)\ \langle x^2 \rangle^2 \\ & +4(2N-3)\ \langle x^2 \rangle \langle x \rangle^2 \\ & -4(N-1)\ \langle x^3 \rangle \langle x \rangle \\ & -2(2N-3)\ \langle x \rangle^4 \end{aligned} \tag{13}$$

A value for $\mathrm{Var}(\mathrm{Var}(x))$ can then be found from equation 13, using equations 8, 11, 12 with the sample average $\bar{x}$ as an estimate for $\langle x \rangle$ (equation 7). The statistic that is then applied as a measure of the goodness of the Poisson assumption is then

$$\frac{\mathrm{Var}(x) - \bar{x}}{\sqrt{\mathrm{Var}(\mathrm{Var}(x))}}$$

the deviation of the sample variance from its (estimated) expected value in units of standard deviations.

The next task to is set significance levels for this deviation. For example, for a normal distribution, the 95% significance level is at 1.64, meaning 95% of the random values will have a deviation < 1.64 standard deviations from the mean value. How well can this be applied to a Poisson distribution?

We apply a Monte Carlo method to our Poisson model and statistic (5000 tests per value of λ) to determine the limit below which 95% of the deviations lie, with the following results:

- the limiting deviation is only weakly dependent on the sample size N;
- as λ increases, the limit $\to 1.64$, the value for a normal distribution; $\lambda > 5$ is already into this region (1.60);
- for $\lambda > 0.09$, we can fit the limiting deviation for 95% to a cubic equation in powers of $1/\lambda$;

  $$95\%\ \text{limit} = 1.64 - 0.299 \cdot \lambda^{-1} + 0.0403 \cdot \lambda^{-2} - 0.001922 \cdot \lambda^{-3}$$

  e.g. this gives for $\lambda = 0.1$ a value of 0.75 standard deviations;
- for $\lambda < 0.09$, use the above formula with $\lambda = 0.09$.

11.4 Application and Validity

As described earlier, the background product `IES_BG` is made up by taking one-hour intervals of single-spin (~4 s) *count* measurements meeting the criteria for integration time and distance from the Earth, and which also pass the Poisson test. That test consists of estimating the mean value and variance of the ~900 measurements and checking that the deviation of the variance from its expected value is within the 95% confidence limit.

There are two ways in which this test can go wrong:

false negatives: the 95% confidence limit means that even for a true Poisson distribution, 5% of these results will be wrongly rejected simply because of statistical variations; since we are looking for a *long-term* mininum in the background based on the hourly determinations, this is not so critical;

false positives: there is also a chance that non-Poisson distributions might be erroneously accepted; estimating how high this rate might be is not so easy since it requires a model for such distributions.

We do indeed see that at times of obvious activity in the electron fluxes, the Poisson test does fail, as expected. However to check the behaviour at more borderline situations, we set up Monte Carlo tests in which the 900 measurements are generated (randomly) with the mean value varying from λ to 2λ, and seeing how many are rejected by the test. The results are:

- for $\lambda = 5 \to 10$ and higher, the rejection rate is 100%;

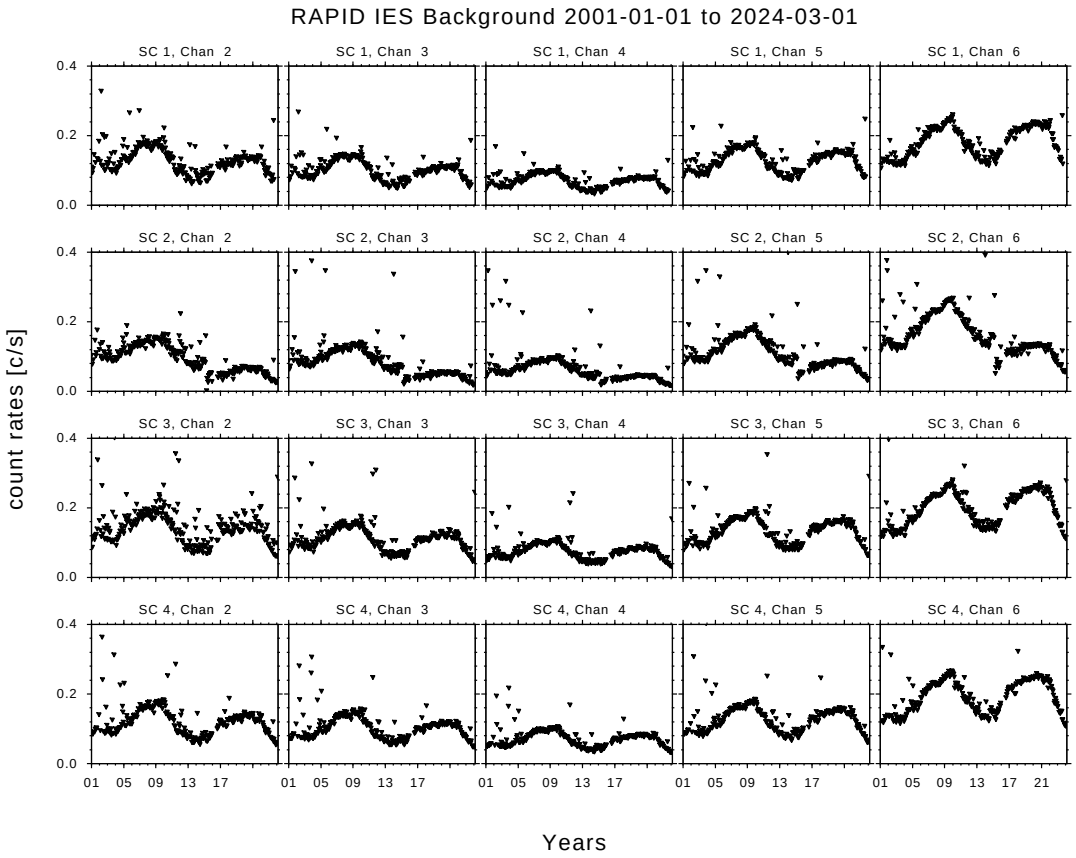

Figure 66: Minimum electron background rate per orbit over 23 years, for all 4 spacecraft and 5 energy channels. Channel 1 has been suppressed as described in the text. (The jump in the data on SC2 in 2015 is due to the partial failure in IES, Section 10).

- for $\lambda = 1 \rightarrow 2$, it is $\sim$32%;
- for $\lambda = 0.1 \rightarrow 0.2$, it is only about 6% (which is close to the 5% of false negatives inherent in the system).

This means that the rate of false positives is very low for a mixture of high λ, but at the realistic low values of $\sim$0.1, it is very high. This might be considered to be unsatisfying until one realizes

1. at such low values of λ, the relative error (standard deviation to mean value) is very large ($\gg$ 1), and therefore deviations of a factor of 2 are quite likely to be accepted;
2. Such a low average over such a long time is most likely background anyway;
3. what could still lead to false positives would be a very steady flux at high rates, over a long time, from something like solar events, which can continue for days.

We conclude that this Poisson test is a reasonable method to detect times of steady background, and to eliminate most other true events.

11.5 Long-Term Analysis

To investigate the long-term variation, if any, in the electron background, we take all the hourly measurements for all 4 spacecraft over the entire Mission, from 2001 to (currently) the middle of 2023. We then proceed as follows:

1. For each single orbit (∼2.5 days) we take the minimum background for each detector and energy channel, which we then plot as a matrix, one for each spacecraft.
2. We establish from this that, apart from other known interferences such as the solar noise (Section 5.1.4) and pedestal noise (Section 5.1.3), the 9 detectors all show the same behaviour.
3. For this reason, we combine all the 9 detectors (without those suspect ones) to make up an omnidirectional background.
4. We also remove energy channel 1, since this suffers from many redefinitions of the lower threshold, and so is not consistent over all detectors, spacecraft, and time.
5. The final results are now plotted in Figure 66.

Note that in Figure 66 we are plotting rates, not raw counts. The rates range from $\sim 0.1\ s^{-1}$ to $\sim 0.25\ s^{-1}$, or counts per spin of 0.4–1. Note also the differences between channels does not reflect a possible energy dependence, since these are total rates over the whole channel width; channel 6 is by far the widest and so it is not surprising that its rates are the highest.

The time variation over the 22 years is reminiscent of the 11-year solar cycle, and in fact, this profile is very similar to ones observed on other missions [e.g., on Cassini by *Roussos et al.*, 2011], which were attributed to intergalactic cosmic rays, modulated by the solar activity.

We thus conclude, that our electron background is similarly solar-cycle modulated cosmic rays.

11.6 Non-Cosmic-Ray Background

In spite of what is stated above, there are times when there are other types of background fluxes present. The algorithm for determining the background only checks for long-term (∼1 hour) stability in the sense that any variations within this interval are consistent with only Poisson noise.

Figure 67 demonstrates this for a period of regular, low cosmic ray background. The one-hour background data are plotted as red stars over the corresponding electron fluxes. When the flux variation is not steady during that hour, then no background point is found, and there is a gap in the background data. Real events stand out over the steady background.

However, a steady flux level can also exist during long, slowly changing events, such as for the coronal mass ejection (CME) shown in Figure 68. Here the red background points follow increasing flux levels, since they remain constant in the Poisson sense. Short term events are still visible, standing out from this high-level background.

> **Conclusion:** The background product indicates the *current* steady (scale of hours) background level, in order to study shorter-term events that sit on top of it. It is normally from intergalactic cosmic rays, but can be swamped by other steady backgrounds, such as from solar events.

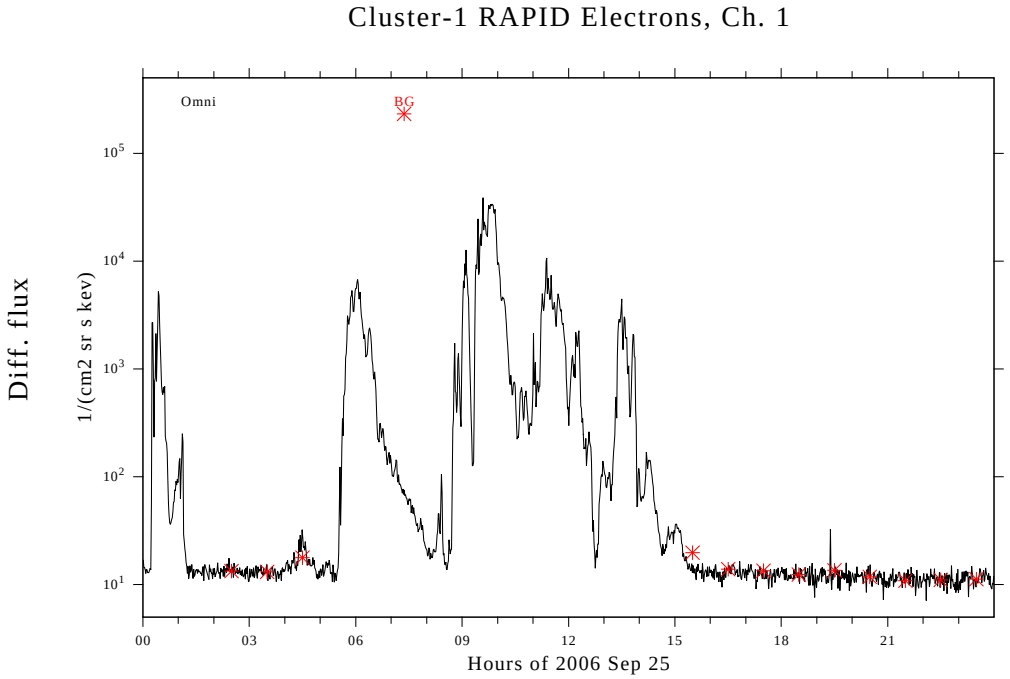

Figure 67: Plot of omnidirectional electon fluxes in energy channel 1 (black line) together with corresponding one-hour background values (red stars). Background values only exist when the variations over the one hour are purely statistical (Poisson). Therefore they do not exist during any "events" that might occur.

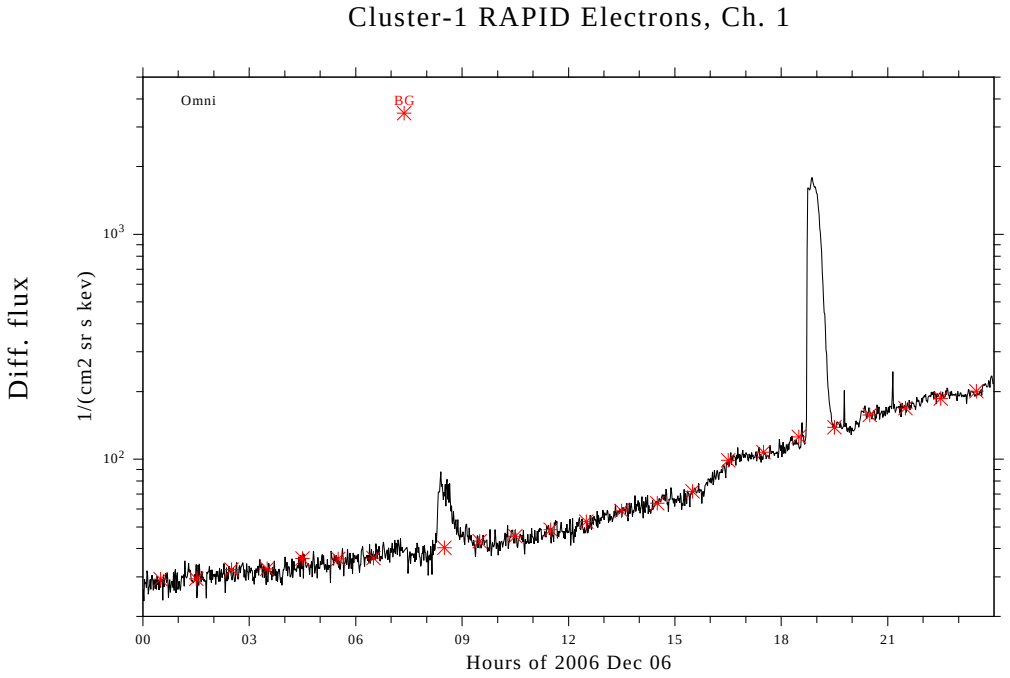

Figure 68: The same plot as in Figure 67 but for a time during a CME interval, which enhances the long-term stable background. Any short term events still appear, but do not contribute to the background product.

12 IES Contamination in the Radiation Belts

The RAPID/IES data can be contaminated by energetic protons and electrons. This is especially worrying issue in the radiation belts. An assessment of a possible contamination has been done by *Kronberg et al.* [2016]. They assess the level of distortion of energetic electron spectra from the RAPID/IES detector, determining the efficiency of its shielding. The assessment is based on the analysis of experimental data (from the National Institute of Standards and Technology and the Stopping and Range of Ions in Matter program) and a radiation transport code (Geant4). In simulations, the incident particle energy distribution of the AE9/AP9 radiation belt models was used. The results of the simulations which present the contamination percentage of the RAPID/IES energy channels at different L* are shown in Figure 69 and their values can be found in Table 3.

Applying the simulation results, the RAPID/IES data can be corrected using the following methods:

(1) The experimental data show that the RAPID/IES at all energy channels (40–400 keV) are strongly contaminated by protons of ($\simeq$230 to 630 keV and >600 MeV) at 3$\leq$L$^\star\leq$4. Therefore, in case of simultaneous availability of electron intensities and proton intensities in the range from $\simeq$230 to 630 keV, we recommend to subtract the proton intensities from the electron intensities as described in section 5, equation (3) in *Kronberg et al.* [2016]. In case of the IES energy channel 6 one can simply subtract the proton intensities at $\simeq$230 to 630 keV from the electron data for liberating data from proton contamination.

(2) In case that proton intensities in the aforementioned range are not available, we recommend to use equation 14 to remove the proton and electron contaminations:

$$I_{\mathrm{e,\,clean}} = I_{\mathrm{e}} - I_{\mathrm{e}}C, \tag{14}$$

where C is the contamination percentage taken from Table 3).

In summary, the Roederer L-values (for quiet magnetic field), $L^\star$, and energy channels that should be used with caution are identified: at 3$\leq$L$^\star\leq$4 all energy channels (40–400 keV) are contaminated by protons ($\simeq$230 to 630 keV

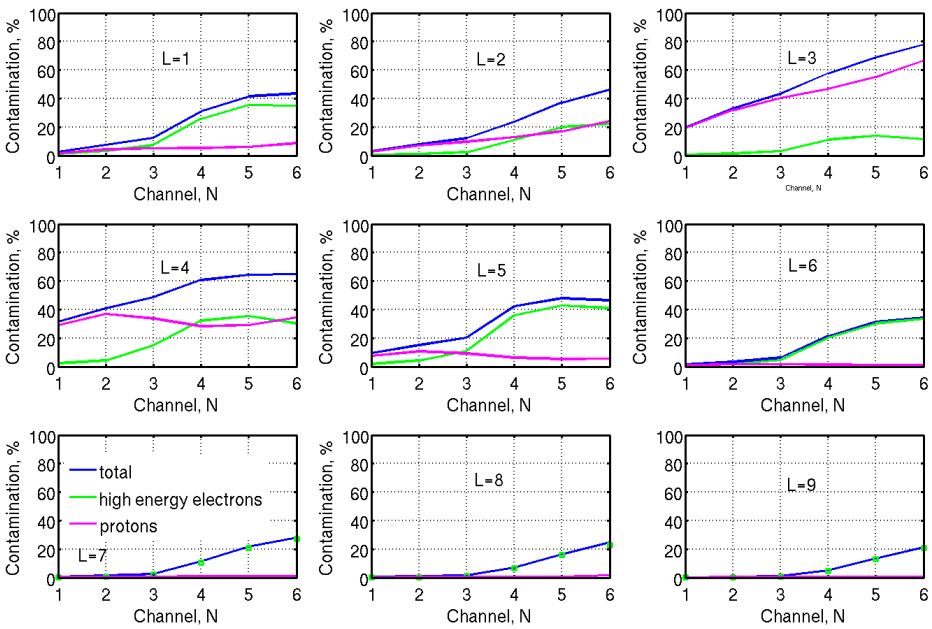

Figure 69: IES data contamination in the electron and proton radiation belts at different $L^\star$-shells, for different energy channels and for the solar maximum. The percentage of the contamination by protons, high-energy electrons and the sum of those is denoted by magenta, green and blue colors respectively.

and >600 MeV); at L* $\simeq$1, 4–6 the energy channels at 95–400 keV are contaminated by high energy electrons (>400 keV). However, choosing carefully the energy channels and the L shells according to the results of Geant4 simulations (Table 2), one can still use the IES radiation belt and ring current observations. Or the data can be corrected using the methods (1) and (2) proposed above.

Table 3: Contamination (%) of the IES detector in the Earth's radiation belts for the solar maximum.

	Contamination, %					
Nr. Channel	1	2	3	4	5	6
			L*=1			
electrons	1.03	3.28	7.27	25.85	35.43	34.89
protons	1.6	4.23	5.02	5.2	6.04	8.62
total	2.63	7.51	12.29	31.06	41.47	43.51
			L*=2			
electrons	0.32	1.02	2.35	10.8	20.06	22.2
protons	2.55	6.93	9.68	12.88	17.04	24.33
total	2.87	7.95	12.04	23.68	37.1	46.53
			L*=3			
electrons	0.62	1.23	2.97	11.04	13.83	11.28
protons	18.97	31.73	40.21	46.6	54.9	66.65
total	19.59	32.96	43.18	57.64	68.73	77.93
			L*=4			
electrons	2.38	4.31	14.92	32.25	35.42	30.3
protons	29.03	36.77	33.78	28.41	28.96	34.49
total	31.41	41.08	48.7	60.66	64.38	64.79
			L*=5			
electrons	1.76	4.32	11.02	35.96	42.65	40.94
protons	7.51	10.77	9.18	6.2	5.29	5.47
total	9.27	15.09	20.2	42.16	47.94	46.41
			L*=6			
electrons	0.5	1.66	4.65	20.19	30.33	33.41
protons	0.83	1.58	1.5	1.26	1.12	1.14
total	1.33	3.24	6.15	21.44	31.45	34.55
			L*=7			
electrons	0.18	0.69	1.99	10.59	21.01	27.01
protons	0.26	0.61	0.69	0.75	0.8	0.93
total	0.44	1.3	2.68	11.34	21.81	27.94
			L*=8			
electrons	0.09	0.38	1.09	6.45	15.79	22.93
protons	0.17	0.42	0.52	0.62	0.73	1.64
total	0.26	0.8	1.61	7.07	16.53	24.57
			L*=9			
electrons	0.06	0.25	0.72	4.48	12.8	20.67
protons	0.11	0.27	0.34	0.42	0.51	0.63
total	0.17	0.52	1.06	4.9	13.31	21.3

13 Accessing Data for Heavier Ions

The regular ion products, omnidirectional and 3-D, deliver rates and fluxes for three ion sets: H, He, and CNO. However, RAPID is capable of detecting ions of higher masses as well. This is illustrated in Figure 12 on page 24 and Figure 70 below, where in addition to the regular species-channels areas, there are also areas provided for SiFe in the Energy–TOF space. The counts in these additional areas can only be accessed through the Direct Events (DE) and ion matrix (MTRX) products. Their usage is not straight-forward and they can only be properly interpreted with considerable knowledge of the RAPID instrument.

13.1 Direct Events (DE)

The Direct Events product is described in Appendix B of RAP-ICD. For a limited number of ion events per spin (20 in NM, 106 in BM), the high-resolution energy and time-of-flight information is given, along with directional information (head, sub-head, spin sector).

For the CSA product, additional derived data are given: the species (H, He, CNO, SiFe) and energy channel (1–8) as determined by the on-board classification algorithm that is used for sorting the ions in the omnidirectional and 3-D productions. These areas in Energy–TOF space are shown in Figure 70. For the Direct Event product, this algorithm is applied during processing, on the ground.

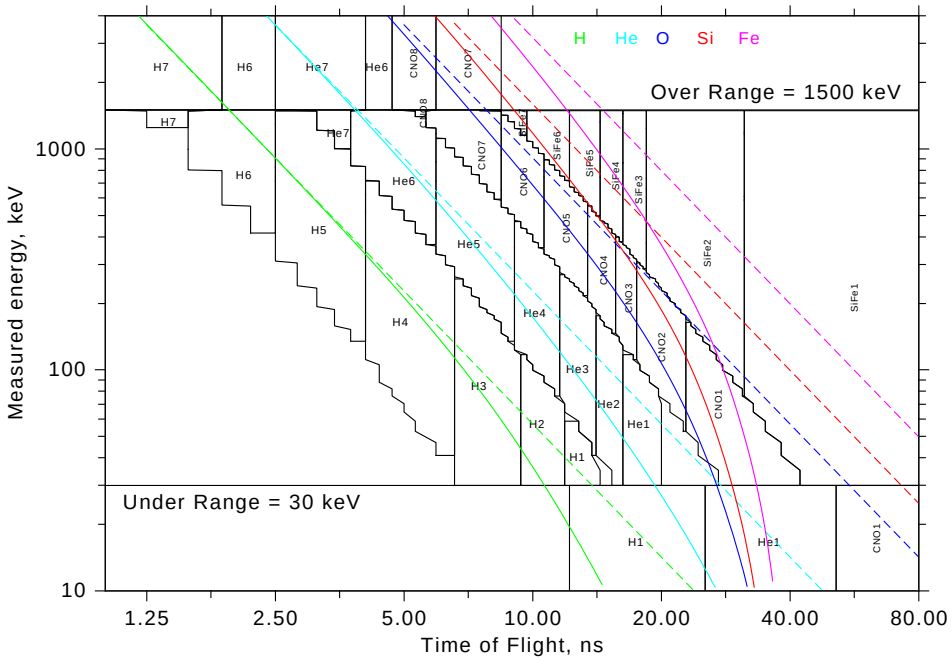

Figure 70: Direct Event space, measured energy versus time-of-flight. This is the same as Figure 12, with the addition of coloured lines showing the locus of 5 ions species, as calculated with the SRIM software using the actual foil and detector characteristics for RAPID, for an incidence angle of 15°, the central value. The dashed lines are the results without energy losses in the detectors.

The energy–TOF space is an array of 256×256 elements, the energy ranging from 0–1500 keV, the TOF from 0–80 ns, both scales being linear with their respective index of 0–255.

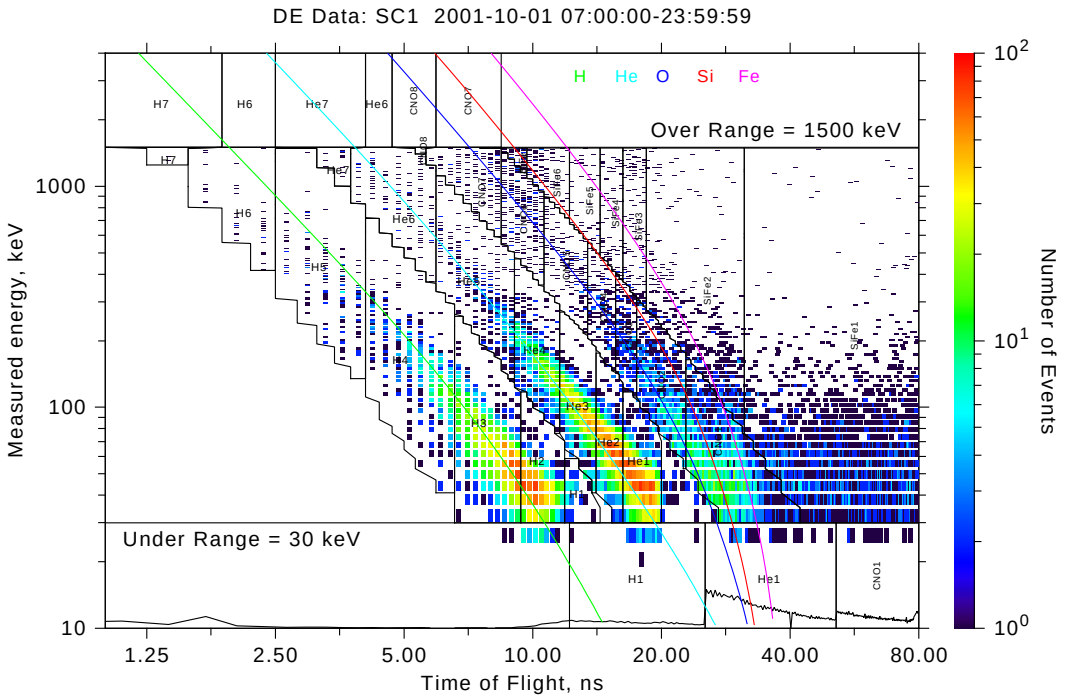

Figure 71: Direct Event space filled with data from 2001-10-01, during a very disturbed interval. Here one sees how well the H, He, and CNO fall in their expected areas, whereas other events line up reasonably well with the (SRIM) Fe line. There are even indications at higher energies of the possible presence of Si.

In principle, every point in the energy–TOF space corresponds to a given mass through the equation

$$\begin{aligned} E_{\text{tof}} &= \frac{1}{2} m v^2 \\ &= \frac{1}{2} m \left(\frac{L}{T \cos\theta} \right)^2 \end{aligned} \tag{15}$$

where L is the length over which the time-of-flight T is measured, and θ the angle of incidence, from 0° to 30°. Thus in the log-log plot of Figure 70 the locus of constant mass m should be a straight line of slope -2, and m determines the intercepts. The dashed lines in the figure are such ideal curves.

However, the E_{tof} above is not the measured energy in the Figure, but the energy the particle has as it traverses the TOF distance L. The measured energy is less, due to losses in the detector, in the dead layer and nuclear defect. When these losses are considered, the constant mass lines become curves, deviating most strongly at lower energies. These deviations have been calculated using the algorithms of the *Stopping and Range of Ions in Matter*, SRIM [*Ziegler et al.*, 2015], with the actual foil and detector characterists of RAPID. These are the solid coloured curves in Figure 70.

The on-board classification algorithm makes use of preprogrammed E–TOF curves to define the species-channel areas in Figure 70. The coloured SRIM curves match reasonably well with these for H, He, and O, but for Si and Fe, they are badly off, especially at lower energies.

In order to use the Direct Event data to investigate the behaviour of the higher mass ions, one cannot rely on the on-board assignments, but must use the SRIM curves to properly identify the masses. This has been successfully carried out by *Haaland et al.* [2020] in a long-term study to search for Fe in the magnetosphere.

Figure 71 shows DE data in the energy–TOF space for a particularly active time early in the Mission. It shows the

H, He, CNO events, well separated, lining up in the expected locations, whereas there are other events following the SRIM curve for Fe, even at low energies. This is the evidence that the Fe measurements are indeed credible.

This figure even hints that there might be a Si component in the ions at higher energies. More on this in Section 13.2.

It is clear that the mass resolution is rather broad. The spread in the ion distributions is due not only to noise in the electronics, but also to a large part from the range of incidence angles (±30°) in each head and the corresponding cosine factor for the TOF distance (Eqn. 15). Therefore we prefer to speak of "Fe-like" and "Si-like" particles.

The Direct Events product, essentially a diagnostic tool, can be use to access data for higher mass particles, but only with better understanding of the RAPID instrument.

13.2 The MTRX and RMTRX Products

There is another product in the raw RAPID data that can access the higher mass species. This is called the ion matrix MTRX product, and is a transformed version of the Direct Event space. But unlike the DE, which contains full information on a few individual events, the MTRX contains count rates in an array of 32 masses by 64 energy-per-mass bins. There is no directional information at all; the accumulation time is 64 spins.

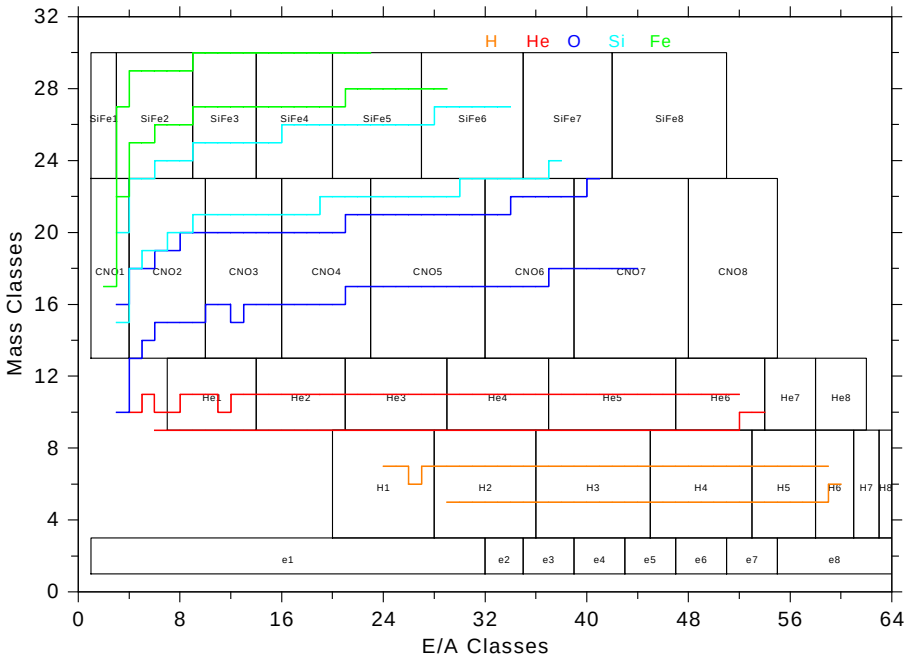

Figure 72: The MTRX space, 32 mass values versus 64 energy per mass bins, as converted from DE space using the preprogrammed E–TOF curves. If these were correct, then each mass would be a horizontal line. The species-channel areas of Figure 70 are rendered here as well; in fact, they are actually defined in this space. The coloured lines are the transformed SRIM E–TOF curves (for incidence angles of 0° and 30° for each species) showing again how they deviate from the preprogrammed values for higher masses at low energies.

The conversion from DE to MTRX space relies on the preprogrammed internal E–TOF curves for masses in question. The original intention was that each mass would map to a horizontal line, i.e., to a single "mass" index number. Since these curves are clearly in error for higher masses (the SRIM curves in Figure 70), the MTRX space cannot be correct at higher masses. Figure 72 illustrates this space, including the preprogrammed species-channels areas (which are in fact defined in MTRX space) and the converted SRIM curves for 5 species. (These species-channel areas play no role for the output of MTRX, and are only included here for illustration.)

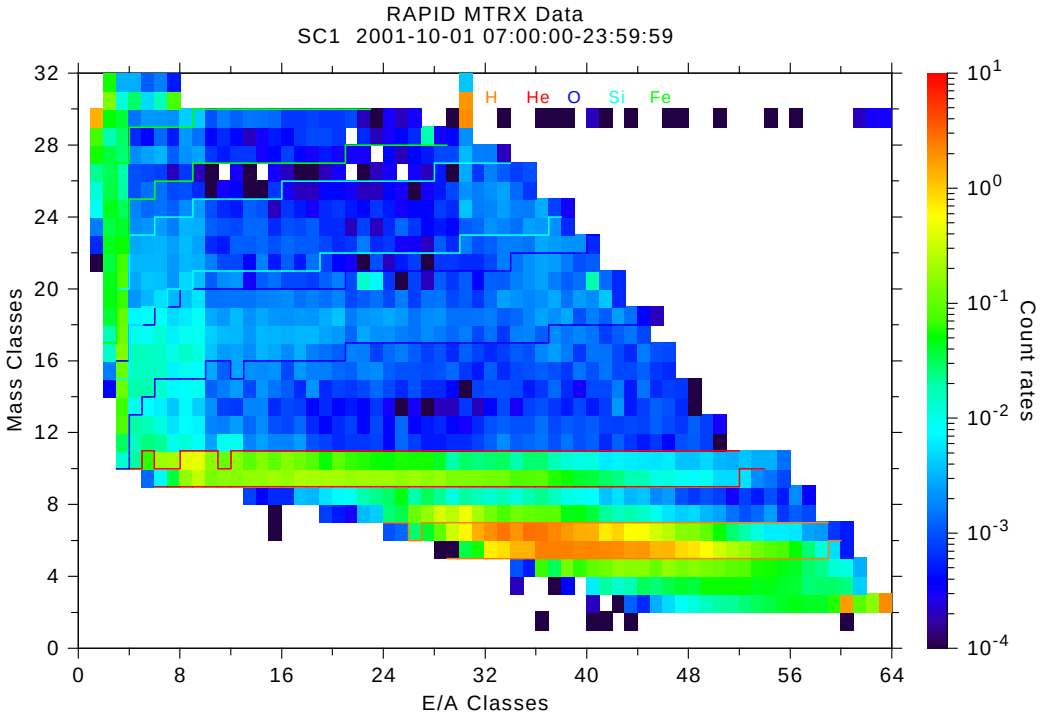

Figure 73: The MTRX space filled with data from 2001-10-01, the same interval as in Figure 71. The SRIM curves for the limiting incidence angles of 0° and 30° are also shown.

This product was not originally delivered to CSA, as it seemed to offer nothing new for the H, He, CNO particles, has a poor time resolution (64 spins ≈ 256 s, with a readout time of 256 spins (NM) or 64 spins (BM)). However, with the success of the Fe investigation by *Haaland et al.* [2020] with the DE data, it became clear that MTRX could provide even better data for this work. The poor time resolution and lack of directional information are not so important for such a long-term study. And it has the advantage over DE, that all events are counted, and there is no priority scheme to blur the relative intensities between the species or to distort the spectra. For this reason, it is now included as a CSA RAPID product.

Figure 73 shows the MTRX data from the same time interval as in Figure 71. In this case, the "hints" of a Si component are far more pronounced, and could be called "indications". This has been investigated more thoroughly in a follow-up paper by *Haaland et al.* [2021], using the RMTRX data described below.

It is difficult to interpret the masses correctly without specialist knowledge, and it cannot be (easily) calibrated into fluxes.

In order to overcome this problem of mass interpretation, we have produced an additional derived product: RMTRX, or Reduced Matrix. This is intended to be easier for the general user, the masses and energies are delivered directly. It is the same as MTRX except that the 32 × 64 array becomes 5 × 8, with 5 masses (H, He, O, Si, Fe) and 8 energy channels, which are now species dependent. These array elements are sums of the count rates over selected areas in MTRX space, shown in Figure 74. This is effectively a redefinition of the species-channel areas of Figure 72.

Note that the species channels have been expanded to fill any gaps between them, something most noticeable for oxygen. This allows for any spreading of the data beyond the expected range of incidence angles and for possible shifts downwards as the solid state detectors age.

The RMTRX numbers are pure sums over the corresponding areas, with no normalization to adjust for the sizes

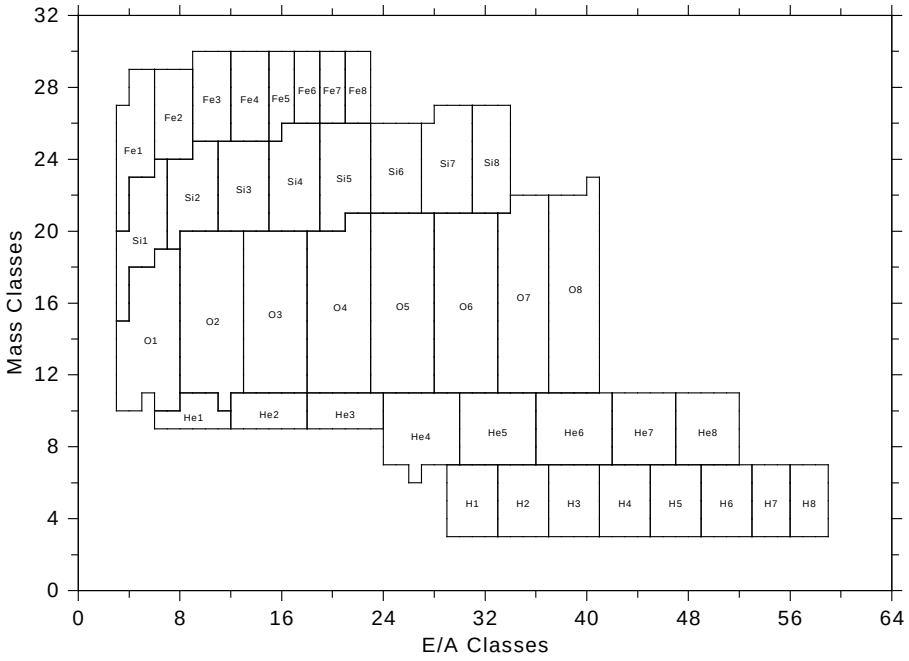

Figure 74: The MTRX space showing the 5×8 areas of the RMTRX product.

of the areas. Conversion into flux is tricky and has not been done.

Using the data from the SRIM curves, we can determine the initial energy values for these energy channels, i.e., the energy the particle had before entering the detection system, before going through the start foil. These are listed in Table 4. (Note: these are different from the regular channel values as in Table 1 of RAP-UG, as they are defined differently; in particular, they skip the underrange area that goes into the regular channel 1.)

The MTRX and RMTRX products for the whole Mission have been added to CSA in 2020, as count rates only.

It is this RMTRX product that is used by [*Haaland et al.*, 2021] to investigate the presence of Fe and Si in the solar wind and magnetosphere.

Table 4: Initial (external) energies for the RMTRX channels
Lower levels in keV

Channel	H	He	O	Si	Fe
1	74	101	243	401	709
2	86	137	408	648	1080
3	104	166	515	818	1344
4	130	206	611	934	1524
5	174	266	743	1082	1689
6	253	362	929	1272	1817
7	423	535	1203	1520	1961
8	718	817	1526	1854	2126
Upper	1143	1279	1866	2066	2218

14 Summary

The result of the cross-calibration activities of RAPID with PEACE and CIS in Section 6 show that those instruments are well cross-calibrated and do not need special corrections apart from a possible adjustment to the 1st energy channel. Still at least for CIS/CODIF and RAPID/IIMS the data starting from 2006 have to be cross-checked, as at both instruments the TOF efficiencies become worse with time.

For Cluster/RAPID science data users another important fact will be of interest. To understand the relationship between count rates and fluxes a few notes have to be taken on factors and calculation procedures, being involved in the data processing chain performed by the RAPID software.

To this end, it is important to pay attention to the standard deviations of all the RAPID measurements in order to check their statistical significance. These standard deviations are delivered as part of every RAPID data product.

Appendices

A Calculation of Fluxes from Count Rates

Here an overview is presented for the derivation of the particle fluxes from the measured count rates.

A.1 Geometry Factor

Consider a particle of energy E and incoming direction Ω, striking the detector surface at some point S. The probability that it successfully navigates through the entrance aperture and collimators to reach the detector at that point is $\Pr(E, \Omega, S)$, which is either 1 or 0. The integral of this probability over the field-of-view $\Delta\Omega$ and detector surface ΔS is the *geometry factor* (GF):

$$G(E) = \int_{\Delta\Omega} d\Omega \int_{\Delta S} dS \ \Pr(E, \Omega, S) \tag{16}$$

The geometry factor $G(E)$ has units of $\mathrm{cm}^2 \cdot \mathrm{sr}$; it essentially describes how much of the detector surface can be 'seen' externally, summed over all input directions.

In the case of RAPID, the particle paths do not contain electric and magnetic fields, hence the GF is independent of energy and species.[2] Calculations for one SCENIC sensor yield

$$G = 8.85 \times 10^{-3}\ \mathrm{cm}^2 \cdot \mathrm{sr} \tag{17}$$

or $2.21 \times 10^{-3}\ \mathrm{cm}^2 \cdot \mathrm{sr}$ for one polar segment of 15°.

The rate of particles of energy E striking the detector surface can now be written as

$$\begin{aligned} \mathcal{R}(E) &= \int_{\Delta\Omega} d\Omega \int_{\Delta S} dS \ j(E, \Omega, S) \cdot \Pr(E, \Omega, S) \\ &= G(E) \cdot \bar{j}(E) \end{aligned} \tag{18}$$

where

$$\bar{j}(E) = \frac{1}{G(E)} \int_{\Delta\Omega} d\Omega \int_{\Delta S} dS \ j(E, \Omega, S) \cdot \Pr(E, \Omega, S) \tag{19}$$

Note that $\bar{j}$ is the average of j over the field-of-view and detector area, weighted by the geometry factor.

A.2 Detector Efficiency

The probability that a particle is detected and measured once it strikes the detecting surface is described by the *detector efficiency* $\epsilon(E)$, which is a function of particle energy and species, but not of direction and position on the surface.

The efficiency has been measured by ion beam experiments on the channel plate detectors, and can be fitted to an exponential:

$$\begin{aligned} \epsilon &\approx a \exp(bE) + c \quad \text{for } E < E_{\max} \\ &\approx \epsilon_{\max} \qquad\qquad\quad E > E_{\max} \end{aligned} \tag{20}$$

The coefficients a, b, c, as well as $E_{\max}$ and $\epsilon_{\max}$ depend on particle type. The maximum $\epsilon_{\max} \sim 0.1$–0.2.

[2] This statement does not apply when the deflection voltage is on to sweep ions out of the detection region.

A.3 Conversion Factor for Particle Flux

We now derive the *conversion factor* (CF) between particle flux and measured count rates.

The number of counts recorded per unit time is the integral over the selected energy range of the rate $\mathcal{R}$ (equation 18) that particles strike the detector times the probability ϵ that they are measured:

$$\int_{\Delta\Omega} d\Omega \int_{\Delta S} dS \ \Pr(E, \Omega, S)\, \epsilon(E) \cdot j(E, \Omega, S) = \int_{E_1}^{E_2} dE \ G(E)\, \epsilon(E) \cdot \bar{j}(E) \tag{21}$$

We now want to find an approximation for the particle flux knowing the count rate $\mathcal{N}$. The problem is to invert equation (21). In fact, what we really obtain is only the *integral flux* J:

$$J(E_1, E_2) = \int_{E_1}^{E_2} dE \ \bar{j}(E) \tag{22}$$

Let us define the *weighted mean conversion factor* for this energy range as

$$\overline{CF} = \frac{\int dE \ w(E)\, G(E)\, \epsilon(E)}{\int dE \ w(E)} \tag{23}$$

$$\approx \frac{1}{\Delta E} \int_{E_1}^{E_2} dE \ G(E)\, \epsilon(E) \tag{24}$$

If the weighting function $w(E)$ were to be proportional to $\bar{j}(E)$, then (23) yields

$$\overline{CF} \int_{E_1}^{E_2} dE \ \bar{j}(E) = \int_{E_1}^{E_2} dE \ \bar{j}(E) \cdot G(E)\, \epsilon(E)$$

$$\overline{CF} \ J(E_1, E_2) = \mathcal{N}(E_1, E_2) \tag{25}$$

or

$$J(E_1, E_2) = \mathcal{N}(E_1, E_2) / \overline{CF}(E_1, E_2) \tag{26}$$

$\overline{CF}$ is thus the conversion factor between the integral flux in one energy channel and the count rate in that channel.

From equation (23) we see that the conversion factor at a given energy is $G(E)\,\epsilon(E)$ and that $\overline{CF}$ is the mean of this factor over the energy channel. Since $G(E)\,\epsilon(E)$ varies only slightly with energy (except at low energies), the mean value should not differ too much from any value within the range.

Ideally the weighting function $w(E)$ in equation (23) should be of the same shape as $\bar{j}(E)$; in reality we take it to be constant. This assumption is legitimate to the extent that $G(E)\,\epsilon(E)$ is only weakly dependent on energy.

The averaged CF *does not depend directly on the* ΔE *of the energy channel*. One often quotes a *differential conversion factor*, in units of $\mathrm{cm}^2 \cdot \mathrm{sr} \cdot \mathrm{keV}$ which is really $\overline{CF} \times \Delta E$. In this paper, we deal entirely with the 'integral' CF.

A.4 Conversion to Differential Flux

One really would like to have an estimate for the differential flux $\bar{j}$. This is usually achieved with

$$\bar{j} = J(E_1, E_2)/\Delta E \tag{27}$$

but this produces only the average differential flux within the energy channel, and it is not at all clear to which energy it should be assigned. A better method is to try to fit the observed counts, or integral fluxes, to a spectrum model.

Incidently, by taking $w(E)$ in equation (23) as constant, the flux in equation (27) is really an average of the differential flux $\bar{j}(E)$ over the energy channel, weighted by the conversion factor $G(E)\,\epsilon(E)$.

A.5 Calculation of Omnidirectional Flux

For each of the three ion species, we will be given the omnidirectional counts for 8 energy channels. For each energy channel, and species, we will have the effective omnidirectional CF, $\Sigma\overline{CF}$, the sum of the CF's over the polar segments.

We also allow for a possible background count rate for each energy channel and direction. The background rates must also be summed over all polar segments to produce the rate in the pseudo omnidirectional detector, ΣBG.

The omnidirectional flux in energy channel n is thus:

$$\boxed{J_n = \frac{C_n/T - \Sigma BG}{\Sigma\overline{CF}}} \tag{28}$$

where C_n is the number of counts in energy channel n accumulated over time T (one spin for protons, 4 spins for the others); C_n/T corresponds to $\mathcal{N}$ of equations (21) and (26).

Note: it was originally thought that the background would be isotropic penetrating particles or electronic noise. It now turns out that for the ions, there is solar contamination, predominantly in the sun sector. It is also a different rate in serial and parallel mode, since in serial only one third of the sector is "active", and this third misses the sun. In the latest version of the calibration data, no background removal is applied, since this can lead to strange irreversible results; it is better to let the user work on this himself. The only exception is for some large solar contamination in the IES head 1 on SC3, which is very strongly dependent on the solar aspect angle.

B Phase Space Density Conversion

All the products delivered to CSA by the RAPID Team are in differential particle flux units. Because of RAPID's wide energy bins, a conversion to phase space density (as commonly used by lower energy spectrometers) is not feasible, since the effective energy of each bin depends on the spectrum. Nevertheless, we give here an outline of how such a conversion is to be done.

The differential flux of particles with velocity $\bar{v}$ is given by

$$\bar{j}(E, \Omega)\, dE\, d\Omega = f(\bar{v})\, v^3\, dv\, d\Omega \tag{29}$$

where $f(\bar{v})\, v^2\, dv\, d\Omega$ is the number of particles per unit volume with velocity between (v_x, v_y, v_z) and $(v_x + dv_x, v_y + dv_y, v_z + dv_z)$. From the equation (29) using relationship $dE = mv\, dv$ we get the standard relation between differential flux and phase space density (non-relativistical case)

$$\bar{j} = \frac{2E}{m^2}\, f(\bar{v}) \tag{30}$$

The phase space density can be written in units of $\mathrm{km}^{-6}\mathrm{s}^3$ as

$$f = m^2 \frac{\bar{j}}{E_{\mathrm{eff}}} \cdot 0.53707 \tag{31}$$

where m is the particle mass in atomic mass units, $\bar{j}$ is recorded in $\mathrm{cm}^{-2}\mathrm{s}^{-1}\mathrm{sr}^{-1}\mathrm{keV}^{-1}$ and E_{eff} is the effective energy of the energy channel in keV.

For the relativistic case, we must use the total energy $E_T = E_0 + E$, where E_0 is the rest energy and E the measured kinetic energy. Applying the relativistic formula

$$E_T = \frac{E_0}{\sqrt{1 - v^2/c^2}} \tag{32}$$

to equation 29, we get the equivalent of equation 30 to be

$$\bar{j} = f(\bar{v})\ \frac{E_0^2\, c^4}{E_T^3}\,[1 - (E_0/E_T)^2] \tag{33}$$

The equavalent of equation 31 in the same units, becomes:

$$f(\bar{v}) = E_T \left(\frac{E_T}{E_0}\right)^2 \frac{\bar{j}}{1 - (E_0/E_T)^2} \cdot 1.2379 \times 10^{-12} \tag{34}$$

B.1 Calculation of the Effective Energy for the Energy Channels

The differential flux is delivered as the intergrated flux divided by ΔE. The problem is to what energy does it correspond? Here is a simple analysis for a power law distribution

$$J = \int_{E_1}^{E_2} A \cdot E^{-\gamma}\, dE = \frac{A}{\gamma - 1}(E_1^{-\gamma+1} - E_2^{-\gamma+1}) \tag{35}$$

where E_1 and E_2 are the energy channel thresholds, γ is a spectral index and A is a normalization.

Let $E_\mathrm{m} = (E_2 + E_1)/2$, $\Delta = (E_2 - E_1)/2$ and we denote as

$$\delta = \frac{\Delta}{E_\mathrm{m}} \tag{36}$$

then equation (35) can be transformed to

$$\frac{J}{E_2 - E_1} = \frac{A}{\gamma - 1} \cdot \frac{(1-\delta)^{-\gamma+1} - (1+\delta)^{-\gamma+1}}{2\delta} E_\mathrm{m}^{-\gamma} \equiv A \cdot E_\mathrm{eff}^{-\gamma} \tag{37}$$

where E_eff is the energy at which the spectrum with given A and γ has the differential flux equal $J/\Delta E$. Equation (37) leads to

$$\begin{aligned}\left(\frac{E_\mathrm{eff}}{E_\mathrm{m}}\right)^{-\gamma} &= \frac{(1-\delta)^{-\gamma+1} - (1+\delta)^{-\gamma+1}}{2\delta(\gamma - 1)} \\ &\simeq 1 + \frac{\gamma(\gamma+1)\delta^2}{6} + \ldots \\ \frac{E_\mathrm{eff}}{E_\mathrm{m}} &\simeq 1 - \frac{(\gamma+1)\delta^2}{6} + \ldots \end{aligned} \tag{38}$$

The spectral index γ can be estimated by using fluxes for two adjacent energy channels and their effective energies

$$\gamma = \frac{\ln(j_1/j_2)}{\ln(E_{\mathrm{eff}_2}/E_{\mathrm{eff}_1})} \tag{39}$$

This expression is derived from the definition of the differential flux $j = A \cdot E^\gamma$.

Some upper energy channel thresholds are double or more the lower one. In this case where $E_2 = 2E_1$, $\Delta = E_1/2$, $E_\mathrm{m} = 1.5E_1$ we get $\delta = 1/3$. Requiring $(\gamma+1)\delta^2/6 < 0.1$ (i.e. 10 % accuracy in E_eff) we obtain $\gamma < 5.6$ for $\delta = 1/3$. Thus the mean energy, E_m is a good first approximation of the effective energy, E_eff, i. e. $E_\mathrm{eff} = E_\mathrm{m}$.

Chan	E_g	$f/\bar{j}$	E_g	$f/\bar{j}$
	Protons		Helium	
1	42.23	1.271×10^{-2}	64.18	1.338×10^{-1}
2	83.32	6.445×10^{-3}	154.0	5.576×10^{-2}
3	121.3	4.426×10^{-3}	201.2	4.269×10^{-2}
4	244.3	2.197×10^{-3}	287.2	2.991×10^{-2}
5	599.8	8.953×10^{-4}	508.6	1.689×10^{-2}
6	1340.	4.005×10^{-4}	1100.	7.806×10^{-3}
7	2748.	1.954×10^{-4}	2533.	3.392×10^{-3}
8	4007.	1.340×10^{-4}	3799.	2.261×10^{-3}
	Oxygen		Electrons	
1	151.6	9.066×10^{-1}	44.49	5.284×10^{-9}
2	337.0	4.079×10^{-1}	58.64	4.487×10^{-9}
3	454.0	3.028×10^{-1}	80.22	3.872×10^{-9}
4	563.6	2.439×10^{-1}	109.7	3.517×10^{-9}
5	777.7	1.767×10^{-1}	149.7	3.402×10^{-9}
6	1157.	1.187×10^{-1}	207.2	3.556×10^{-9}
7	1931.	7.117×10^{-2}	286.6	4.080×10^{-9}
8	3267.	4.207×10^{-2}	369.8	4.883×10^{-9}

Table 5: Conversion factors from differential flux ($cm^{-2}s^{-1}sr^{-1}keV^{-1}$) to phase space density ($km^{-6}s^3$).

Therefore a first guess of γ can be obtained from equation (39) using $E_{\text{eff}} = E_{\text{m}}$, and then we can get a better estimate of E_{eff} from equation (38) and iterate again.

Example: We take the realistic energy thresholds $E_1 = 27.7\,\text{keV}$, $E_2 = 64.4\,\text{keV}$ $E_3 = 75.3\,\text{keV}$ and $E_4 = 92.2\,\text{keV}$ and the differential fluxes $j_1 = 7.58 \times 10^4\,\text{cm}^{-2}\text{s}^{-1}\text{sr}^{-1}\text{keV}^{-1}$ and $j_2 = 1.93 \times 10^4\,\text{cm}^{-2}\text{s}^{-1}\text{sr}^{-1}\text{keV}^{-1}$. The δ values can be estimated using formula (36), thus $\delta_1 = 0.3985$ and $\delta_2 = 0.1001$. Assuming that $E_{\text{eff}_1} = 46.05\,\text{keV}$ and $E_{\text{eff}_2} = 83.75\,\text{keV}$, i. e. the mean energies of the energy channels, we can calculate new γ using expression (39). Then the new calculated spectral index is $\gamma = 2.28$. With this using the last expression in formula (38) we can find new effective energies $E_{\text{eff}_1} = 42.05\,\text{keV}$; $E_{\text{eff}_2} = 83.29\,\text{keV}$ and the new spectral index $\gamma = 2$; then again $E_{\text{eff}_1} = 42.39\,\text{keV}$; $E_{\text{eff}_2} = 83.33\,\text{keV}$ and $\gamma = 2.02$. Iterate until E_{eff_1} and E_{eff_2} will be approximately constant, usually 2 to 3 iterations are sufficient.

It is also possible to estimate the effective energy in a simpler way assuming for example that the $\gamma = 4$ and then calculate the E_{eff} using the last expression in formula (38). The estimations of the effective energy at different γ shows that the values of the effective energy are differ from each other in the less than 10% range. And this is not higher than the standard deviation error for the energy channel thresholds calculations which is about 10%.

B.2 Conversion Factors for Mean Energies

Rather than employing the complicated method described above, one can simply use the geometric mean energy $E_g = \sqrt{E_1 \cdot E_2}$ with equations 31 and 34 to generate a set of fixed conversion factors between differential flux and phase space density, as listed in Table 5.

B.3 Effective Energy and Geometric Mean Energy

The geometric mean energy E_g defined above is in fact a good approximation to the effective energy $E_{\rm eff}$. Let us recast equations 35 and 37 in terms of E_g:

$$\begin{aligned}\frac{J}{E_2 - E_1} &= A \cdot E_{\rm eff}^{-\gamma} \\ &= \frac{A}{E_2 - E_1} \frac{E_g^{-\gamma+1}}{\gamma - 1} \left[(E_1/E_g)^{-\gamma+1} - (E_2/E_g)^{-\gamma+1} \right] \end{aligned} \tag{40}$$

Let us simply this by setting $r^2 = E_2/E_1 > 1$, from which $E_1 = E_g/r$ and $E_2 = r E_g$. Equation 40 then leads to:

$$\begin{aligned}\left(\frac{E_{\rm eff}}{E_g} \right)^{-\gamma} &= \frac{1}{\gamma - 1} \frac{r^{\gamma-1} - r^{-\gamma+1}}{r - r^{-1}} \\ &\to 1 \quad \text{as } r \to 1 \end{aligned} \tag{41}$$

Demonstration: for $E_2 = 2E_1$, and $\gamma = 4$, we have $r = \sqrt{2}$ and equation 41 yields $E_{\rm eff}/E_g = 0.962$; this shows that E_g is a good estimate of $E_{\rm eff}$ even for this "extreme" case.

B.4 Energy Density with Geometric Mean Energy

Energy density, ε, for a finite energy channel should be

$$\varepsilon = \int_{E_1}^{E_2} f E \, {\rm d}^3 v, \tag{42}$$

where f is the phase space density of particles with velocity v, E_1 and E_2 are the energy channel thresholds. The energy density expressed through the omnidirectional flux will be the following:

$$\varepsilon = \int_{E_1}^{E_2} \sqrt{\frac{m}{2}} \sqrt{E} j(E) \, {\rm d}E {\rm d}\Omega = 2\pi \sqrt{\frac{m}{2}} \int_{E_1}^{E_2} \sqrt{E} j(E) \, {\rm d}E, \tag{43}$$

where Ω is the field of view. Here, phase space density, f, was converted into differential flux using equation 30. Therefore, the simple formula to calculate the energy density for the narrow energy channel will be:

$$\varepsilon = \pi \sqrt{2m} \sqrt{E} j(E) \, \Delta E, \tag{44}$$

The problem, which can appear in case of wide energy channel, is the definition of the energy E, which is suppose to be an effective energy of the corresponding channel. As it was mention in Section B.2 for the defining the effective energy, E, the geometric mean energy, $E_g = \sqrt{E_1 \cdot E_2}$ is often used, rather than more precise definition from Section B.1. The question is how reliable this simplification and at which spectral slopes and energy channel width it is appropriate to use.

It is reasonable to assume that at RAPID energies the differential flux $j = A \cdot E^{-\gamma}$ has a power law dependence on energy. Therefore,

$$\begin{aligned}\varepsilon &= \pi \sqrt{2m} \int_{E_1}^{E_2} \sqrt{E} A \cdot E^{-\gamma} \, {\rm d}E \\ &= \pi \sqrt{2m} \frac{A}{\gamma - 3/2} \left[E_1^{-\gamma+3/2} - E_2^{-\gamma+3/2} \right] \end{aligned} \tag{45}$$

Let us test how well this exact power-law formula compares with the "geometric mean energy density" found by setting $E \to E_g$ and $j(E) \to J/(E_2 - E_1)$ in equation 44. Recall that the measured mean differential flux $J/(E_2 - E_1) = A \cdot E_{\rm eff}^{-\gamma}$ (equation 37), expressed in terms of the effective energy.

Again we use $r^2 = E_2/E_1 > 1$, and then $E_1 = E_g/r$ and $E_2 = rE_g$; and for further simplification, we set $\alpha = \gamma - 3/2$.

$$\begin{aligned}
\varepsilon &= \pi\sqrt{2m}\,\frac{A\,E_g^{-\gamma+3/2}}{\gamma-3/2}\left[(E_1/E_g)^{-\gamma+3/2} - (E_2/E_g)^{-\gamma+3/2}\right] \\
&= \left\{\pi\sqrt{2m}\sqrt{E_g}\;(A\cdot E_{\rm eff}^{-\gamma})\Delta E\right\}\frac{1}{\gamma-3/2}\frac{E_g}{\Delta E}\left(\frac{E_g}{E_{\rm eff}}\right)^{-\gamma}\left(r^{\gamma-3/2} - r^{-\gamma+3/2}\right) \\
&= \left\{\pi\sqrt{2m}\sqrt{E_g}\;(J/\Delta E)\Delta E\right\}\frac{1}{\gamma-3/2}\left(\frac{E_g}{E_{\rm eff}}\right)^{-\gamma}\left(\frac{r^{\gamma-3/2} - r^{-\gamma+3/2}}{r - r^{-1}}\right) \\
&= \varepsilon_g\,\frac{1}{\gamma-3/2}\left(\frac{E_g}{E_{\rm eff}}\right)^{-\gamma}\left(\frac{r^{\gamma-3/2} - r^{-\gamma+3/2}}{r - r^{-1}}\right)
\end{aligned} \tag{46}$$

Here ε_g is the geometric mean energy density, equation 44 with E_g in place of E and $J/\Delta E$ for $j(E)$.

We now apply equation 41 and get for the deviation dev between the power-law energy density and the geometric mean energy density:

$$\begin{aligned}
\text{dev} &= \varepsilon/\varepsilon_g \\
&= \frac{\gamma-1}{\gamma-3/2}\,\frac{r^{\gamma-3/2} - r^{-\gamma+3/2}}{r^{\gamma-1} - r^{-\gamma+1}}
\end{aligned} \tag{47}$$

Using our previous example of $E_2 = 2E_1$ and $\gamma = 4$, equation 47 yields dev $= 0.949$.

Note that $r > 1$ and ideally $r \to 1$ for a narrow bin. In this case dev $\to 1$. However, in case of wide energy channels one has to use the formula 47 for calculation of the energy density deviation.

C Standard Deviations of Processed Data

Every measurement has an associated error bar defining the uncertainty in that measurement. For particle counters, the fundamental source of error is in the random nature of the incoming particles; but a second source of uncertainty lies in the on-board data compression.

C.1 Poisson Standard Deviations

Poisson statistics describe the situation when one is counting the number of discrete *random* events within a given time interval. It is important that the events be random, that is, completely independent of one another. In this case, the probability of acquiring n counts is given by

$$\Pr(n) = \mathrm{e}^{-\lambda}\frac{\lambda^n}{n!} \tag{48}$$

where λ is a parameter that needs to be determined. (This is equation 4 once more from Section 11).

It can be shown that λ is both the mean value and variance of this distribution. Thus when one has a single, the best estimate for the mean λ is simply the measured count n with an error of $\sqrt{n}$, the standard deviation (= square root of the variation). This is the well-known rule-of-thumb for particle counters.

However, this rule applies only to the *counts* themselves, and not to any function of them, such as count rates or particle fluxes. For such a function, say $F(n) = K\cdot n$, we have for its mean and variance:

$$\begin{aligned}
\langle F(n)\rangle &= K\cdot\langle n\rangle \\
\mathrm{Var}(F(n)) &= K^2\mathrm{Var}(n)
\end{aligned} \tag{49}$$

meaning that the error (standard deviation) in $F(n)$ is K times the error in n, and by no means the square root of $F(n)$! For this reason, we provide the derived standard deviations along with the data products since it is not possible for the user to work them out without knowing the detailed conversion factors.

For Poisson statistics, the relative error decreases with larger counts. For $n = 10$, the relative error is 31%, for $n = 100$, 10%, and so on. The relative errors in any derived functions will be the same as in the count.

C.2 Data Compression Errors

The method for compressing the on-board data is described in Appendix C of RAP-ICD. Compression is necessary so that even large numbers can be encoded and transmitted in a single byte, but it also means that the decoded numbers lose precision. The maximum precision possible is 5 bits, i.e. one out of 32, or about ±1.5%.

In the one example given in Appendix C, all numbers between 176 and 183 are encoded the same and then decoded as 179.5, thus the uncertainty in this value is ±3.5, or ±2%.

This uncertainty is based on the full range of possible numbers, whereas the variance is the mean squared deviation from the average value. For a set of m consecutive integers, that variance is

$$\mathrm{Var}\{n, n+1, \ldots, n+m-1\} = \frac{m^2-1}{12} \tag{50}$$

The standard deviations given in the RAPID datasets include those from both the Poisson statistics and the decompression uncertainty, by summing the two variances. For most realistic situations, the Poisson error dominates. It is not until we have a count of several thousands that the decompression standard deviation is greater. (E.g., for count = 10 000, Poisson standard deviation is 100, decompression is 150.) Such high *individual* counts (per energy channel, per direction, per spin) occur only for omnidirectional products in the radiation belts, where counts of ∼1000 can be encountered. In any event, the effect of both are included in the delivered standard deviations.

C.3 Combining Standard Deviations

The given standard deviations apply only to the associated measurement. If one wants to combine measures, say to take an average of flux values over 10 minutes, then one sums over all the individual single-spin measurements and divides by the total number (about 150 for 10 minutes).

So far so good, but what is the standard deviation of this function of the individual measurements. The rule here is:

> *The variance of a sum of independent variables is the sum of their variances.*

This, together with equation 49, means that for N values of some measurement F_n with standard deviations σ_n, the average $\bar{F}$ is

$$\bar{F} = \frac{1}{N}\sum_{n=1}^{N} F_n \tag{51}$$

$$\mathrm{Var}(\bar{F}) = \frac{1}{N^2}\sum_{n=1}^{N} \sigma_n^2 \tag{52}$$

$$\sigma(\bar{F}) = \sqrt{\mathrm{Var}(\bar{F})} = \frac{\bar{\sigma}}{\sqrt{N}} \tag{53}$$

That is, the precision in the average value improves as the square root of N.

C.4 Determining the Actual Standard Deviation

If one has something like 150 measurements, then it is reasonable to calculate the actual variance.

For N measurements of F_n, the best estimate of the variance for one measurement is

$$\sigma^2(F_n) = \frac{1}{N-1}\sum_{n=1}^{N}(F_n - \bar{F})^2 \tag{54}$$

(The factor $1/(N-1)$ arises instead of $1/N$ because one degree of freedom is lost in the determination of $\bar{F}$ itself.)

This is the estimated variance for each single measurement; it can be higher than the statistical variance in the individual values since the fluxes being measured do not need to be constant. There can also be physical noise in the source as well.

Now the estimated variance for the overall average is then

$$\sigma^2(\bar{F}) = \frac{1}{N}\sigma^2(F_n) \tag{55}$$

or, the error in the average is the error in the individual values divided by $\sqrt{N}$.

C.5 The Meaning of Standard Deviation

To understand the significance of the standard deviation, one can look at the behaviour of the normal distribution. For larger values of λ ($\gtrsim 10$) the Poisson distribution can be approximated by a normal distribution of mean λ and standard deviation $\sqrt{\lambda}$.

For a normal distribution, the probability of being within one standard deviation of the mean is 68%. In other words, if we measure n counts within time Δt, then the actual count rate is likely to be $(n \pm \sqrt{n})/\Delta t$, with 68% reliability. There is still almost one chance in three that it is outside this range! The probability of being within two standard deviations of the mean is 95%.

So one can use the standard deviation as the error bar on the measurements, but one must understand that this is only a statement of likelihood, and not absolute certainty.

C.6 Error in the Calibration Factors

The above only takes into account the statistical errors in the measurements. In addition, one has to consider the systematic errors in the calibration factors themselves. This is very tricky, but we would expect that an error of 10% would be a reasonable estimate for this uncertainty.

D Times of ENA Mode

Listing of ENA times for SC4
Time range: 2001-01-01 to 2002-06-01

Start	Stop	Hours	R_E	Lat	LT	R_E	Lat	LT
Season 2001								
2001-01-12 12:26:58	2001-01-12 14:19:02	1.9	17.77	24.7	15.9	18.41	21.3	15.8
2001-01-14 21:02:00	2001-01-15 04:56:03	7.9	17.55	25.7	15.8	19.54	12.1	15.3
2001-01-24 07:56:55	2001-01-24 09:23:57	1.5	16.89	28.6	15.2	17.52	25.7	15.1
2001-01-26 16:47:09	2001-01-27 01:06:21	8.3	16.75	29.2	15.1	19.33	14.1	14.6
2001-01-29 01:42:09	2001-01-29 04:00:00	2.3	16.63	29.6	14.9	17.63	24.9	14.8
2001-02-12 07:07:12	2001-02-13 13:40:20	30.6	15.94	32.2	14.1	14.88	-24.2	12.3
2001-02-28 22:07:01	2001-03-01 14:34:12	16.5	15.41	34.0	13.1	19.59	4.1	12.1
2001-03-03 07:07:02	2001-03-04 12:54:32	29.8	15.35	34.3	12.9	13.15	-32.3	10.7
2001-03-08 01:12:02	2001-03-09 08:45:05	31.6	15.25	34.6	12.6	14.93	-24.7	10.7
2001-03-15 04:32:10	2001-03-16 11:50:10	31.3	15.22	34.5	12.1	15.10	-24.2	10.3
2001-03-17 13:37:13	2001-03-18 20:50:01	31.2	15.21	34.5	12.0	15.17	-23.9	10.1
2001-03-22 07:46:58	2001-03-22 14:15:55	6.5	15.15	34.7	11.7	18.13	20.8	11.1
2001-03-27 02:07:14	2001-03-28 08:50:01	30.7	15.18	34.4	11.3	15.47	-23.0	9.5
2001-03-29 11:11:55	2001-03-29 14:19:12	3.1	15.16	34.4	11.2	19.15	13.4	10.4
2001-03-31 20:21:58	2001-04-02 02:45:04	30.4	15.21	34.2	11.0	15.62	-22.4	9.2
2001-04-05 14:36:52	2001-04-07 08:24:57	41.8	15.20	34.1	10.7	5.68	-65.8	1.7
2001-04-07 23:52:04	2001-04-08 05:20:40	5.5	15.28	33.7	10.5	19.03	14.2	9.8
2001-04-10 09:01:57	2001-04-12 03:31:14	42.5	15.30	33.6	10.3	4.68	-49.1	23.0
2001-04-15 03:22:03	2001-04-15 16:36:52	13.2	15.40	33.2	10.0	19.52	8.1	9.2
2001-04-19 21:52:16	2001-04-20 03:20:38	5.5	15.54	32.4	9.7	18.00	20.8	9.3
2001-04-22 07:11:57	2001-04-23 10:30:05	27.3	15.64	31.9	9.5	16.80	-17.7	8.0
2001-04-24 16:27:08	2001-04-26 09:09:39	40.7	15.73	31.5	9.3	5.70	-66.3	0.5
2001-04-29 10:57:13	2001-04-29 15:55:43	5.0	15.92	30.8	9.0	18.06	20.4	8.6
2001-05-01 20:22:13	2001-05-02 09:21:59	13.0	16.07	30.0	8.8	19.56	6.2	8.1
2001-05-23 11:27:00	2001-05-23 22:05:10	10.6	18.25	19.1	7.1	19.52	1.4	6.6
2001-05-25 21:56:56	2001-05-26 04:54:56	7.0	18.76	16.3	6.8	19.65	4.9	6.5

Start	Stop	Hours	R_E	Lat	LT	R_E	Lat	LT
Season 2001–2002								
2001-12-21 17:22:08	2001-12-21 20:59:33	3.6	19.43	-1.9	16.7 →	19.00	-8.0	16.5
2001-12-26 08:32:09	2001-12-26 17:20:04	8.8	19.44	3.1	16.5 →	18.53	-11.8	16.1
2001-12-31 01:04:03	2001-12-31 18:31:08	17.5	19.31	5.9	16.3 →	15.76	-26.3	15.4
2002-01-02 08:52:03	2002-01-02 09:40:44	0.8	19.14	8.1	16.2 →	19.25	6.7	16.1
2002-01-04 17:17:14	2002-01-05 07:55:05	14.6	19.03	9.2	16.1 →	17.88	-16.0	15.4
2002-01-19 01:22:46	2002-01-19 14:43:25	13.3	19.14	5.1	15.0 →	12.84	-41.0	13.5
2002-01-21 05:02:27	2002-01-21 20:01:04	15.0	18.08	14.9	15.1 →	18.53	-11.6	14.3
2002-01-25 22:31:57	2002-01-25 23:54:31	1.4	17.89	16.1	14.8 →	18.29	13.5	14.7
2002-02-02 00:57:05	2002-02-02 09:19:10	8.4	17.61	17.6	14.4 →	19.23	2.2	13.9
2002-02-09 03:36:56	2002-02-10 07:05:12	27.5	17.40	18.6	13.9 →	13.95	-36.1	12.2
2002-02-11 12:35:06	2002-02-11 23:50:49	11.3	17.36	18.8	13.8 →	19.25	-1.7	13.2
2002-02-13 21:34:58	2002-02-14 21:36:15	24.0	17.30	18.9	13.6 →	16.09	-26.3	12.3
2002-02-16 06:26:56	2002-02-16 18:02:18	11.6	17.20	19.3	13.5 →	19.25	-1.9	12.8
2002-02-18 15:21:51	2002-02-18 17:46:18	2.4	17.13	19.6	13.3 →	17.98	14.7	13.2
2002-02-21 00:21:56	2002-02-21 17:46:20	17.4	17.11	19.8	13.2 →	18.57	-11.8	12.2
2002-02-23 19:52:05	2002-02-23 23:48:11	3.9	19.24	0.3	12.4 →	19.07	-6.4	12.2
2002-03-07 06:21:58	2002-03-07 07:23:03	1.0	16.88	20.5	12.2 →	17.29	18.3	12.2
2002-03-09 15:21:58	2002-03-09 16:47:17	1.4	16.85	20.7	12.1 →	17.42	17.6	12.0
2002-03-21 21:09:07	2002-03-22 00:10:57	3.0	19.06	4.2	10.8 →	19.25	-1.0	10.7
2002-03-26 16:30:36	2002-03-26 19:24:31	2.9	19.17	2.0	10.4 →	19.25	-3.0	10.3
2002-04-02 18:55:58	2002-04-02 21:09:55	2.2	19.10	3.3	10.0 →	19.25	-0.5	9.9
2002-04-14 15:52:31	2002-04-14 18:51:30	3.0	19.05	3.8	9.2 →	19.26	-1.3	9.1
2002-04-21 20:00:39	2002-04-21 23:34:29	3.6	19.15	2.1	8.7 →	19.25	-4.0	8.6